

Electronic Theses and Dissertations, 2004-2019

2013

Study Of Transport Phenomena In Carbon-based Materials

Walid Aboelsoud
University of Central Florida

 Part of the [Mechanical Engineering Commons](#)
Find similar works at: <https://stars.library.ucf.edu/etd>
University of Central Florida Libraries <http://library.ucf.edu>

This Doctoral Dissertation (Open Access) is brought to you for free and open access by STARS. It has been accepted for inclusion in Electronic Theses and Dissertations, 2004-2019 by an authorized administrator of STARS. For more information, please contact STARS@ucf.edu.

STARS Citation

Aboelsoud, Walid, "Study Of Transport Phenomena In Carbon-based Materials" (2013). *Electronic Theses and Dissertations, 2004-2019*. 2707.
<https://stars.library.ucf.edu/etd/2707>

STUDY OF TRANSPORT PHENOMENA IN CARBON-BASED MATERIALS

by

WALID ABOELSOUD ABDELHAADY ABOELSOUD
M.Sc. Ain Shams University, 2005

A dissertation submitted in partial fulfillment of the requirements
for the degree of Doctor of Philosophy
in the Department of Mechanical and Aerospace Engineering
in the College of Engineering and Computer Science
at the University of Central Florida
Orlando, Florida

Spring Term
2013

Major Professor: Louis C. Chow

© 2013 Walid Aboelsoud Abdelhaady Aboelsoud

ABSTRACT

In air-cooled heat exchangers, air-side thermal resistance is usually the largest compared to conduction and liquid-side thermal resistances. Thus, reducing the air-side thermal resistance with fin-like structures can greatly improve overall cooling performance. The performance of these structures is usually characterized by the rate of heat which can be transferred and the pumping power required. One promising solution is to use a high-thermal-conductivity material with a large surface per unit volume such as carbon foam. This study presents a method of utilizing V-shape corrugated carbon foam. The air-side heat transfer coefficient and the pressure drop across the foam have been investigated using different V-shape foam geometrical configurations obtained by varying its length and height. Based on design considerations and availability, the foam length has been chosen to be 25.4, 38.1 and 52.1 mm while its height is 4.4, 6.8 and 11.7 mm, resulting in nine different test pieces of foam with different heights and lengths.

A total number of 81 experiments were carried out and results show that of the nine V-shape configurations, the foam with the shortest length and tallest height gives the best performance. Experimental results are also compared with the results of prior work using different carbon foam geometries. It is shown that V-shape corrugated carbon foam provides higher heat transfer coefficient and better overall performance.

Numerical method is performed next. The effect of the foam length and height on thermal and hydraulic performance is demonstrated and discussed. There is excellent agreement between numerical and experimental results. An analysis is also made to better understand the transport

phenomena that occur within the porous matrix. For laminar flow of air, one of the findings is the high heat transfer effectiveness of the foam which means a foam thickness of 1 mm or less is sufficient for heat transfer enhancement for air speed of up to 4 m/s.

To demonstrate the feasibility of using carbon foam, an analytical case study of carbon foam heat exchanger was performed and compared to traditional heat exchanger with the same heat load. Results show that a volume saving of up to 55% can be obtained by using carbon foam instead of traditional aluminum fins.

Another attractive carbon-based material is the highly oriented pyrolytic graphite (HOPG) which has an in-plane thermal conductivity of about 1700 W/m.K and an out-of-plane k of about 8 W/m.K at room temperature. HOPG is a graphite material with a high degree of preferred crystallographic orientation. HOPG can be very useful in thermal applications when axial conduction is critical and needed to be minimized as in recuperators used in cryocoolers and compact power generation. Also, an analysis of HOPG for micro-channel applications shows that the high in-plane thermal conductivity of HOPG, which is far greater than that of copper and aluminum, allows a taller height for the micro-channel. This translates to an increase in the heat flux removal rate by two to three times.

ACKNOWLEDGMENTS

This dissertation holds far more than the culmination of years of study. It also reflects the relationships with many generous and inspiring people I have met since the beginning of my graduate work. I would like to express the deepest appreciation to my advisor, professor **Louis C. Chow**, who continually and convincingly conveyed a spirit of adventure in regards to research, and an excitement in regards to teaching. Without his guidance and persistent help this dissertation would not have been completed. Thanks to Dr. **Wei. Wu** and Mr. **Y. R. Lin** who guided me in the past several years and helped me to perform the experiment. Special thanks to RINI Technologies Inc. for their financial and technical support. Thanks to my committee members, **professor Ranganathan Kumar**, professor **Weiwei Deng** and professor **Aravinda Kar** for their input, valuable discussions and accessibility. I would also like to thank my parents, two sisters, younger brother and my fiancée and her family. They were always supporting me and encouraging me with their best wishes.

TABLE OF CONTENTS

LIST OF FIGURES	ix
LIST OF TABLES	xi
NOMENCLAUTURE.....	xii
CHAPTER ONE: INTRODUCTION.....	1
CHAPTER TWO: CARBON FOAM EXPERIMENT.....	11
Experimental Set-up and Procedure.....	11
Results and Discussion	20
Conclusion	33
CHAPTER THREE: CARBON FOAM SIMULATION AND ANALYSIS.....	34
Numerical Method	34
Free Air Flow	36
Porous Matrix.....	37
Boundary Conditions	38
Problem Setup and Solution Procedure	40
Numerical Results and Discussion.....	41
Analytical Method	48

Analytical Results and Discussion.....	51
Conclusion	56
CHAPTER FOUR: CARBON FOAM APPLICATIONS.....	57
Case Study	58
Condenser Analysis and Design	61
Results and Conclusion.....	63
CHAPTER FIVE: HIGHLY ORIENTED PYROLYTIC GRAPHITE (HOPG).....	64
Introduction.....	64
HOPG Micro-Channel	67
APPENDIX A: UNCERTAINTY ANALYSIS.....	70
Design Stage Uncertainty	71
Error Propagation.....	72
APPENDIX B: CALIBRATION OF MEASUREMENT INSTRUMENTS	77
Differential Pressure Gage.....	78
Rotameters	79
Thermocouples.....	81
APPENDIX C: CONDENSER DESIGN	84

Case (1): Superheat, Condensation and Subcooling	86
Case (2): Superheat and Condensation	92
Case (3): Condensation and Subcooling	95
Case (4): Condensation	98
LIST OF REFERENCES	102

LIST OF FIGURES

Figure 1. Schematic of Test Apparatus.....	11
Figure 2. Air volume flow rate measurements a. Frontal view b. Top view	12
Figure 3. V-shape carbon foam geometries and test section	14
Figure 4. Temperature measurements.....	17
Figure 5. Effect of foam height on thermal performance	21
Figure 6. Effect of foam length on thermal performance	22
Figure 7. Effect of foam height on hydraulic performance	24
Figure 8. Effect of foam length on hydraulic performance	25
Figure 9. Foam configurations used for comparison with V-shape corrugated carbon foam.....	26
Figure 10. Comparison between V-shape corrugated foam and other foam geometries.....	28
Figure 11. Volumetric HTC vs fluid power per unit volume	30
Figure 12. NTU per unit fluid power at different average air velocities	32
Figure 13. Geometry under study	34
Figure 14. Computational domain	35
Figure 15. Boundary conditions.....	39

Figure 16. Effect of foam length on hydraulic performance	42
Figure 17. Effect of foam height on the hydraulic performance.....	43
Figure 18. Effect of foam length on thermal performance	46
Figure 19. Effect of foam height on thermal performance	47
Figure 20. HTC analytical and numerical results	53
Figure 21. Variation of effectiveness along one minichannel	55
Figure 22. Picture of the traditional air-cooled condenser.....	58
Figure 23. Attainable region of the fan curve	59
Figure 24. Fan and foam coupling	60
Figure 25. New condenser with carbon foam inserts.....	62
Figure 26. Crystal structure of HOPG	65
Figure 27. In-plane thermal conductivity k_{xy} , out-of-plane thermal conductivity k_z and anisotropy ratio as a function of temperature	66
Figure 28. Micro-channel model.....	67

LIST OF TABLES

Table 1. Measurements and Instrumentation	13
Table 2. Foam geometries	15
Table 3. Representation of test matrix and uncertainty analysis for (F6)	18
Table 4. Foam geometries	35
Table 5. Boundary conditions	38
Table 6. Numerical results	44
Table 7. Analytical and numerical results	52
Table 8. New condenser design parameters	63

NOMENCLAUTURE

A_b	Base area, foot-print (m^2)	k_s	Solid thermal conductivity (W/m.K)
A_c	Cross sectional area (m^2)	L	Foam length (m)
A_o	Total outside surface area of the condenser (m^2)	L^*	Micro-channel passage length
A_f	Refrigerant flow area (m^2)	L_f	Total length of the corrugated foam wall (m)
a_c	Cross sectional area of the minichannel (m^2)	L_1	Condensation length of the condenser (m)
a_s	Surface area of the minichannel (m^2)	L_2	Superheat length of the condenser (m)
c_f	Inertia coefficient	L_3	Subcooling length of the condenser (m)
c_p	Average specific heat of air at constant pressure (J/kg.K)	\dot{m}	Total mass flow rate of air through foam (kg/s)
d_h	Hydraulic diameter (m)	\dot{m}_a	Mass flow rate of air through the condenser (kg/s)
d_m	minichannel diameter (m)	\dot{m}_m	Mass flow rate of air through the minichannel (kg/s)
d_p	pore diameter (m)	\dot{m}_R	Mass flow rate of Refrigerant through the condenser (kg/s)
D	Minichannel length	\bar{Nu}	Average Nusselt number
H	Foam height (m)	NTU	Number of Transfer Units
H^*	Micro-channel height	n	Total number of minichannels
HTC	Overall heat transfer coefficient (W/m ² .K)	\hat{n}	Normal unit vector perpendicular to surface area
h_v	Volumetric heat transfer coefficient (W/m ³ .K)	p	Fluid Power = $\dot{V} \cdot \Delta p$ (W)
\bar{h}_i	Average interfacial heat transfer coefficient based on LMTD (W/m ² .K)	Pr	Prandtl number
\bar{h}_i^*	Average interfacial heat transfer coefficient based on $(T_{fs} - T_{bi})$ (W/m ² .K)	P_w	Wetted perimeter (m)
\bar{h}_G	Average heat transfer coefficient of the refrigerant gas (W/m ² .K)	p_{sat}	Saturation pressure
\bar{h}_L	Average heat transfer coefficient of the refrigerant liquid (W/m ² .K)	p	Pressure field
K	Foam permeability with air (m^2)	Q	Total rate of heat transferred (W)
k	Thermal conductivity	Q_{in}	input power (W)
k_{eff}	Effective thermal conductivity (W/m.K)	Q_{loss}	= $Q_{in} - Q$ (W)
k_f	Fluid thermal conductivity (W/m.K)	q_x	Rate of heat transferred to air up to distance x within one minichannel (W)

q	Total rate of heat transferred to air within one minichannel (W)	U_o	Overall heat transfer coefficient of the condenser ($W/m^2.K$)
R_{AV}	Surface area to volume ratio of the foam (m^2/m^3)	V	Gross volume of the protruding surface = (W.H.L) (m^3)
Re	Reynolds number	V^*	Net volume of foam = (H.L.f.t) (m^3)
T	Temperature field	\dot{V}	Air volume flow rate (l/s)
T_f	Fluid temperature	v	velocity field (m/s)
T_s	Solid temperature	v_f	Filtration velocity (Darcy velocity) (m/s)
T_b	Bulk air temperature ($^{\circ}C$)	W	Foam width (m)
T_b^*	Minichannel base temperature ($^{\circ}C$)	W^*	Condenser width (m)
T_{bi}	Bulk inlet air temperature ($^{\circ}C$)	x	Distance measured from the inlet to the minichannel (m)
T_{bo}	Bulk outlet air temperature ($^{\circ}C$)	β_F	Forchheimer Coefficient (kg/m^4)
T_{bx}	Bulk air temperature after distance x from the entrance to the minichannel ($^{\circ}C$)	Δp	pressure drop (Pa)
T_{fb}	Foam base temperature ($^{\circ}C$)	Δh_{fg}	Latent heat of the refrigerant (kJ/kg)
T_{fs}	Minichannel surface temperature ($^{\circ}C$)	Δh	Enthalpy change (kJ/kg)
T_{sat}	Condensation temperature ($^{\circ}C$)	ϵ	Foam porosity
$T_{\bar{m}}$	Mean bulk temperature ($^{\circ}C$)	ϵ_m	Minichannel effectiveness
t	Foam wall thickness (2.5 mm)	ϵ_f	Foam effectiveness
t^*	Micro-channel wall thickness	η_f	Fin efficiency
U	Average inlet air velocity (m/s)	μ	Dynamic viscosity of air at $T_{\bar{m}}$ (N.s/m ²)
U_c	Instrument uncertainty	μ_s	Dynamic viscosity of air at T_{fs} (N.s/m ²)
U_d	Design-stage uncertainty	ρ	Average air density (kg/m^3)
U_z	Zero-order uncertainty	θ_b	($T_b^* - T_b$)
$U_{\Delta p}$	Uncertainty in differential pressure measurement	<u>Subscripts</u>	
$U_{\dot{V}}$	Uncertainty in volume flow rate measurement	G	Superheated gas
U_U	Uncertainty in velocity calculation	g	Saturated gas
U_h	Uncertainty in heat transfer coefficient calculation	L	Subcooled liquid
		l	Saturated liquid

CHAPTER ONE: INTRODUCTION

Air as a cooling medium is preferred in electronics cooling because it is convenient and readily available. However, since air has a low thermal conductivity and therefore a low heat transfer coefficient (HTC), it can be very challenging for researchers and designers to reduce air-side thermal resistance of heat exchangers and improve their thermal performance in many practical applications. Reducing the air-side thermal resistance can be achieved by increasing the heat transfer effectiveness with a fin structure made of a highly conductive material protruding from the air-side surface. Recently, carbon foam has gained great interest due to its excellent thermal characteristics.

Carbon foam is one of the materials recently developed by Oak Ridge National Lab. (ORNL) for heat transfer enhancement. The foam has excellent thermal properties (bulk thermal conductivities of up to 180 W/m.K). This is the first repeatable foam with bulk thermal conductivities of greater than 50 W/m.K, and the process was licensed to Poco Graphite under the trade name *PocoFoam*TM [1].

The pore size of *PocoFoam*TM ranges from 0.275 to 0.35 mm and its bulk density is between 200-600 kg/m³ [2]. Carbon foam has several distinct advantages over the more traditional metallic foams such as those made from aluminum. For example, the effective thermal conductivity of typical carbon foam is in the range 40–180 W/m.K [1], whereas the effective thermal conductivity of typical aluminum foam is between 2 and 26 W/m.K [3]. The high effective conductivity of carbon foam, coupled with an open, interconnected void structure with

porosity (75-90%) that yields a large internal surface area per unit volume ($5000\text{--}50,000\text{ m}^2/\text{m}^3$), makes carbon foam an attractive material for air cooling [3].

The effect of metal foams in heat exchangers has been studied in significant details. Mancin et al. [4] studied thermal and hydraulic performance of five copper foam specimens with different pore size and porosities. A comparison study based on global and interstitial heat transfer coefficient was conducted to identify the best foam specimen among the tested group. Chein et al. [5] studied copper foam heat sinks coated with silver using electroforming with different porosity, pore density, permeability, and inertial coefficient and compared their thermal and hydraulic performance with plate-fin and pin-fin heat sinks. As a result, copper foam shows better performance as compared to standard plate-fin and pin-fin heat sinks.

Aluminum is preferred in electronics cooling because it is light and has relatively high thermal conductivity. Similar to copper foam, Kim et al. [6] studied heat transfer characteristics of aluminum foam heat sink and compared their results with a conventional parallel-plate heat sink with the same size. Results showed that the heat transfer enhancement of aluminum foam heat sink is 28% or higher than the conventional heat sink. Another comparison between a porous fin made of 6101 aluminum-alloy and a conventional louvered fin was done by Kim et al. [7]. Their results showed that the two types of fins have similar thermal performance with the louvered fin showing a little better performance.

Sertkaya et al. [8] compared thermal and hydraulic performance of aluminum foam (three different pore sizes) with aluminum fin (three different spacing) using a cross flow heat exchanger. They concluded that aluminum fin has better heat transfer characteristics as well as

lower pressure drop. They claimed that the heat transfer performance is better for the fin than the foam due to the poor thermal contact between the foam and its substrate.

The air-side heat transfer performance and the pressure drop was investigated by Garrity et al. [9] for three carbon foam samples. The performance of the three foam samples was compared with conventional multi-louvered fins. They assumed that the air-side thermal resistance is the dominant thermal resistance. Performance of samples were evaluated based on the coefficient of performance (COP, defined as the ratio of the total heat rate removed to the electrical input of the air blower), compactness factor (CF, defined as the total heat rate removed per unit volume), and power density (PD, defined as the total heat rate removed per unit mass). Their results showed that carbon foam samples provide a significant improvement in CF but the COP and PD are considerably lower than those for conventional multi-louvered fin heat exchangers.

Convective heat transfer coefficient in a channel with different geometries of carbon foam was experimentally and numerically studied by Leong et al. [10]. Foam geometries tested are block solid foam (BLK), zigzag foam (ZZG), and baffle foam (BAF). Their results showed that the solid block foam has the best heat transfer performance at the expense of high pressure drop. However, they claimed that their proposed configurations could achieve relatively good enhancement of heat transfer at moderate pressure drop.

Williams and Roux [11] investigated various air cooled base plate channel designs for an array of generic power amplifier modules. In their study, graphite foam and a micro-fibrous material were used as mini-heat exchangers to cool the power amplifier modules. Different foam geometries were tested such as zigzag, U-shape corrugation, and inline PocoFoam. All

geometries showed an improvement over the empty channel cooling. They concluded that the zigzag PocoFoam provides the most improvement in heat transfer coefficient among all other configurations.

Wu et al. [12] compared thermal and hydraulic performance of a V-shape corrugated carbon foam, of dimensions of 51x51x19 mm, with the U-shape corrugated carbon foam, pin finned, and solid carbon foam geometries reported in [1]. PocoFoam with porosity of 75% was used. They demonstrated that the V-shape geometry is an attractive heat sink for electronics and aerospace applications. Lin et al. [13] studied the U-shape corrugated carbon foam with wall thickness of 2.5 and 3 mm, they found that about 95% of the heat can be transferred to the fluid (air) within 4 mm of the foam thickness when the average air speed is 4 m/s.

Assessment of the heat sink performance based on thermal characteristics alone is not desirable because pumping power is also crucial in the selection of heat sink. It is important to keep the ratio of the heat transfer rate from the heat sink to the pumping power near a maximum while taking into account other design and selection considerations.

Vanka and Stone [14] discussed different methods to evaluate the improvement in the performance of several configurations of plate-fin heat exchangers. They provided a comprehensive review of how to judge and compare the effectiveness of these geometries. One of these methods was established by Soland et al. [15]. They chose the volumetric heat transfer coefficient (h_v) as a performance parameter to assess the heat transfer process. Pumping power per unit volume (P/V) was chosen as a pumping power performance parameter.

Due to its high thermal conductivity [1] and high surface area to volume ratio [3], carbon foam is an attractive material for air-side thermal resistance reduction consideration. V-shape corrugated carbon foam appears to be a very attractive solution for thermal management [12]. Therefore, there is a need for more studies to investigate the effect of geometrical parameters on thermal and hydraulic performance and to exploit this geometry in thermal applications.

In this study, thermal and hydraulic performance assessment of nine V-shape corrugated carbon foam pieces is introduced. Comparison of performance of the nine V-shape corrugated carbon foam geometries and the six foam geometries described in [9, 10] will be established. We will show that the V-shape corrugated carbon foam is a promising geometry which can achieve high heat transfer coefficient with minimal pressure drop.

Many numerical studies were carried out in order to gain better understanding of the transport phenomena in porous media. Vafai and Kim [16] mentioned that numerical results based on Brinkman-Forchheimer extended Darcy equation have been shown to agree well with experimental results. The equation accounts for boundary layer growth and macroscopic shear stress, as well as microscopic shear stress and microscopic inertial force. It is also very effective for studying the motion of the fluid in the region, which is partially filled with porous medium and partially filled with a regular fluid. This implies that this equation well describes the relation between parameters of momentum transport through porous media when a free fluid flow is in the neighborhood.

There are two energy transport models proposed in the literature. The first model is the local thermal equilibrium (LTE) model where the fluid temperature (T_f) and the solid temperature (T_s)

are assumed to be equal and there is only one energy equation. The second model is the local thermal nonequilibrium (LTNE) model where two distinct temperature fields within the porous matrix exist. The fluid temperature and the solid temperature are solved by using two distinct energy equations. The validity of LTE model was discussed in [17-20].

The assumption of LTE may not be valid for high speed flows or high permeability porous media in which the fluid to solid interaction time or surface area, respectively may not be large enough to bring the temperature of the fluid and solid phases close enough for LTE to be a reasonable assumption [17]. Experimental validation of numerical models requires measurement of the porous matrix temperature. Thermocouple is used to measure only one temperature which is a temperature between the fluid and solid temperatures. From that prospective, it is more appropriate to use the LTE model to describe the temperatures field rather than solve for the solid and fluid temperatures separately and then average them [18].

Kaviany [19] and Mohamad and Karim [20] mentioned that if there is a significant heat generation occurring in the solid or fluid phase and when the temperature at the interfacial surface changes significantly with respect to time, then the solid and fluid phases could be far from the local thermal equilibrium (LTE).

Fluid flow and heat transfer interfacial boundary conditions between the free fluid and the porous matrix were studied by Alazmi and Vafai [21]. The configuration used in their study is fluid flow between a porous medium and solid boundary kept at constant temperature. LTE condition is assumed. Five fluid flow boundary conditions and four heat transfer boundary conditions, from literature, are summarized and discussed. The effects of Reynolds number and porosity on

different types of interface conditions are analyzed. They concluded that results of velocity field, temperature field and Nusselt number are quite close for all of the fluid flow and heat transfer models however, small discrepancies could appear for cases where Reynolds number is small.

Numerical study of pressure driven laminar flow of air of uniform inlet velocity and uniform inlet temperature inside a pipe or channel was established by Mohamad [22]. The conduit is subjected to constant wall temperature and fully or partially filled with porous medium. The effects of porous layer thickness on the rate of heat transfer enhancement and pressure drop are investigated. In his study of energy transport, LTE is assumed based on a previous study of the author [20] which revealed that the thermal equilibrium assumption is valid as long as there is no heat generation in the fluid phase or in the solid phase. Moreover, a few tests done using LTNE assumption and results are not that sensitive to the nonequilibrium condition. Results showed that the inertia term of the momentum equation, has a significant effect on Nusselt number, but it is not clear that the correlation of the inertia term is valid for a highly porous. Results also showed that the heat transfer rate increases by increasing the thickness of the porous material inside the conduit on the expenses of having higher pressure drop. The optimum thickness of the porous material or radius ratio is found to be 0.6, where the heat transfer can be enhanced with a reasonable pressure drop. LTE will be assumed in the numerical part of this study.

Pavel and Mohamad [23] experimentally and numerically investigated the effect of aluminum porous media inserted in a pipe on the rate of heat transfer and the pressure drop where LTE model is assumed. The porous media consists of commercial aluminum screens of wire diameter 0.8 mm, density 2770 kg/m^3 and thermal conductivity $177 \text{ W/m}^2\text{K}$, with different outer

diameters and then inserted on steel rods. Twelve different configurations are obtained by varying the screen diameter and the distance between two adjacent screens. Pressure driven air flow is allowed into a pipe partially or fully filled with this porous media. The pipe is subjected to constant uniform heat flux. They studied the effect of porosity, diameter of the porous diameter, thermal conductivity and Reynolds number (1000 – 4500), on Nusselt number and the pressure drop. The conclusion is that the heat transfer enhancement can be achieved with larger diameter screens whose diameters approach the diameter of the pipe. For a constant diameter of the porous medium, further improvement can be achieved using a porous insert with a smaller porosity and higher thermal conductivity.

Alazmi and Vafai [24] investigated the effect of variances from literature on constant porosity, variable porosity, thermal dispersion, and local thermal nonequilibrium (LTNE) models on the transport process in porous media contained within parallel plate channel. The channel is subjected to constant heat flux or constant wall temperature boundary conditions. They showed that the effect of these variances on the presented models is significant on the velocity field and negligible on the temperature field and Nusselt number.

Alazmi and Vafai [25] studied the effect of variable porosity, thermal dispersion and LTNE on the characteristics of transport process for free surface flow through porous media. Parameters such as Reynolds number and the pore diameter are also used to quantify the significance of these effects. Results show that variable porosity has a significant effect only in the neighborhood of the solid boundary where no slip condition occurs.

Betchen and Straatman [26] studied the fluid flow and the heat transfer in a block of carbon foam with variable porosity in the transverse direction to the primary direction of water flow. The foam base is maintained at constant temperature. LTNE energy equations are used in their analysis. Results showed that only foam pieces with large porosity variation significantly affects the heat transfer for flow at relatively high Reynolds number. They found that superior thermal performance can be achieved by locating the more porous side of the foam adjacent to the heated surface, resulting in a significant increase in the rate of heat transfer.

Analysis of transport phenomena in porous media is introduced in literature. The analytical solution is compared to numerical result and closed form solution if any. Analytical investigation of forced convection flow through a channel subjected to constant uniform heat flux and filled with a porous media was performed by Marafie and Vafai [27]. Analytical solutions are obtained for both fluid and solid temperature fields including the effect of various parameters such as thermal conductivity ratio of fluid to solid, and inertia coefficient (c_f). The analytical solution is compared to the exact solution of LTE model available in the literature as well as the analytical solution for the LTNE model based on Darcian flow field (no inertia term). It is demonstrated that the inertia coefficient (C_f) have a small role in determining the validity of LTE model.

Haji-Sheikh and Vafai [28] analyzed the problem of fluid flow and heat transfer through channels of different geometries, subjected to constant uniform wall temperature, filled with porous material. The geometries used in their analysis are parallel plate channels, circular tubes and elliptical passages with different aspect ratios. Modified Graetz problem based on

Brinkman's model is introduced. Results are compared to results from another numerical study based on the method of weighted residuals.

Solid carbon foam has excellent thermal characteristics at the expense of poor hydraulic performance, namely high pressure drop. Recently, there have been great interests of how to take advantage of thermal benefits of carbon foam while overcome its drawbacks. One of the ideas is to change the foam geometry in such way it will keep the same thermal performance and reduce the pressure drop. Experimental and numerical investigation of fluid flow and heat transfer in a channel filled with different configurations of graphite foams were carried out by Leong et al. [10]. Foam geometries tested are block solid foam (BLK), zigzag foam (ZZG), and baffle foam (BAF). LTNE was assumed and the numerical code is validated by results obtained from [21].

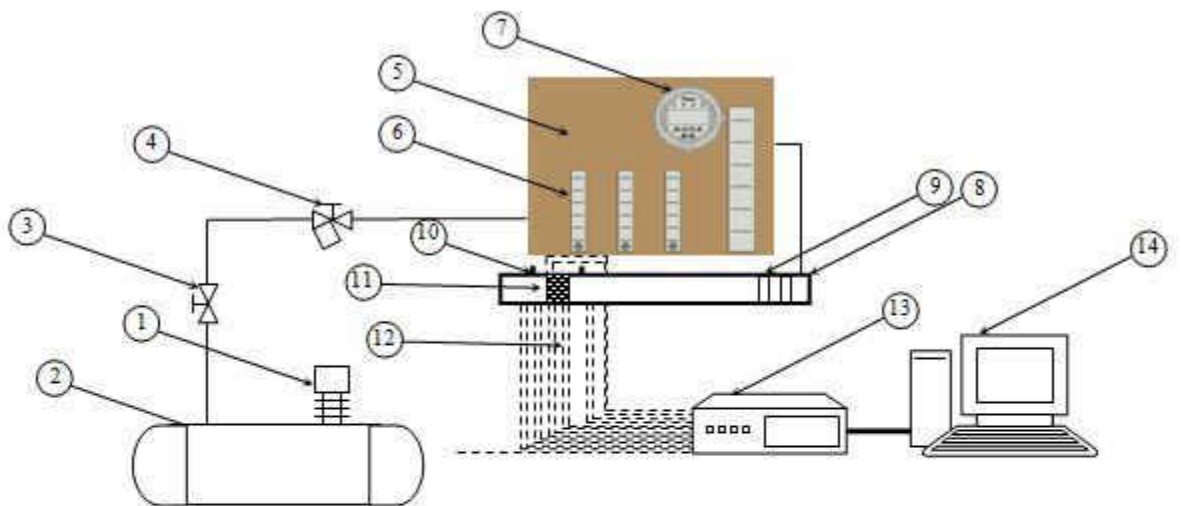
DeGroot and Straatman [29] proposed a numerical LTNE model for computing fluid flow and heat transfer with general unstructured, nonorthogonal grids. The major contribution of their model is its ability to use nonorthogonal grids to discretize complex geometries without affecting the robustness of the model and having any significant increase on the computational time. They demonstrated the efficiency of their model on a V-shaped corrugated carbon foam which is presented by [12].

Due to its high effective thermal conductivity, solid carbon foam has the potential to achieve excellent heat transfer performance however, the high pressure drop performance is a restriction on the way of achieving an ideal heat sink. The V-shape corrugated carbon foam can achieve even better thermal performance with less pressure drop [1].

CHAPTER TWO: CARBON FOAM EXPERIMENT

Experimental Set-up and Procedure

The experimental setup is shown in Figure 1. Air flows from the reservoir of a reciprocating compressor through an air hose to a set of four rotameters, OMEGA FL series 2035, 2060, 2061 and 2071, which are connected in parallel to air flow channel. As shown in Table 1, the rotameters have different full scale values. The maximum accuracy of the air flow measurement can be achieved by choosing the appropriate rotameter for each run. A single rotameter can be isolated using manual control valves attached in series to each rotameter as shown in Figure 2.



- | | |
|-------------------------------|-----------------------------|
| 1. Reciprocating compressor | 8. Air Channel |
| 2. Air Reservoir | 9. Mesh screens |
| 3. Hand valve | 10. Pressure taps |
| 4. Valve with water separator | 11. Test section |
| 5. Measurement board | 12. Thermocouples |
| 6. Rotameters | 13. Data Acquisition system |
| 7. Differential pressure gage | 14. Personal computer |

Figure 1. Schematic of Test Apparatus

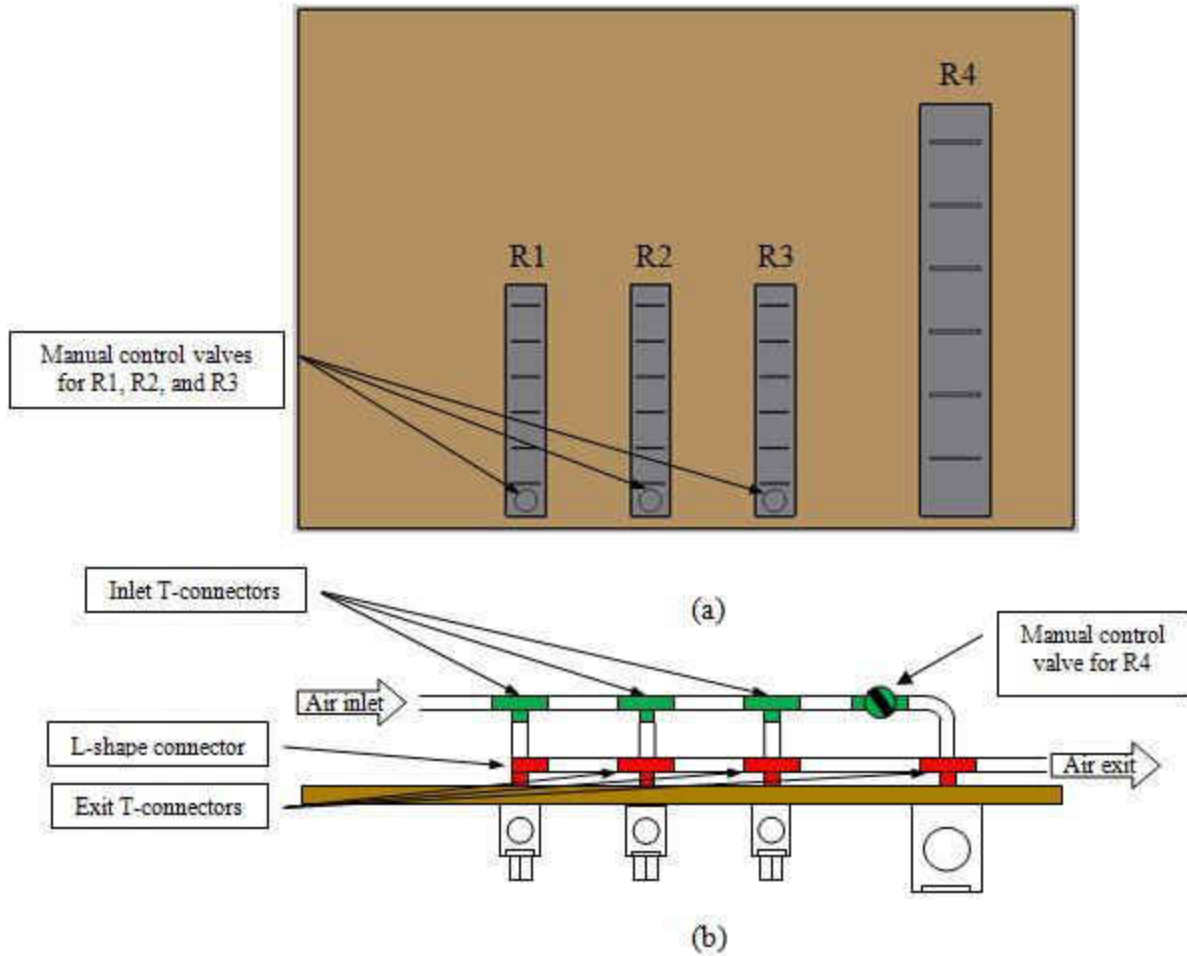


Figure 2. Air volume flow rate measurements a. Frontal view b. Top view

Air enters the air channel from an air hose attached to the side of the channel. It then passes through two mesh screens (100x100 openings per linear inch, 38.1 mm apart) to ensure a good distribution of air in all directions. Three sets of the screens with three different heights were used based on channel and foam heights (4.4, 6.8 and 11.7 mm). A DWYER 167-6 pitot tube, described in [Table 1](#), was used to verify a good air distribution. Air then flows through a channel 50 mm wide and 38 cm long with three different heights as mentioned before. The 38-cm entry

length prior to the test section is provided to ensure a fully developed flow before the test section. Finally, the air exits from the test section to the atmosphere ($p_{\text{atm.}}$). The maximum uncertainty in the volume flow rate measurements is $\pm 10.3\%$ and the average uncertainty is $\pm 5.1\%$ ([Appendix A](#)).

Table 1. Measurements and Instrumentation

Experiment parameter	Instrument	Model #	Flow range (SCFM)	Accuracy
Flow	Rotameter (R1)	OMEGA FL-2035	0.15-1.5	$\pm 3\%$ of F.S
	Rotameter (R2)	OMEGA FL-2060	0.5-5	$\pm 3\%$ of F.S
	Rotameter (R3)	OMEGA FL-2061	1-10	$\pm 3\%$ of F.S
	Rotameter (R4)	OMEGA FL-2071	3-25	$\pm 2\%$ of F.S
		Model #	Size (mm)	Insertion Length (mm)
Velocity	Pitot tube	Dwyer 167-6	3.2	152
		Model #	Rated capacity (W)	Length (mm)
Power	Cartridge heater	CSH102100/120	100	51
		Model #	Range (Pa)	Accuracy
Differential pressure	Gage (digital display)	Dwyer DM-1108	2491	$\pm 1\%$ of F.S

Nine different foam geometries with different lengths and heights were tested for their heat transfer and pressure drop characteristics. Foam lengths were chosen to be 25.4, 38.1 and 52.1 mm and heights to be 4.4, 6.8 and 11.7 mm. These nine foam geometries are listed in [Table 2](#). Foam wall thickness of 2.5 mm was chosen based on previous work done by Wu et al. [\[12\]](#) and Lin et al. [\[13\]](#). The test section consists of the V-shape corrugated carbon foam attached on the surface of copper block with the same foot print. The different foam geometries and test sections are shown in [Figure 3](#).

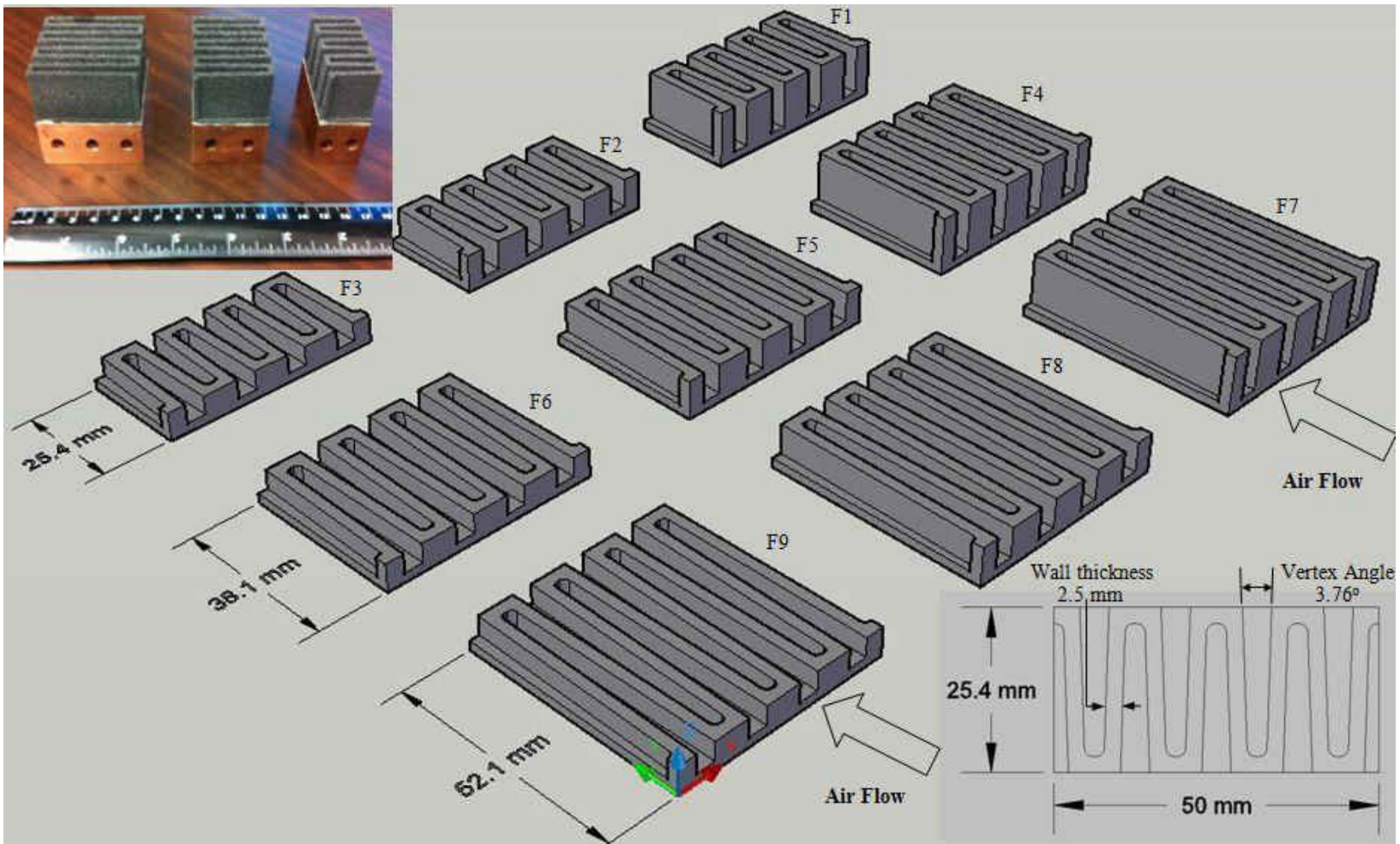


Figure 3. V-shape carbon foam geometries and test section

Two cartridge heaters, OMEGA CSH-102100/120 of 100 watt capacity each, shown in [Table 1](#), are inserted perpendicular to the flow direction in the middle plane of the copper block for the foam pieces of length 25.4 and 38.1 mm, while three cartridge heaters are inserted in the case of 52.1 mm long foam pieces. Silver-based adhesive material, Pyro-Duct 597A, was used to reduce the contact resistance between the foam and the copper surface as well as maintaining a good bond between foam and copper.

Table 2. Foam geometries

Configuration	Width (mm)	Height x Length (mm)	V-shape vertex angle (degrees)	# of free channels	Wall thickness (mm)
F1	50	11.7x25.4	3.76	4	2.5
F2	50	6.8x25.4	3.76	4	2.5
F3	50	4.4x25.4	3.76	4	2.5
F4	50	11.7x38.1	2.26	4	2.5
F5	50	6.8x38.1	2.26	4	2.5
F6	50	4.4x38.1	2.26	4	2.5
F7	50	11.7x52.1	1.66	4	2.5
F8	50	6.8x52.1	1.66	4	2.5
F9	50	4.4x52.1	1.66	4	2.5

Thirteen T-type thermocouples with an average bead diameter of 0.4 mm and average length of 40 cm were used for temperature measurement. The standard method of thermocouple calibration was performed ([Appendix B](#)). The maximum uncertainty in the temperature measurements is $\pm 0.1^\circ\text{C}$ ([Appendix A](#)). Two thermocouples located at 51 mm before the inlet to the test section were used to measure the temperature of the air upstream while four thermocouples located 2 mm after the test section ([Figure 4](#)) were used to measure the temperature of the air downstream. The maximum difference in the measured air temperature at outlet is 1.2°C . Four thermocouples were planted 1.5 mm below the copper surface to measure the average surface temperature of the copper as shown in [Figure 4](#). The maximum difference in

the measured temperature of the copper surface is 0.2°C . Two thermocouples were inserted 0.5 mm above the thermal adhesive layer to measure the foam base temperature (T_{fb}). The maximum difference in temperature measurement between them is 1.4°C .

The average inlet air temperature (T_{bi}) is the room temperature which ranges from 20.8 to 22.8°C . The Inlet pressure to the test section is the sum of the atmospheric air plus the pressure drop across the foam (Δp). The average temperature of the inlet air, outlet air and foam base for a representation of test matrix (F6, 4.4×38.1 mm) is shown in [Table 3](#).

Two pressure taps 10.2 cm apart were installed at 25.4 mm before the inlet to test section. A DWYER DM-1108 differential pressure gage, described in [Table 1](#), was used to measure the pressure difference between upstream and downstream. The calibration of the differential pressure gage is shown in [Appendix B](#). The maximum uncertainty in differential pressure measurements is $\pm 17.2\%$ and the average uncertainty is $\pm 10.7\%$ ([Appendix A](#)).

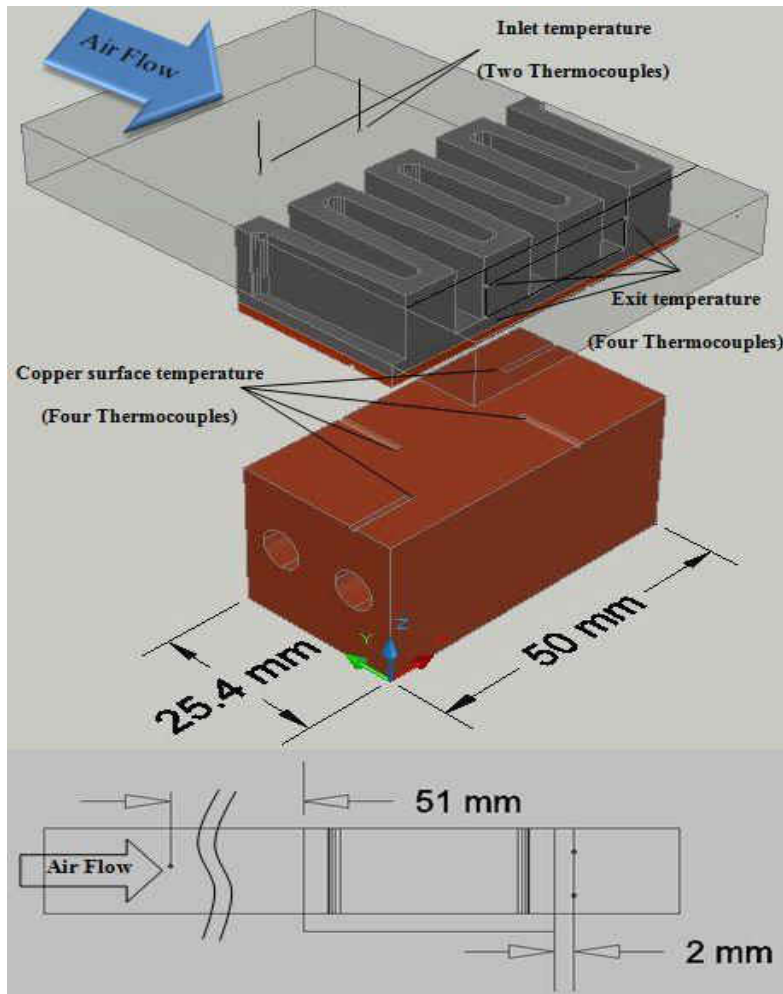


Figure 4. Temperature measurements

A Keithley multimeter/data acquisition system (integra series, model 2700) was used to acquire data from thermocouples from all measurements points. Cold junction compensation was done by simulating the cold junction electronically which was stored in the DAQ for T-type thermocouple. The Model 2700 uses the ITS-90 inverse function coefficients for the polynomial to calculate thermocouple temperature. The heaters were powered by a variable AC power supply which enables the control of the voltage input to the heaters and consequently the power input.

Table 3. Representation of test matrix and uncertainty analysis for (F6)

Foam #	Δp	\dot{V}	T_{fb}	T_{bi}	T_{bo}	HTC	$U_{\Delta p}$	$U_{\dot{V}}$	U_h	Q_{in}	Q_{loss}
	(Pa)	(l/s)	(°C)	(°C)	(°C)	(W/m ² .K)	(±%)	(±%)	(±%)	(W)	(%)
F6 (4.4x38.1) mm	145	0.2	54.5	21.3	52.9	201	17.2	10.3	6.3	12.7	28
	270	0.5	44.3	21.3	43.7	290	9.2	4.9	6.4	12.7	0
	750	0.8	34.3	21.3	34.1	510	3.3	3.2	6.4	12.7	7
	1045	1.0	31.6	21.2	31.4	642	2.4	7.6	6.5	12.7	6
	1655	1.2	29.3	21.1	29.3	808	1.5	6.1	6.6	12.7	6
	2350	1.5	27.8	21.1	27.8	987	1.1	5.1	6.7	12.7	7
		1.7	26.8	21.0	26.7	1156		4.3	6.8	12.7	8
		2.0	25.9	20.9	25.7	1353		3.8	6.9	12.7	12

Experimental procedures, described as follows, were repeated for each run:

1. Ensure all rotameter valves are closed then open the main air supply valve.
2. Decide which rotameter will be used for measurements based on the highest measurement accuracy and open the valve slowly until the float reaches the desired flow position.
3. Turn on the heater power supply and adjust the input voltage to the heaters to the desired value of the input power.
4. Keeping rotameter level constant, take measurements of all temperatures and differential pressure every 10 minutes until steady state is reached. Steady state is reached when measurements are the same for three consecutive measurement times.
5. Save results of this run and prepare for the next experiment by varying the rotameter, the rotameter float level and/or the heater input voltage to the desired value and repeat procedure number 4 and 5.

Calibration of flow meters and differential pressure gage were conducted before starting the experiments ([Appendix B](#)). Rotameters were calibrated using McMillan mass flow sensor (model 50s, 0-50 l/min) and differential pressure gage was calibrated using a U-tube manometer.

The heat transfer coefficient is defined in [Equation 1](#) based on the difference between the average foam base temperature and the average inlet air temperature.

$$HTC = \frac{Q}{A_b \cdot (T_{fb} - T_{bi})} \quad 1$$

Uncertainty propagation analysis was conducted as described in [\[30\]](#). [Table 3](#) shows a sample of the test matrix with corresponding measurements, calculations, and uncertainty analysis. The maximum uncertainty in the heat transfer coefficient was found to be $\pm 7\%$ and the average uncertainty is $\pm 6.5\%$. All uncertainty calculations are based on the 95% confidence level.

Results and Discussion

A total number of 81 experiments were carried out with different air face velocities (0.7 – 9 m/s) and heat fluxes of (0.5 – 2 W/cm²). [Table 2](#) shows the nine V-shape corrugated carbon foam pieces which were tested using different heat fluxes applied to the bottom of the foam and different upstream air velocities. A sample test result for F6 and the uncertainty of the measurements are given in [Table 3](#). We aim to show thermal and hydraulic performance of the V-shape corrugated carbon foam. Thermal performance of the foam is assessed by the heat transfer coefficient. Hydraulic performance is assessed by the pressure drop (Δp).

The performance of turbomachines is usually provided as the relation of the pressure drop, input power and efficiency as function of the volume flow rate. Thus we found it more useful to plot the performance parameters of the foam (pressure drop and the heat transfer coefficient) as a function of the air volume flow rate rather than the average air velocity. This enables the reader to estimate what the performance of the foam would be when coupled with a given fan or blower.

The relation between the volume flow rate of the air and the heat transfer coefficient at different foam heights with the same foam length is shown in [Figure 5](#). For the same volume flow rate, the velocity is inversely proportional to the foam height (same as channel height). The heat transfer coefficient is higher for the shorter foam height because the air velocity is higher.

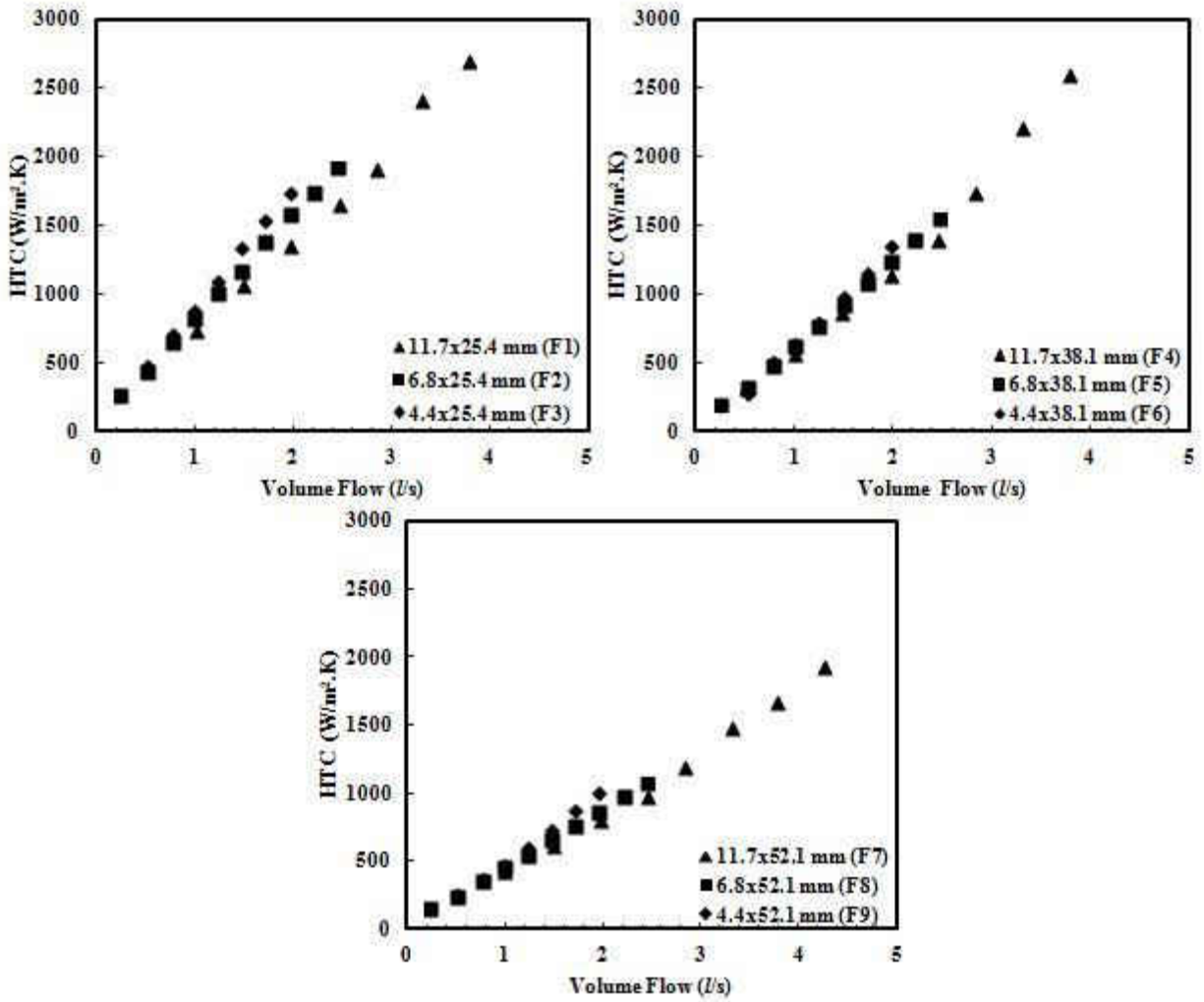


Figure 5. Effect of foam height on thermal performance

Figure 6 shows the relation between the volume flow rate of air and the heat transfer coefficient for different foam lengths with the same height. At a fixed inlet air velocity and heat load, the variation of the base temperature for all foam pieces is small. The base area of the foam is proportional to the foam length and the heat transfer coefficient is inversely proportional to the base area of the foam as illustrated in Equation 1. For the same heat load, temperature difference and air velocity, the shorter the foam length, the higher is the heat transfer coefficient.

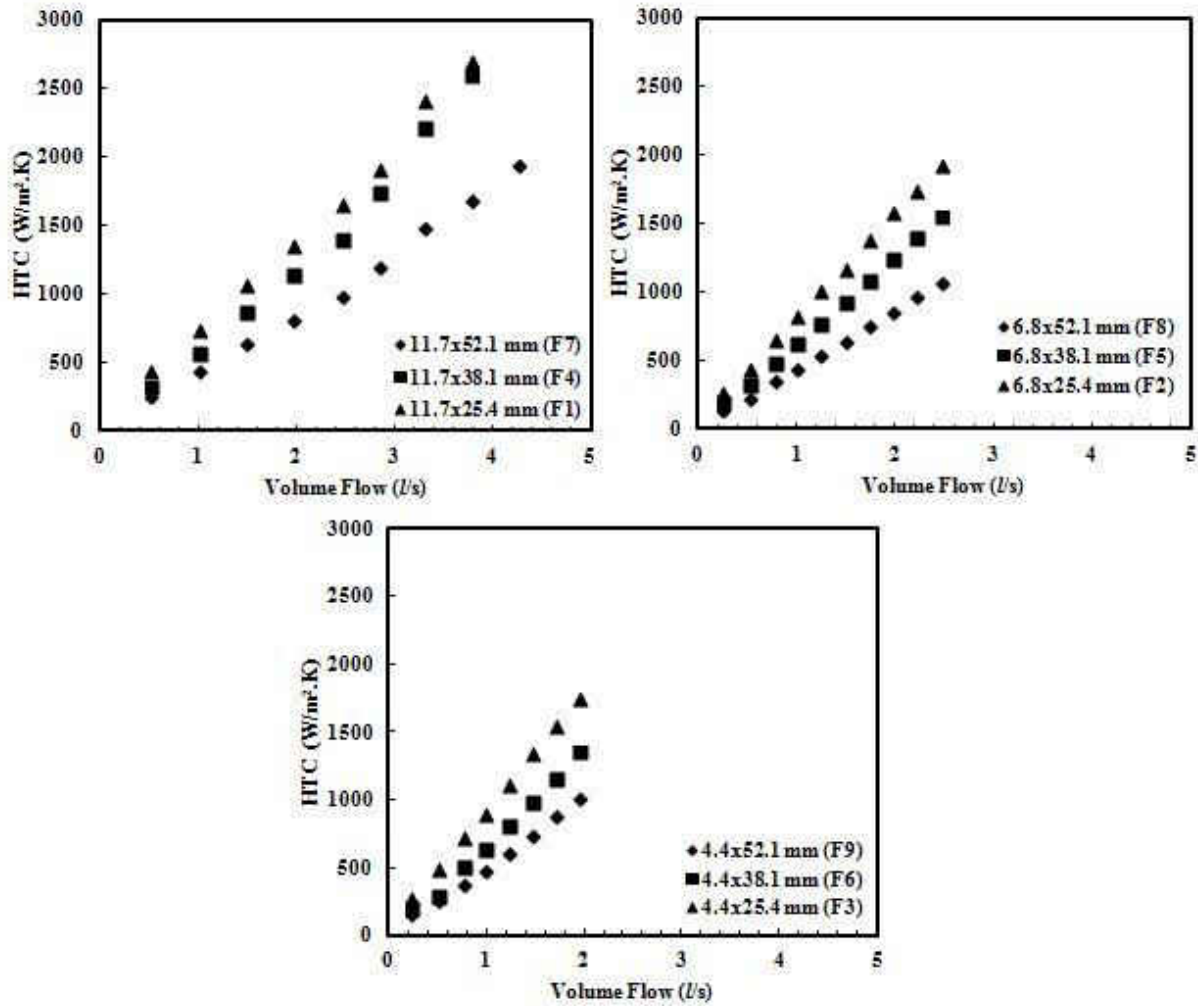


Figure 6. Effect of foam length on thermal performance

Hydraulic performance of the foam is of interest because it determines the pumping power required to convect the heat away from the surface. The pressure drop across the foam (Δp) can be characterized as:

1. Pressure drop through variable area channel with porous walls (Δp_1).
2. Pressure drop across the foam walls (Δp_2).

Air flowing across the V-shape corrugated carbon foam experiences the two pressure drops (Δp_1 & Δp_2). The total pressure drop (Δp) along a streamline is the sum of the two components since they can be considered as two flow resistances connected in series. Since the mass flow rate of air in one flow passage varies due to the mass transfer through the porous walls, air flow through the variable area channel could encounter different flow regimes: laminar, transition, and turbulent.

Figure 7 shows the relation between the volume flow rate of air and the pressure drop across the foam for different foam heights with the same foam length. For the same volume flow rate of air, the shorter the foam height the higher the pressure drop which is attributed to higher air flow velocity.

Figure 8 illustrates the relation between the volume flow rate of air and the pressure drop across the foam for different foam lengths with the same foam height. It is somewhat surprising that the total pressure drop across the foam decreases slightly with increasing the foam length. As air is forced to penetrate the foam wall of thickness of 2.5 mm, the local filtration velocity (v_f) crossing the foam wall decreases with increasing foam length since longer foam length means that the wall has larger overall surface area for the air to penetrate the foam. At a given air volume flow rate, as the foam length increases, the air filtration speed decreases. It appears that (Δp_2) drops more than the increase in (Δp_1) resulting in the total pressure drop characteristics shown in Figure 8. There is a competing action between the two pressure components Δp_1 and Δp_2 .

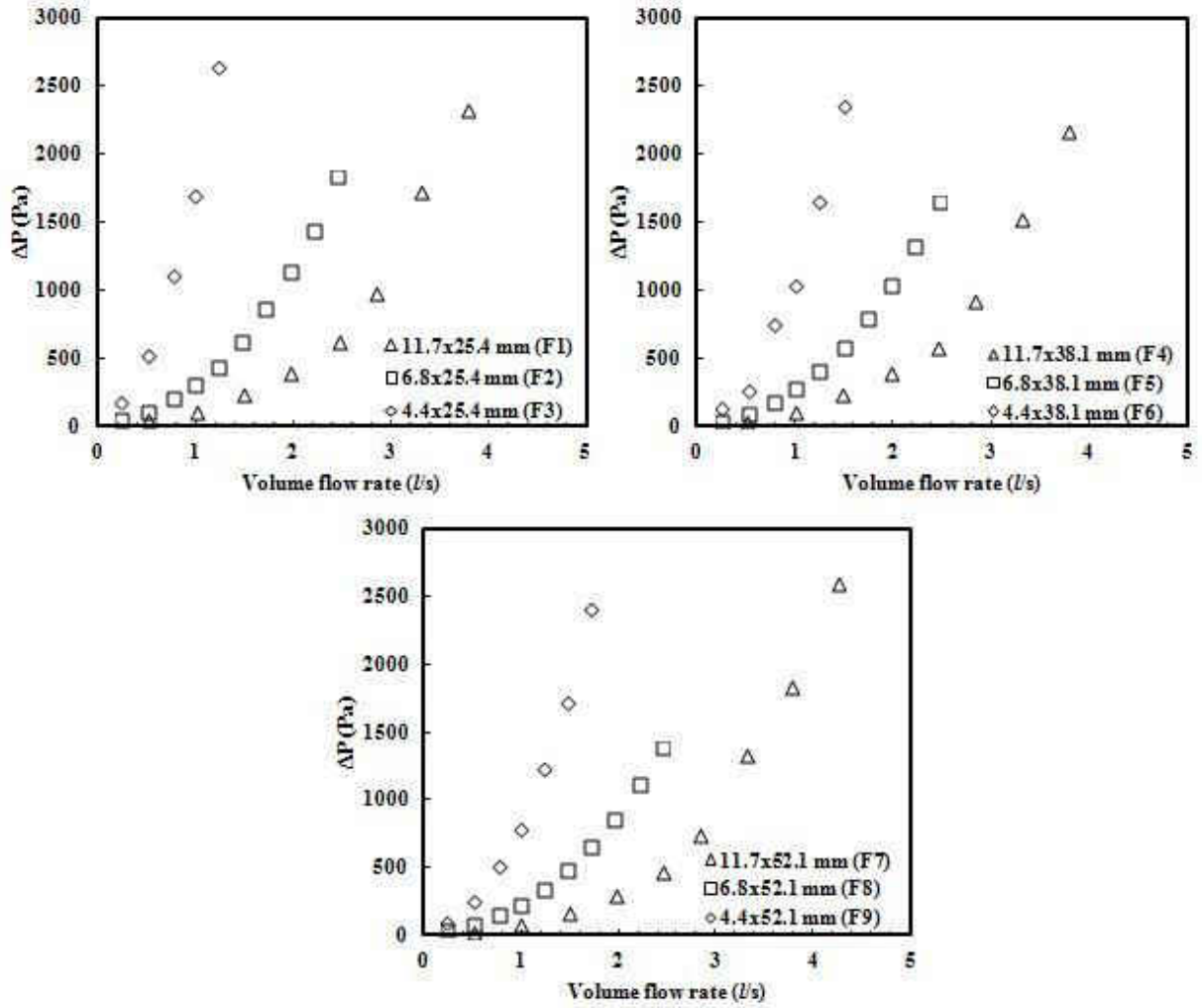


Figure 7. Effect of foam height on hydraulic performance

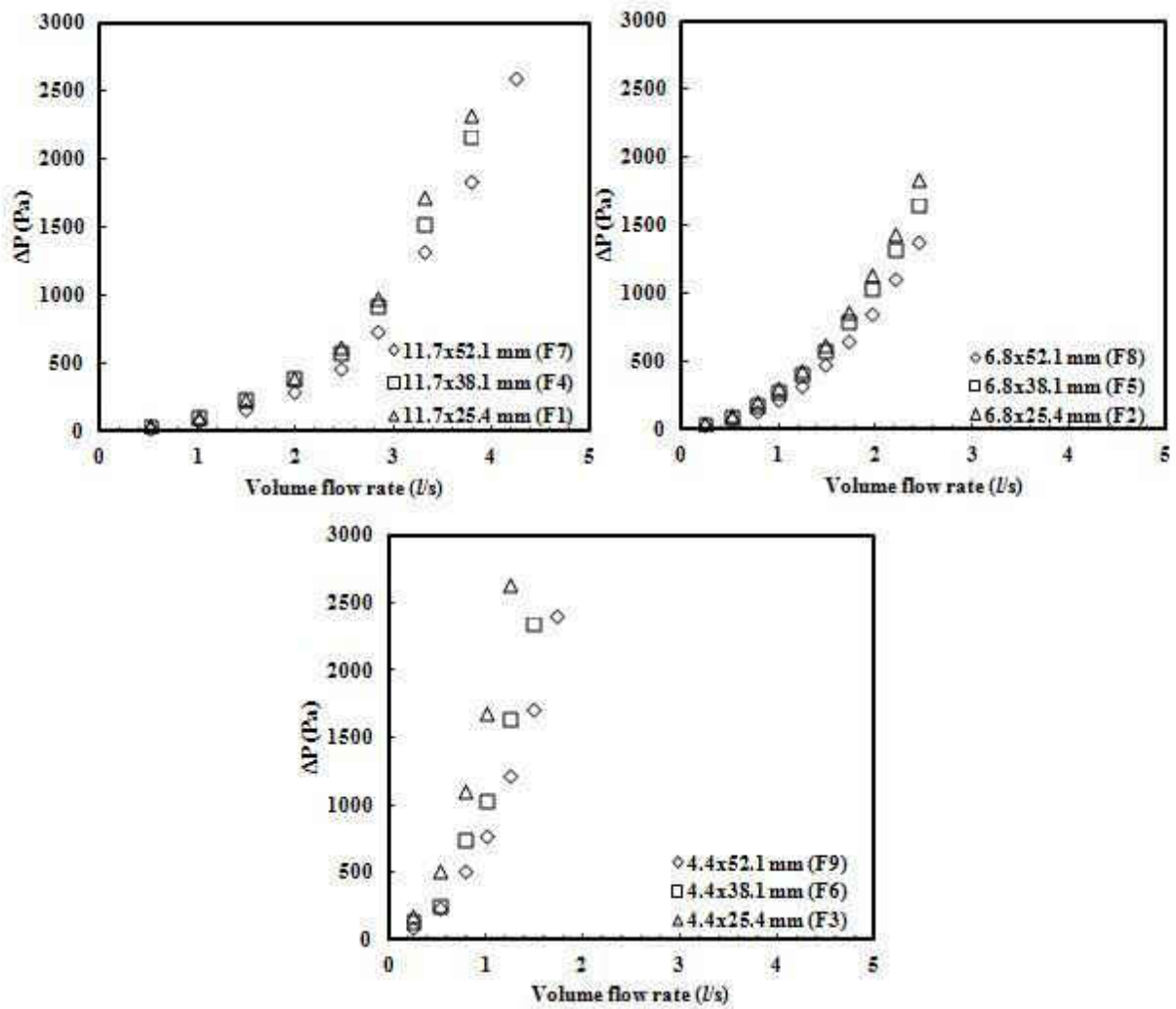


Figure 8. Effect of foam length on hydraulic performance

Garrity et al. [9] examined air-side heat transfer performance and pressure drop three carbon foam samples L1A, L1 and D1, manufactured by Kopper Inc., with pore sizes of 0.5, 0.6 and 0.65 mm, respectively. The three carbon foam samples were modified by machining 80 cylindrical holes, 6.7 mm apart with diameter of 3.2 mm in the flow direction, as shown in Figure 9. The bulk densities of the modified carbon foam samples are 284, 317, and 400 kg/m^3

respectively with porosity based on the flow passage of 0.166. The overall dimension for each of the three foam samples is 15.24x15.24x2.54 cm.

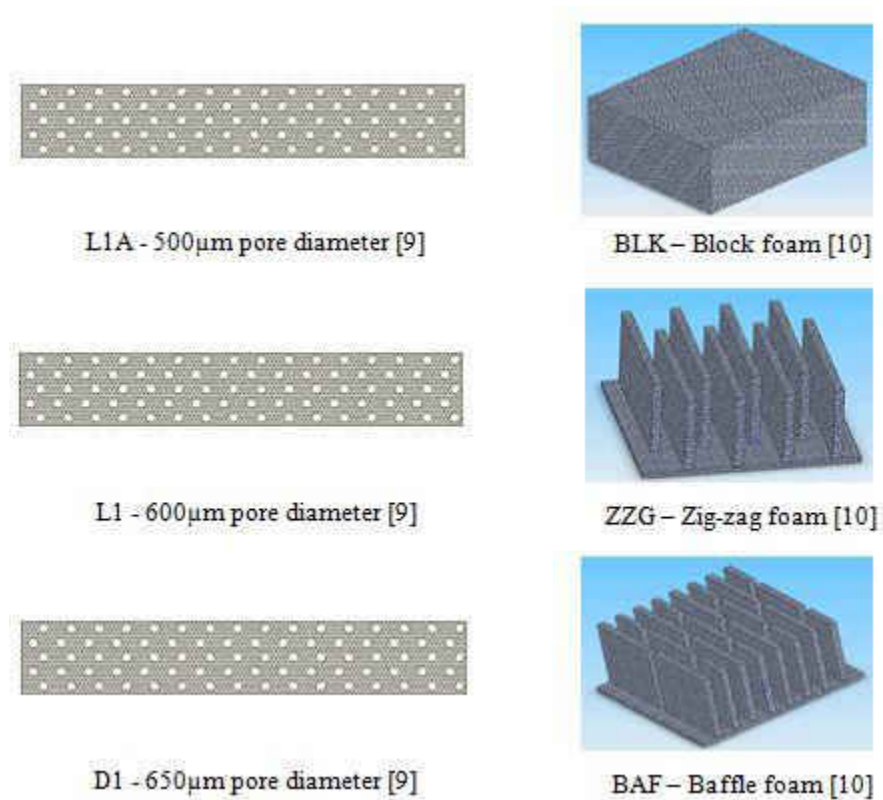


Figure 9. Foam configurations used for comparison with V-shape corrugated carbon foam

(Redrawn from references)

Leong et al. [10] studied the thermal and hydraulic performance of three geometries of PocoFoam with porosity of 72.8%. The three geometries are block foam (BLK), zigzag foam (ZZG) and baffle foam (BAF), as shown in Figure 9. All foam configurations have the same external dimensions of 50 x 50 x 25 mm.

Williams and Roux [11] tested three foam configurations for thermal management of power amplifiers. The tested geometries are inline, U-shape corrugated, and zigzag. All samples are

made of PocoFoam with porosity of 75%. The cooling channel was 65.3 mm wide and 3 mm height. Their measured pressure drop is very high (order of magnitude of 20 kPa).

Different criteria of choosing the appropriate length scale have been selected in [9-11]. In this study, the length scale used is the hydraulic diameter of the test channel as defined in Equation 2 therefore; recalculation is necessary for comparison. The width of the flow channel is W, its length is L and with height H.

$$d_h = \frac{4A_c}{P_w} = \frac{2W \cdot H}{(W + H)} \quad 2$$

Figure 10 shows a comparison between the F1 geometry of the V-shape corrugated foam and other foam geometries. The pressure drop across the F1 geometry is less than BAF, ZZG and BLK geometries. The pressure drop of L1A, L1 and D1 geometries is small because there are holes all the way down to the end of the foam. Although air is forced to go through the 2.5-mm thick porous wall of the F1 configuration (11.7x25.4 mm) the corresponding pressure drop is comparable to that of L1A, L1 and D1 geometries.

The heat transfer coefficient is highest for F1 geometry of the V-shape corrugated foam. It is somewhat surprising that heat transfer coefficient is even higher than that of the solid foam. This was explained in [12] and is due to better incoming air distribution in the V-shape corrugated foam over the heater section, and the fact that the solid foam needs only 4 mm in length to complete 95% of the heat exchange with the incoming air when the average air speed is at 4 m/s or less [13]. This short effective heat transfer length distance is due to its high thermal

conductivity and the small pore size (0.3 mm). Therefore, the longer the solid foam length, the worse is the average heat transfer coefficient.

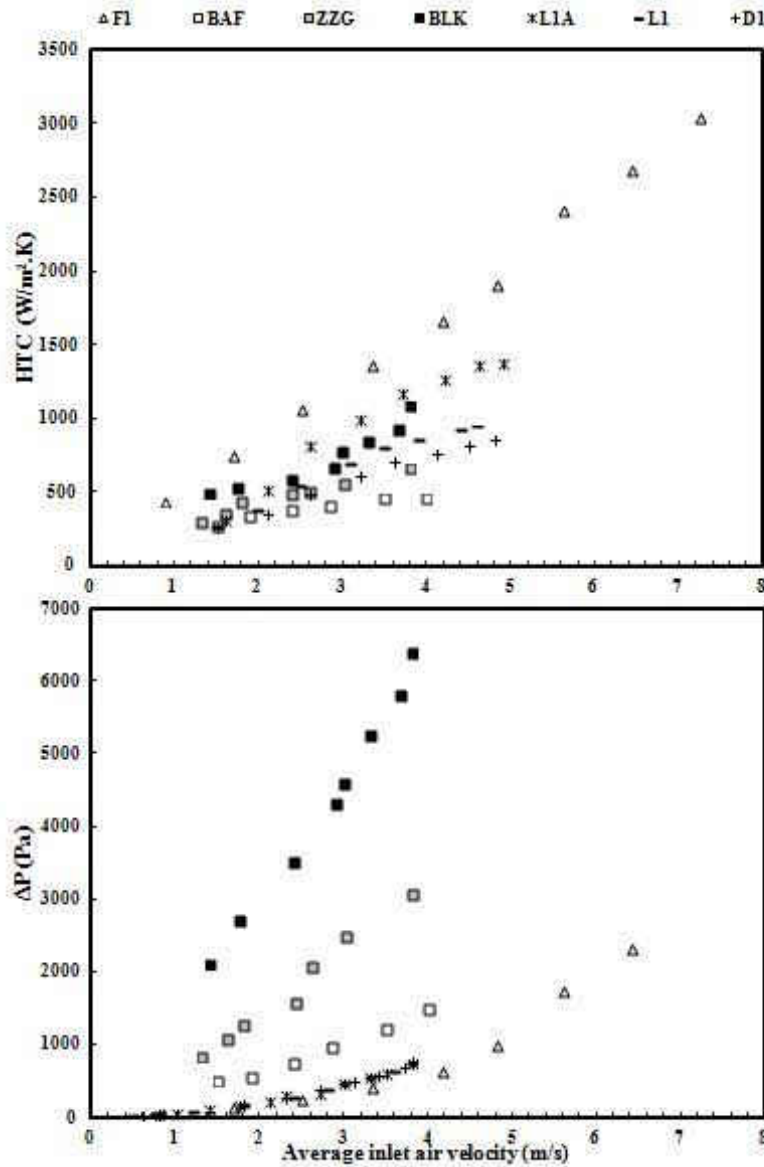


Figure 10. Comparison between V-shape corrugated foam and other foam geometries

The performance of carbon foam geometries can be assessed by the rate of heat transfer from the heated surface per unit temperature difference ($HTC.A_b$) with a specified fluid power. The

greater the ratio of the amount of the heat transfer rate per unit temperature difference that can be rejected to the fluid power is, the better is the foam performance.

To compare and judge the fifteen different foam geometries, we need to eliminate any geometrical dependency from the pressure drop and the heat transfer coefficient. Soland et al. [15] introduced the volumetric heat transfer coefficient and fluid power per unit volume as performance parameters which are defined in Equations 3 and 4. This volume V is defined as the gross volume of the protruding surface ($V=W.H.L$).

$$h_v = \frac{HTC \cdot A_b}{V} \quad 3$$

$$\frac{P}{V} = \frac{\dot{V} \cdot \Delta p}{V} \quad 4$$

Figure 11 shows the relation between the volumetric heat transfer coefficient and the fluid power per unit volume for the nine foam geometries (F1 to F9) as well as the other foam geometries (BAF, ZZG, BLK, L1A, L1 and D1). In general, the V-shape corrugated carbon foam shows the best volumetric heat transfer coefficient for the same fluid power per unit volume. This is because of the small values of pressure drop across the foam which is attributed to its small wall thickness (2.5 mm). This small wall thickness of the foam is sufficient to provide an efficient heat transfer process which leads to high heat transfer coefficient.

There is more than 220% enhancement in the volumetric heat transfer coefficient of the V-shape corrugated carbon foam when compared to BAF, ZZG and BLK geometries. The enhancement is 40% compared to L1A, L1 and D1 geometries.

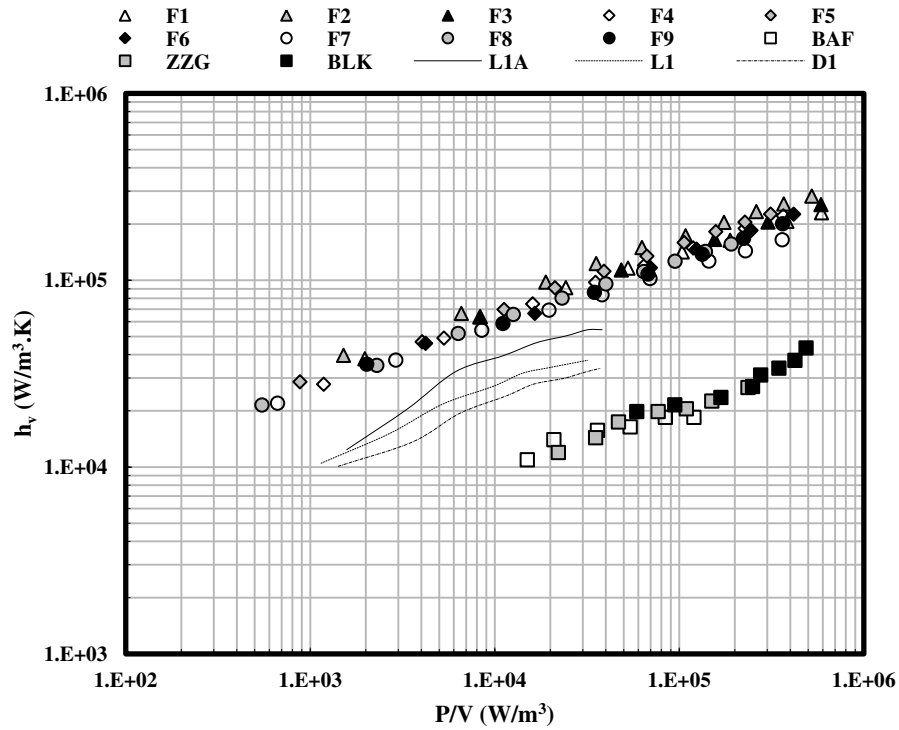


Figure 11. Volumetric HTC vs fluid power per unit volume

The fifteen geometries (F1 to F9, BAF, ZZG, BLK, L1A, L1 and D1) are introduced to enhance the heat transfer rate from flat surface exposed to a gas. Air is used as the working medium and since the operating temperature ranges in all these experiments are about the same, we can ignore variation in fluid properties. The relationship between the effectiveness of a heat exchanger (ϵ_f) and number of transfer units (NTU), defined in [Equations 5 & 6](#), is monotonic. Therefore, using NTU as a comparison criterion is appropriate to compare and judge the thermal performance of the foams. To incorporate the effect of the fluid power, we use the ratio of NTU to the fluid power as defined in [Equation 7](#).

$$\epsilon_f = \frac{T_{bo} - T_{bi}}{T_{fb} - T_{bi}} \quad 5$$

$$NTU = \frac{A_b \cdot HTC}{\dot{m} \cdot c_p} \quad 6$$

$$\frac{NTU}{P} = \frac{A_b \cdot HTC}{\rho \cdot \dot{V}^2 \cdot c_p \cdot \Delta p} \quad 7$$

The relation between the ratio of NTU to the fluid power with the average air velocity (U) for all foam geometries is shown in [Figure 12](#). At the same air velocity, all nine V-shape corrugated carbon foam geometries show a higher NTU per unit fluid power when compared to BAF, ZZG, BLK, L1A, L1 and D1 geometries.

There is at least 600% enhancement of the ratio of NTU to the fluid power of the V-shape corrugated carbon foam when compared to BAF, ZZG and BLK geometries. The enhancement is 200% when compared to L1A, L1 and D1 geometries.

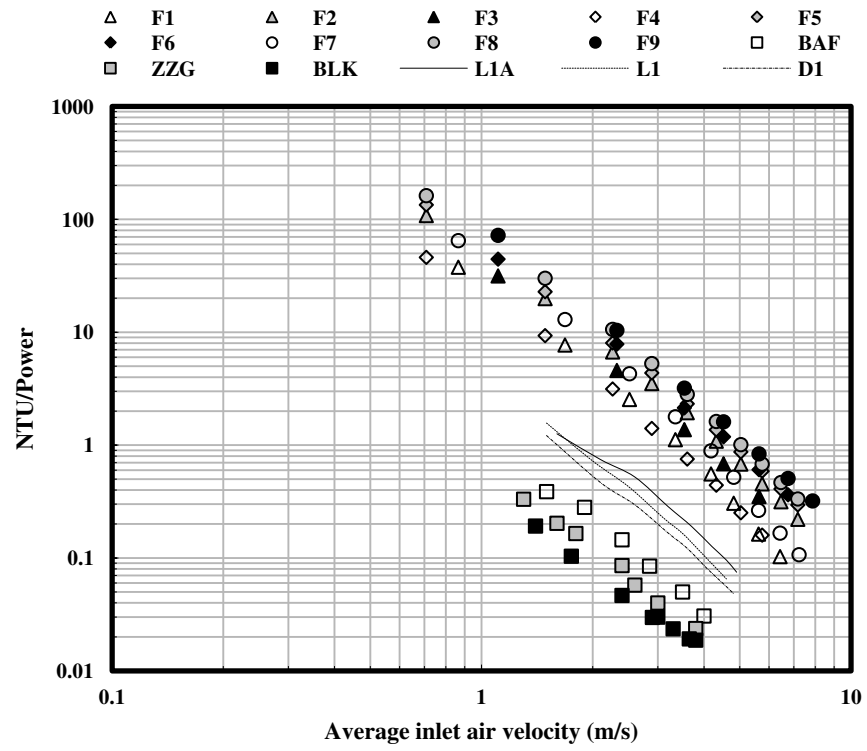


Figure 12. NTU per unit fluid power at different average air velocities

Conclusion

Thermal and hydraulic performance of the V-shape corrugated carbon foam was investigated. Nine different configurations of the foam were tested with respect to their height and length. A total of 81 test conditions were reported.

It was demonstrated that carbon foam is a very effective heat transfer medium because the heat exchange with air flowing through the foam can be accomplished within a small distance. From the performance point of view, a V-shape corrugated carbon foam of shortest length and tallest height gives the best combination.

V-shape corrugated carbon foam shows better performance when compared with other foam configurations. The benefit of using the V-shape corrugated carbon foam is the ability to obtain high ratio of the heat transfer rate to the fluid power required to remove the heat. In general, V-shape corrugated carbon foam shows at least a 40% increase in the volumetric heat transfer coefficient at the constant fluid power per unit volume. The foam also can achieve at least 200% increase in the ratio of NTU to the fluid power when compared to other foam geometries at the same air velocity.

CHAPTER THREE: CARBON FOAM SIMULATION AND ANALYSIS

Numerical Method

The four geometries of the V-shape corrugated carbon foam under study are illustrated in Figure 13 and described in Table 4. The effect of the length and the height of the geometry on the transport process was studied numerically and experimentally verified with respect to fluid flow and heat transfer parameters.

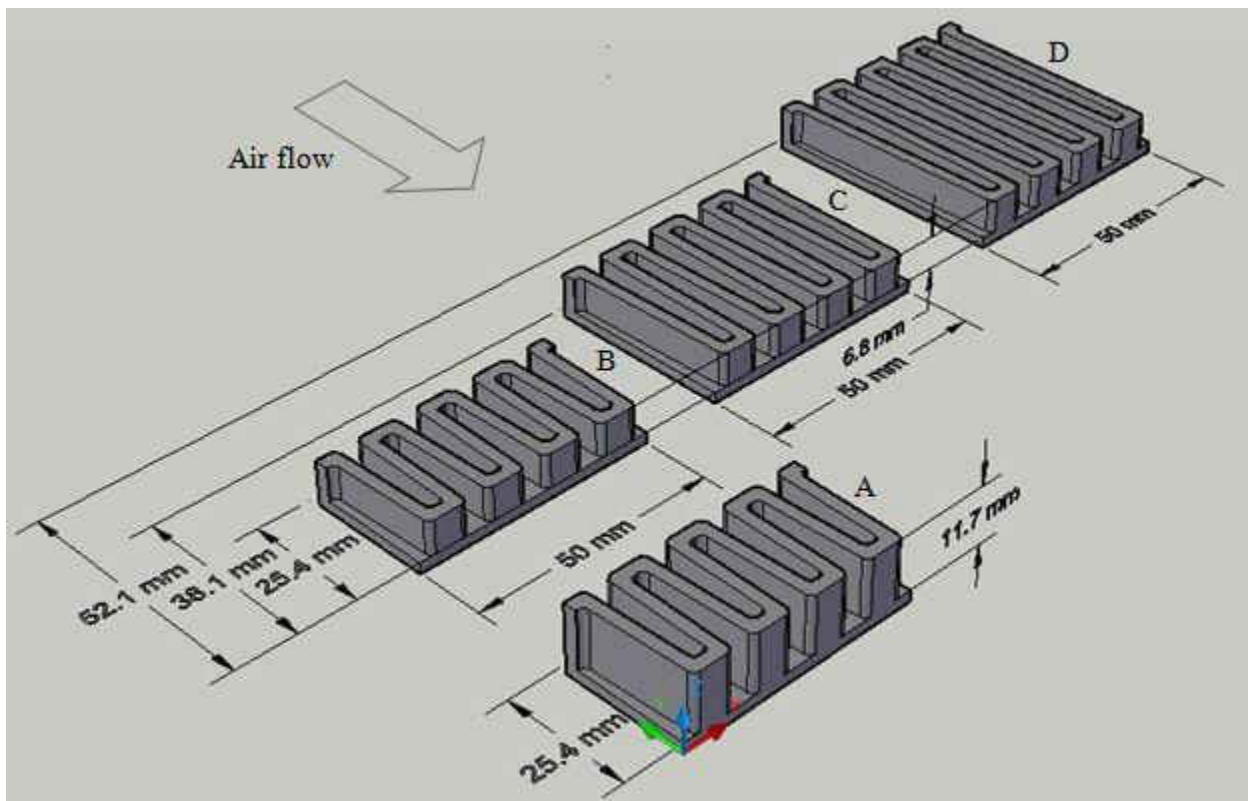


Figure 13. Geometry under study

Table 4. Foam geometries

Configuration	Width (mm)	Height x Length (mm)	V-shape vertex angle (degrees)	# of free channels	Wall thickness (mm)
A	50	11.7x25.4	3.76	4	2.5
B	50	6.8x25.4	3.76	4	2.5
C	50	6.8x38.1	2.26	4	2.5
D	50	6.8x52.1	1.66	4	2.5

The computational domain of any of these geometries can be divided into two domains, as shown in Figure 14: *The free air flow domain*, which consists of an empty channel occupied by air and *the porous matrix domain*, which consists of carbon foam and air.

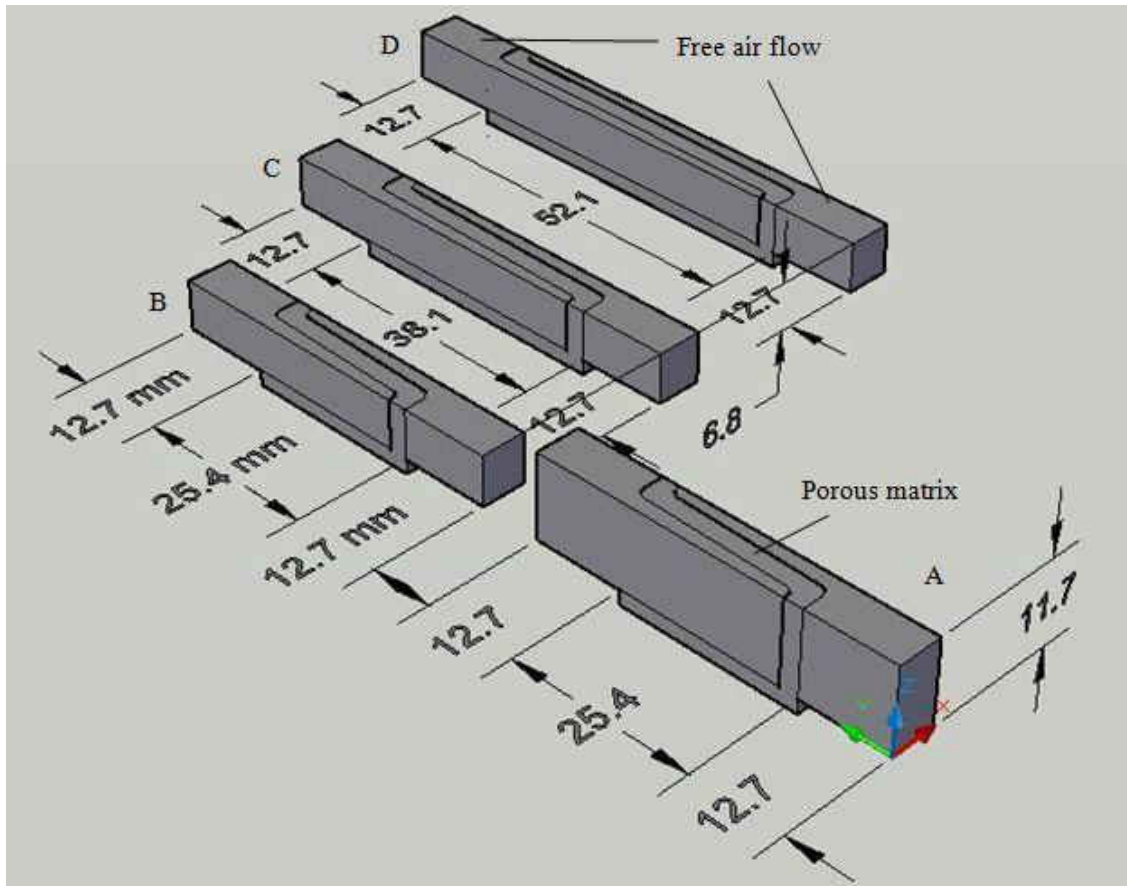


Figure 14. Computational domain

Finite Element Method (FEM) is used to solve for velocity, pressure and temperature fields in the computational domain using COMSOL Multiphysics software. The governing equations are as follows:

Free Air Flow

Continuity Equation

A steady flow of air with laminar condition occurs in the computational domain. The air density is function of temperature and pressure both of which varies with the position (x,y,z). Therefore, the variation of density has been taken into account and the continuity equation would be:

$$\nabla \cdot (\rho \mathbf{v}) = 0 \quad 8$$

Momentum Equation

The air is assumed to be Newtonian fluid and the air flow doesn't experience any volume force and the air dynamic viscosity is function of its temperature which changes with the position, the momentum equation therefore is:

$$\rho((\mathbf{v} \cdot \nabla) \mathbf{v}) = \nabla \cdot \left[-p \mathbf{I} + \mu \left(\nabla \mathbf{v} + (\nabla \mathbf{v})^T - \frac{2}{3} (\nabla \cdot \mathbf{v}) \mathbf{I} \right) \right] \quad 9$$

Energy Equation

In the present analysis, the variation in air thermal conductivity due to temperature change has been considered. With the assumption that the viscous dissipation term is neglected, the energy equation is:

$$\rho c_p \mathbf{v} \cdot \nabla T = \nabla \cdot (k \nabla T) \quad 10$$

Porous Matrix

Continuity Equation

Through the porous matrix, the air velocity is called Darcy velocity or the filtration velocity (v_f) and the air density is affected by the change in pressure and temperature. Therefore, the continuity equation is:

$$\nabla \cdot (\rho v_f) = 0 \quad 11$$

Momentum Equation

The flow in porous media is governed by Brinkman-Forchheimer-extended Darcy equation [16] in which, the porosity appears in the convective acceleration term, the momentum diffusion term and the component of the normal stress. Adding the pressure drop from Darcy law and Forchheimer drag, the momentum equation is:

$$\frac{\rho}{\varepsilon} \left((v_f \cdot \nabla) \frac{v_f}{\varepsilon} \right) = -\nabla p + \nabla \cdot \left[\frac{\mu}{\varepsilon} \left\{ (\nabla v_f + \nabla v_f^T) - \frac{2}{3} (\nabla \cdot v_f) I \right\} \right] - \frac{\mu}{K} v_f - \beta_F v_f^2 \quad 12$$

$$\text{where } \beta_F \text{ (Forchheimer coefficient)} = \frac{c_f \cdot \rho}{\sqrt{K}} \quad \& \quad C_f \text{ (inertia coefficient)} = \frac{3.5}{\sqrt{150 \cdot \varepsilon^3}}$$

Energy Equation

The air flow is laminar and the filtration velocities as well as the average inlet air velocities are limited to 4 m/s. The permeability of the porous matrix (K) is $1.5 \times 10^{-10} \text{ m}^2$. The air flow is steady and no heat generation occurs in the solid or fluid phase. Under these conditions, the LTE model is valid [17, 19, 20]. In this study, LTE condition is assumed and the temperature field in the energy equation describes the temperature of the porous matrix. Viscous dissipation term is neglected and the energy equation is:

$$\rho c_p v_f \cdot \nabla T = \nabla \cdot (k_{\text{eff}} \nabla T) \quad 13$$

where the effective thermal conductivity is defined as:

$$k_{\text{eff}} = (1 - \epsilon)k_s + \epsilon k_f \quad 14$$

Boundary Conditions

The symmetry of the geometry allows reducing the size of the computational domain eight times, as shown in [Figure 14](#), which allows reducing the computational time. Laminar flow of air enters the computational domain with an average of velocity (U) and the bottom is maintained at constant temperature (T_{fb}) as shown in [Figure 15](#). The boundary conditions used to solve this problem is tabulated in [Table 5](#) and shown in [Figure 15](#). At the interface between the two domains, continuity equation must be maintained along the interface, in other words, the mass flow rate of air enters the interface must be equal to the mass flow rate of air that leaves the interface. The air temperature and the shear stress are chosen to be continuous at the interface for both domains [\[16, 21\]](#).

Table 5. Boundary conditions

Symbol	Definition	Parameter	Value
a	Inlet	Average velocity (U)	0.71 up to 4 m/s
b	Outlet	Pressure	0
c	Wall	Velocity	0
d	Symmetry	$\hat{n} \cdot \nabla T$ & $\hat{n} \cdot \nabla v$	0
e	Temperature	Temperature (T_{bi} , T_{fb})	295 up to 334.4K
f	Outflow	$\hat{n} \cdot \nabla T$	0
g	Thermal Insulation	$\hat{n} \cdot \nabla T$	0

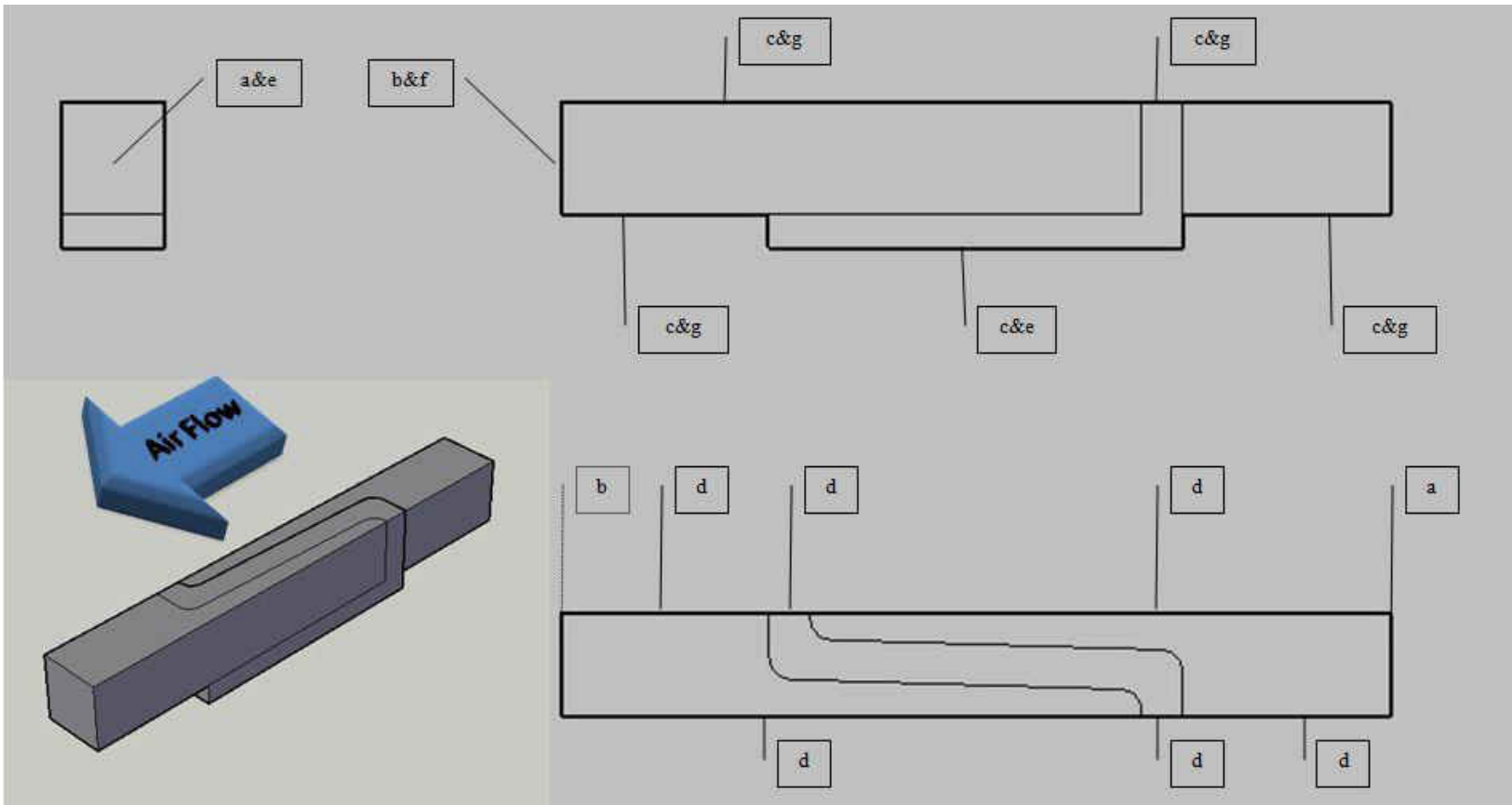


Figure 15. Boundary conditions

Problem Setup and Solution Procedure

Mesh independent solution has been verified for each of the four geometries, A, B, C and D where the number of mesh elements is 736K, 832K, 880K and 921K. The mesh of any of these geometries consists of tetrahedral, triangular, edge and vertex elements. The quality of an element is a value between 0 and 1, where 0 represents a degenerated element and 1 represents a completely symmetric element. The higher the quality of the mesh element the faster the convergence is. The average element quality for all geometries is 0.77.

The solution of the equations that governs the transport process of air was started by solving the continuity and momentum equations with coarse mesh to use the results of velocity and pressure fields as an initial guess. The next step is to solve for velocity and pressure fields with refined mesh. The process of mesh refinement was repeated until a mesh independent solution is reached. Then solving the energy equation coupled with the continuity and momentum equations to reach the final result of velocity, pressure and temperature fields. Convergence was considered to be achieved when the solver iterates until a relative tolerance of 10^{-6} is fulfilled.

Numerical Results and Discussion

The post-processing of the numerical data for the foam pieces A, B, C and D focuses on two parameters. *First*, the pressure drop across the foam which varies with the foam length and height. The pressure drop is of interest since it determines the pumping power required to flow the air through the foam therefore, it is desirable to have the least pressure drop through the foam to maintain the minimum pumping power. The pressure drop across the foam (Δp) can be characterized as:

- a. Pressure drop through variable area channel with porous walls (Δp_1).
- b. Pressure drop across the foam walls (Δp_2).

Air flowing across the V-shape corrugated carbon foam experiences the two pressure drops (Δp_1 & Δp_2). The total pressure drop (Δp) along a streamline is the sum of the two components since they can be considered as two flow resistances connected in series. If laminar air enters the computational domain, it was found that the air flow in the converging part of the free air flow domain has to be laminar too.

Second, the heat transfer coefficient which determines the heat rate that can be rejected from unit base area (A_b) with unit temperature difference between the base and the air inlet.

Carbon foam has anisotropic physical and thermal properties. Since the maximum height of the foam pieces under study is 11.7 mm therefore, it is reasonable to assume that the foam has constant porosity of 0.75, which is given by [10, 11, 31]. Thermal conductivity of carbon foam is a distinct anisotropic thermal property. The effective thermal conductivity of the foam in the growth direction of the graphite (k_{eff}) is 180 W/m.K while it is 40 W/m.K in the plane

perpendicular to the growth direction [1]. The permeability of the foam with air (K) is $1.5e^{-10} \text{ m}^2$ while as the inertia coefficient (c_f) is 0.44 [32].

Figure 16 shows the numerical results and experimental data for the relation between the average inlet air velocity and the pressure drop for different foam lengths with the same foam height (B, C and D). There is a good agreement between numerical results and experimental data. It is somewhat surprising that the total pressure drop across the foam decreases slightly with increasing the foam length. As air is forced to penetrate the foam wall of thickness of 2.5 mm, the local filtration velocity (v_f) crossing the foam wall decreases by increasing foam length since longer foam length means that the wall has larger overall surface area for the air to penetrate the foam. The uncertainty in pressure measurement equals to $\pm 1\%$ of the full scale value ($\pm 25 \text{ Pa}$).

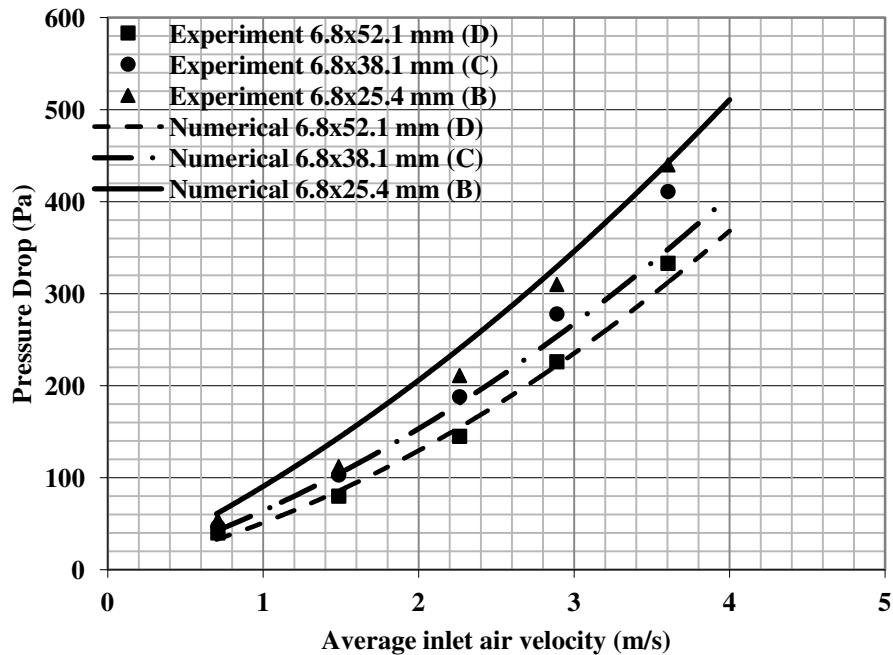


Figure 16. Effect of foam length on hydraulic performance

Figure 17 shows the relation between the average inlet air velocity and the pressure drop for different foam heights with the same foam length (A and B). As expected, changing the height of the foam does not affect the pressure drop. The uncertainty in pressure measurement equals to $\pm 1\%$ of the full scale value (± 25 Pa).

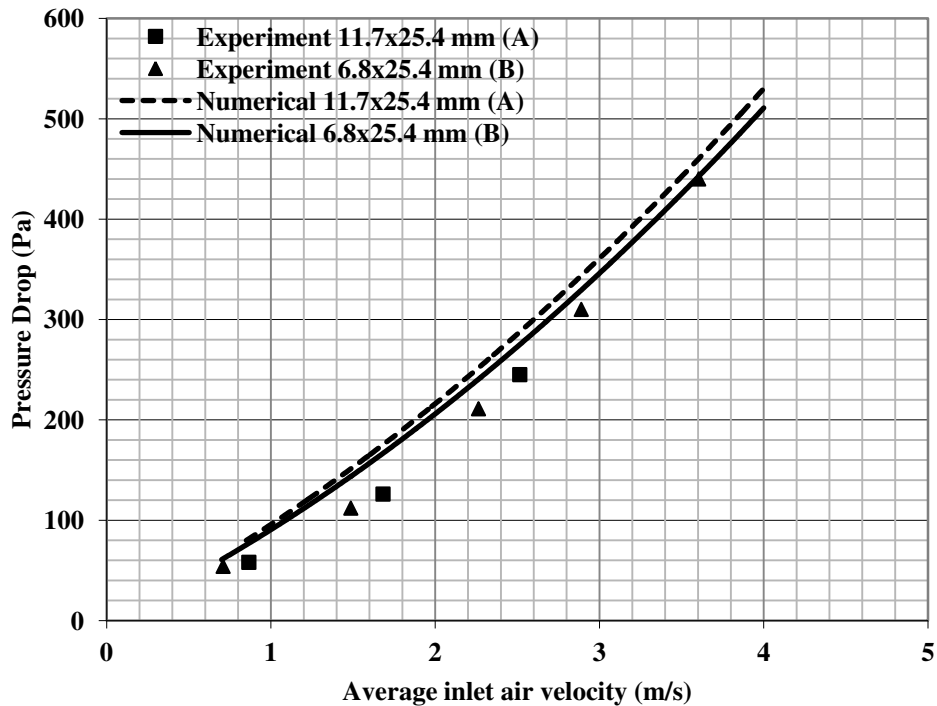


Figure 17. Effect of foam height on the hydraulic performance

It is reasonable to say that the base temperature of a heat sink reflects its efficiency of removing the heat at a same working conditions such as geometry, air velocity and heat load, so the closer the difference between the base temperature of the heat sink and the air inlet temperature, the higher the heat transfer coefficient is. From this prospective, the overall heat transfer coefficient (HTC) is defined based on the difference between the foam base temperature (T_{fb}) and the inlet air temperature (T_{bi}) as follows:

$$HTC = \frac{Q}{A_b \cdot (T_{fb} - T_{bi})}$$

15

In some cases under study (B, C and D) where the foam height is 6.8 mm, the air temperature approaches the foam base temperature at the exit section of the porous matrix, which means that the air picked up all the heat that it can to and the effectiveness (ϵ_f) in such cases is at least 98.8% as shown in [Table 6](#).

Table 6. Numerical results

Geometry	U (m/s)	T _{bo} (K)	T _{fb} (K)	ϵ_f %
B (6.8x25.4 mm)	0.71	339.4	339.6	99.6
	1.49	324.9	325.0	99.4
	2.26	316.9	317.1	99.2
	2.89	312.4	312.5	99.0
	3.60	308.3	308.5	98.8
C (6.8x38.1 mm)	0.71	336.7	336.8	99.7
	1.49	322.8	322.9	99.6
	2.26	315.1	315.3	99.4
	2.89	310.8	310.9	99.3
	3.60	306.9	307.0	99.1
D (6.8x52.1 mm)	0.71	335.6	335.7	99.7
	1.49	322.5	322.6	99.6
	2.26	315.2	315.3	99.5
	2.89	311.1	311.2	99.4
	3.60	307.4	307.5	99.3
A (11.7x25.4 mm)	0.87	336.5	337.3	98.2
	1.68	321.9	322.8	96.6
	2.51	313.3	314.4	94.5
	4	306.5	307.5	92.0

The boundary condition at the foam base is constant temperature which is measured in the experiment. The validation of the constant foam base temperature model is done by comparing the total heat rate transferred to the air from experiment and that from numerical results using the following equation:

$$Q = \dot{m}c_p(T_{bo} - T_{bi})$$

$$\text{where } T_{bi} = 295\text{K} \quad \& \quad \dot{m} = \iint_{\text{Exit area}} \rho v dA \quad \& \quad T_{bo} = \frac{1}{\dot{m}c_p} \iint_{\text{Exit area}} \rho c_p v T dA$$

The relation between the average inlet air velocity and the overall heat transfer coefficient for different foam lengths with the same foam height is illustrated in [Figure 18](#). At a fixed inlet air velocity and heat load, the variation of the base temperature for all foam pieces is a little, as illustrated in [Table 6](#). The base area of the foam is proportional to the foam length therefore; the base area ratio of the foams B, C and D is 1:1.5:2.05. The overall heat transfer coefficient is inversely proportional to the base area of the foam. For the same heat load, temperature difference and air velocity, the shorter the foam length, the higher is the overall heat transfer coefficient. The maximum uncertainty in the overall heat transfer coefficient calculation equals $\pm 7\%$.

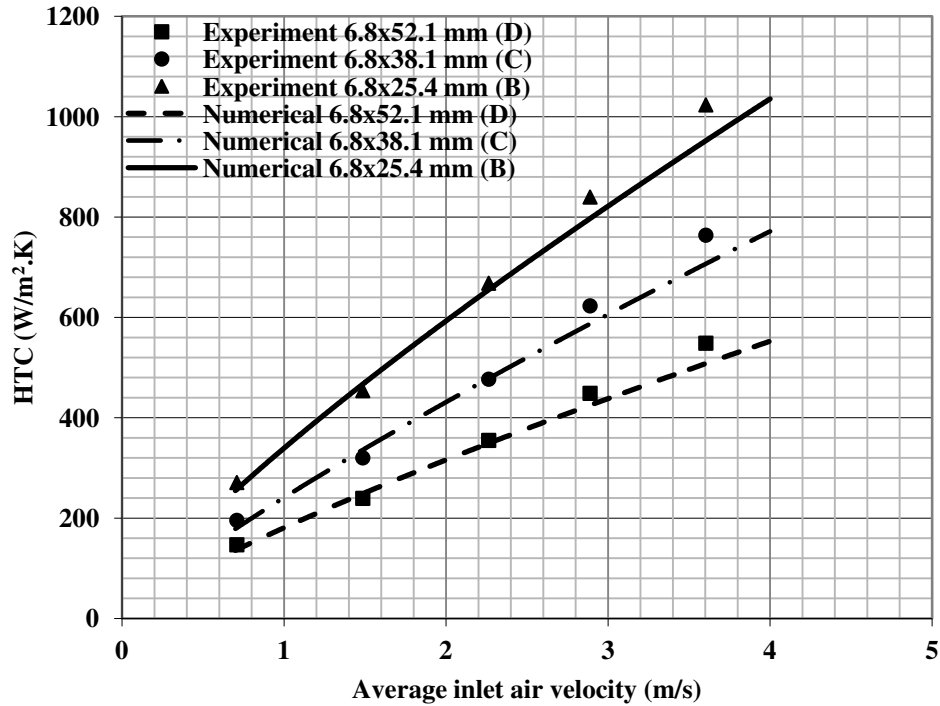


Figure 18. Effect of foam length on thermal performance

Figure 19 shows the relation between the average inlet air velocity and the overall heat transfer coefficient at different foam heights with the same foam length. There is an enhancement in overall heat transfer coefficient of the foam by increasing its height which is attributed to the increase of the mass flow rate of air at the same air velocity therefore, an increase in the heat transfer rate at the same foam base temperature as illustrated in Equation 16. The maximum uncertainty in the overall heat transfer coefficient calculation equals $\pm 7\%$.

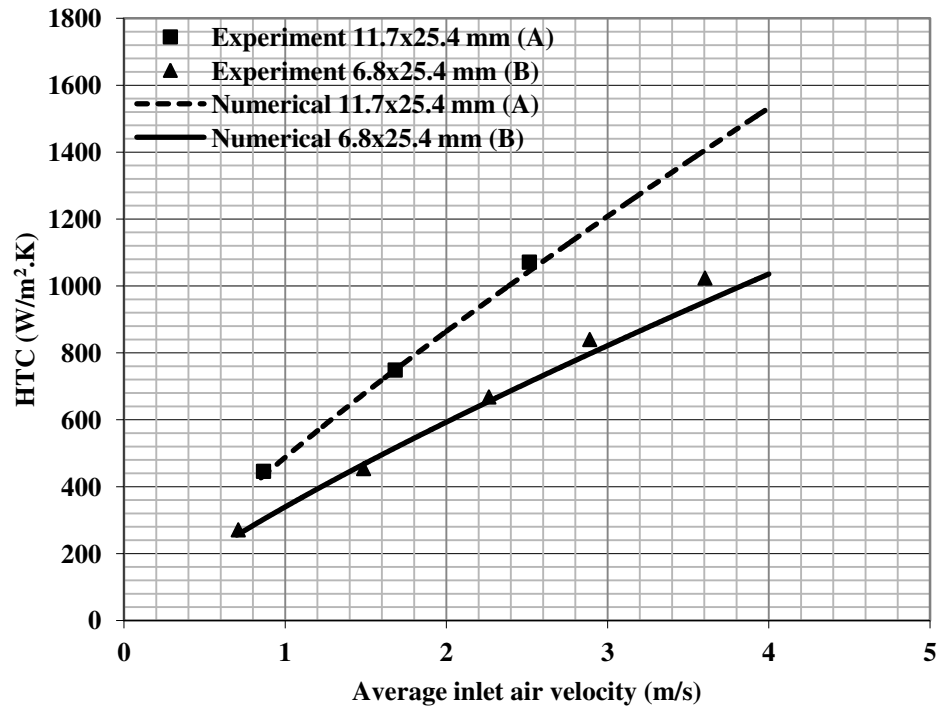


Figure 19. Effect of foam height on thermal performance

Analytical Method

Due to the open, interconnected void structure of the carbon foam, the flow through it can be considered as flow in minichannels connected in parallel. The minichannels have variable cross-section area therefore, the air velocity changes. Although the velocity changes along the flow path of air but the mass conservation has to be maintained. As a result, the average flow velocity through the foam can be defined as the filtration velocity (v_f) that satisfies the conservation of mass for a predefined area and fluid condition.

As air flows inside the minichannel, it picks up heat from the surface. After traveling a distance (x) on the order of several foam pore size ($d_p \approx 300 \mu\text{m}$), the air is able to pick more than 99% of the heat from the surface. This allows the air temperature to approach the surface temperature of the foam.

For the foam pieces B, C and D, the effectiveness of the minichannel and the foam (ϵ_m and ϵ_f respectively) are more than 98.8% as proven by numerical analysis and experiment, it is reasonable to assume that the foam base temperature (T_{fb}) equals to the minichannel surface temperature at a given height (T_{fs}) and equals to that of exit air from the minichannel. From the energy balance applied to the air inside the minichannel at a given air flow rate; the average overall heat transfer coefficient (HTC) can be calculated as follows:

$$\text{HTC} = \frac{\dot{m}c_p(T_{bo} - T_{bi})}{A_b \cdot (T_{fb} - T_{bi})} = \left(\frac{\rho \cdot A_c \cdot c_p}{A_b} \right) U = \left(\frac{\rho \cdot W \cdot H \cdot c_p}{W \cdot L} \right) U = \rho \cdot c_p \cdot \left(\frac{H}{L} \right) \cdot U \quad 17$$

We assume that the minichannels have a constant diameter (d_m) equals to half the pore size of the carbon foam ($d_p \approx 300 \mu\text{m}$). The effectiveness of the minichannel is $\epsilon_m = \frac{T_{bx} - T_{bi}}{T_{fs} - T_{bi}}$. Control

volume analysis on the air inside the minichannel defines the bulk air temperature distribution inside the channel as follows:

$$\left(\frac{T_{fs} - T_{bx}}{T_{fs} - T_{bi}}\right) = e^{-\left(\frac{P \cdot x \cdot \bar{h}_i}{\dot{m}_m \cdot c_p}\right)} = 1 - \epsilon_m \quad 18$$

where \bar{h}_i is the average interfacial heat transfer coefficient, based on the logarithmic mean temperature difference after distance (x) from the inlet, for the entrance and the fully developed regions combined [33] (Equation 19), P is the wetted perimeter, x is the distance measured from the inlet section to the minichannels and \dot{m}_m is the mass flow rate of air through one minichannel. The temperature dependency of Nusselt number which appears in the thermophysical properties of air (ρ , Pr, μ and μ_s), can be taking into account by referring to numerical and experimental results.

$$\bar{Nu} = \frac{\bar{h}_i \cdot d_m}{k} = 1.86 \cdot \left(\frac{Re \cdot Pr}{\left(\frac{x}{d_m}\right)}\right)^{\frac{1}{3}} \cdot \left(\frac{\mu}{\mu_s}\right)^{0.14} \cdot \begin{cases} \bar{Nu} \geq 3.66 \\ 0.6 \leq Pr \leq 5 \\ 0.0044 \leq \left(\frac{\mu}{\mu_s}\right) \leq 9.75 \end{cases}, \text{ combined regiems} \quad 19$$

$\bar{Nu} = 3.66$, fully developed

Conservation of mass on the air provides the filtration velocity (v_f) in terms of the average inlet air velocity (U) as illustrated in Equation 20.

$$\begin{aligned} \dot{m}_m &= \frac{\rho \cdot W \cdot H \cdot U}{n} = \rho \cdot v_f \cdot a_c \\ n &= \frac{R_{AV} \cdot V^*}{a_s} = \frac{R_{AV} \cdot L_f \cdot H \cdot t}{\pi \cdot d_m \cdot t} = \frac{R_{AV} \cdot L_f \cdot H}{\pi \cdot d_m} \\ v_f &= \frac{W \cdot H \cdot U}{n \cdot a_c} = \frac{W \cdot H \cdot U}{\left(\frac{R_{AV} \cdot L_f \cdot H}{\pi \cdot d_m}\right) \cdot \left(\frac{\pi}{4} \cdot d_m^2\right)} = \frac{4 \cdot W \cdot U}{R_{AV} \cdot L_f \cdot d_m} = \frac{W \cdot U}{L_f \cdot \epsilon} \end{aligned} \quad 20$$

where W and H are the foam width and height respectively, a_c is the cross-sectional area of one minichannel, a_s is the surface area of one minichannel, n is the total number of minichannels, t is the foam thickness, R_{AV} is the surface area to volume ratio of carbon foam, L_f is the total length of the corrugated foam wall and V is the volume of the foam.

The air volume in the porous matrix is the same as in the minichannels therefore, the minichannel diameter (d_m) is related to the surface area to volume ratio of carbon foam (R_{AV}) by:

$$V \cdot \varepsilon = n \cdot a_c \cdot t = L_f \cdot H \cdot t \cdot \varepsilon = \left(\frac{R_{AV} \cdot L_f \cdot H \cdot t}{\pi \cdot d_m \cdot t} \right) \cdot \left(\frac{\pi}{4} \cdot d_m^2 \right) \cdot t$$

$$R_{AV} \cdot d_m = 4\varepsilon \quad \& \quad \varepsilon \text{ is the foam porosity} = 75\% \tag{21}$$

The average interfacial heat transfer coefficient based on the logarithmic mean temperature difference (\bar{h}_i) and the average interfacial heat transfer coefficient based on $(T_{fs} - T_{bi})$ (\bar{h}_i^*) are related by:

$$\bar{h}_i \cdot \left(\frac{T_{bx} - T_{bi}}{\ln \left(\frac{T_{fs} - T_{bi}}{T_{fs} - T_{bo}} \right)} \right) = \bar{h}_i^* \cdot (T_{fs} - T_{bi})$$

$$\bar{h}_i^* = \bar{h}_i \cdot \left(\frac{\varepsilon_m}{\ln \left(\frac{1}{1 - \varepsilon_m} \right)} \right) \tag{22}$$

Analytical Results and Discussion

Air flows inside the interconnected void structure of the foam which can be considered as a flow inside conduits with variable cross-sectional area. The principle of hydraulic diameter allows simplifying this case into a constant diameter pipe (d_m). This simplification allows us to have better understanding of transport phenomena in carbon foam.

A comparison between analytical and numerical results is presented in [Table 7](#). The volume of the foam (V) is the volume that contributes in the heat transfer process between the air and the surface. Such volume can be calculated based on the length of the minichannel required to achieve 99.9% of the total heat transfer rate from the inlet ($t_{99.9\%}$) and this length is not the actual foam thickness (2.5 mm). It turns out that the surface area to volume ratio of the foam is 20000 (m^2/m^3) for the foam pieces B, C and D. This value agrees with the value range reported in literature [[10](#), [31](#)]. The corresponding minichannel diameter (d_m) can be calculated from [Equation 21](#), which is found to be 0.15 mm.

It is reasonable to assume that the foam base temperature (T_{fb}) is the same as the foam surface temperature (T_{fs}) at any height of the foam since the effectiveness of the foam is greater than 98.8% for the foam pieces B, C and D as shown in [Table 6](#). The effectiveness of the foam piece (A) ranges between 92% and 98.2%, which means that the variation in the foam temperature along its height is somewhat significant and therefore, the assumption is not as valid.

Table 7. Analytical and numerical results

Geometry	U (m/s)	R_{AV} (m^2/m^3)	d_m (mm)	$HTC_{analysis}$ ($W/m^2.K$)	$HTC_{numerical}$ ($W/m^2.K$)	ϵ_m (%)	$t_{99.9\%}$ (mm)	\bar{h}_i ($W/m^2.K$)	\bar{h}_i^* ($W/m^2.K$)
B (6.8x25.4 mm)	1	20000	0.15	314	348	99.9	0.295	659	95
	2	20000	0.15	627	568	99.9	0.589	659	95
	3	20000	0.15	941	804	99.9	0.883	659	95
	4	20000	0.15	1254	1076	99.9	1.177	659	95
C (6.8x38.1 mm)	1	20000	0.15	209	249	99.9	0.198	659	95
	2	20000	0.15	418	410	99.9	0.396	659	95
	3	20000	0.15	627	589	99.9	0.594	659	95
	4	20000	0.15	836	809	99.9	0.791	659	95
D (6.8x52.1 mm)	1	20000	0.15	153	186	99.9	0.146	659	95
	2	20000	0.15	306	301	99.9	0.291	659	95
	3	20000	0.15	459	428	99.9	0.436	659	95
	4	20000	0.15	612	576	99.9	0.582	659	95

A comparison between the calculated heat transfer coefficient, Equation 17, and numerical results for the foam pieces B, C and D is shown in Figure 20. The good agreement between the two results indicates that the heat transfer mechanism and the assumptions made in the analysis are valid. For the carbon foams with 6.8-mm height (B, C and D), the carbon foam acts as a fin with efficiency near unity.

Figure 21 shows the variation of the effectiveness along one minichannel for the foam pieces B, C and D at different face air velocities. As the filtration velocity increases, air needs a longer length to reach the same effectiveness. It is found that after a short distance from the inlet to the minichannel ≈ 1 mm, the bulk air temperature reaches at least 99.9% of the foam surface temperature as shown in Table 7.

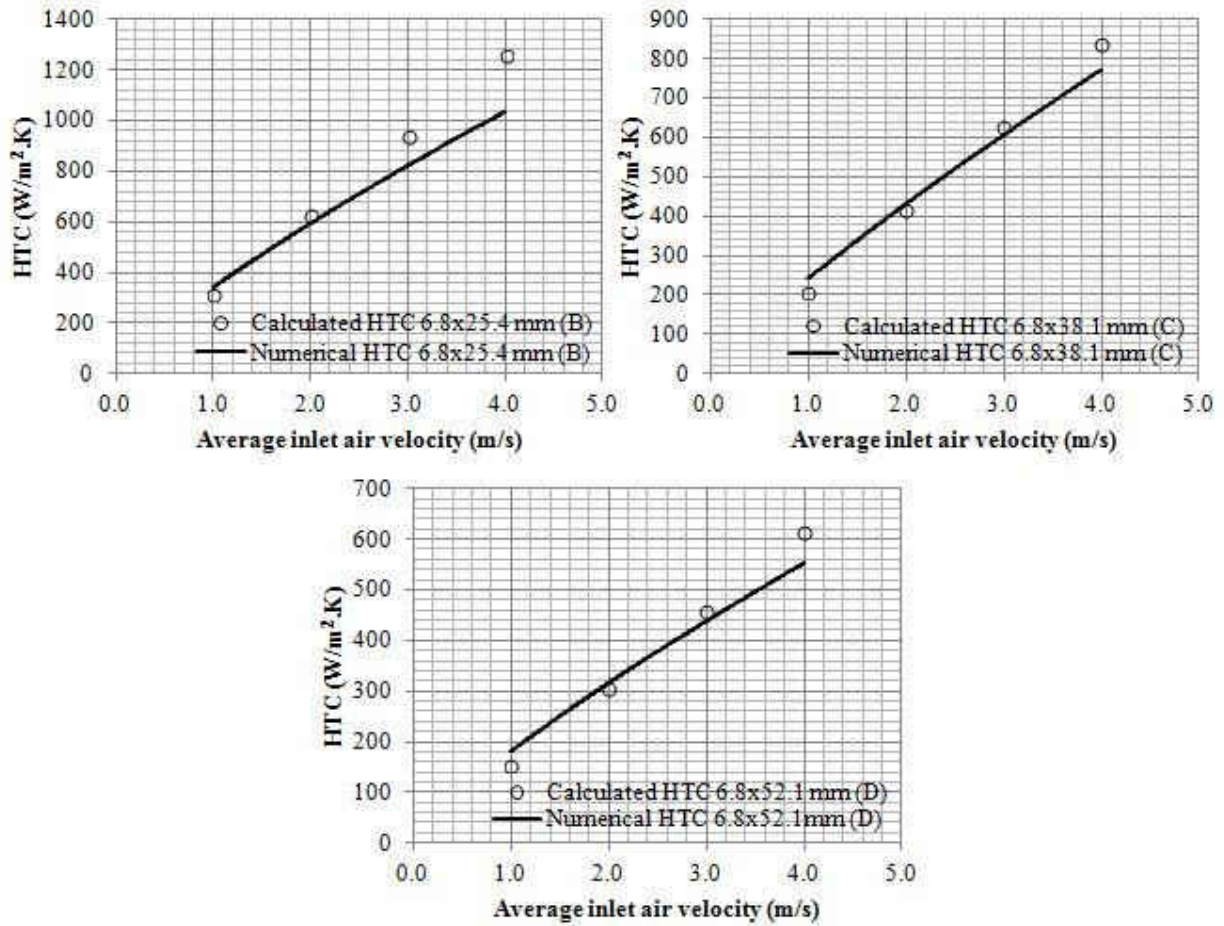


Figure 20. HTC analytical and numerical results

As the average inlet air velocity increases, the filtration velocity increases (Equation 20) and the average overall heat transfer coefficient increases (Equation 17). The position inside the minichannel at which 99.9% of the heat rate is transferred to the air varies with the average inlet air velocity. The variation of this position with the average inlet air velocity is illustrated in Table 7.

The temperature difference between the foam surface and air is the driving potential of the heat transfer process. This temperature difference decreases as air marches inside the minichannel.

Eventually after distance x from the inlet of the minichannel, the effectiveness of the minichannel approaches unity, therefore this temperature difference approaches zero leaving no potential for the heat to transfer as illustrated in [Equation 16](#). The relation between the average interfacial heat transfer coefficient based on $(T_{fs}-T_{bi})$ (\bar{h}_i^*) and the logarithmic mean temperature difference along one minichannel (\bar{h}_i) is illustrated in [Equation 22](#) and both values are given in [Table 7](#).

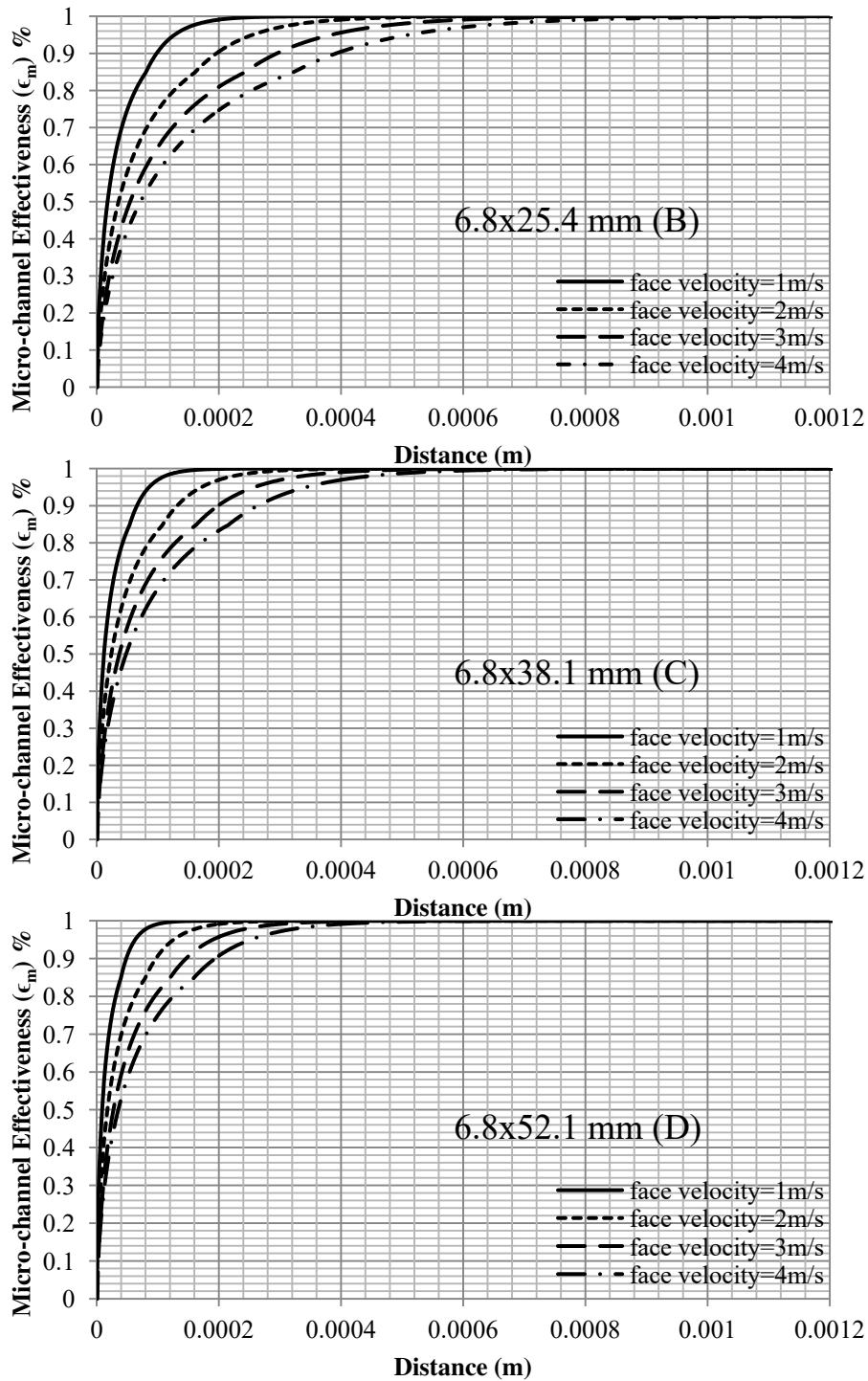


Figure 21. Variation of effectiveness along one minichannel

Conclusion

Numerical analysis of thermal and hydraulic characteristics of four V-shape corrugated carbon foam geometries was carried out. The pressure drop and the overall heat transfer coefficient for the four geometries were calculated. Numerical results were validated by experimental data with respect to the pressure drop, the heat transfer coefficient and the overall heat balance. For the given inlet air velocity range (0.71 - 4 m/s), the pressure drop ranges from 53 to 531 Pa and the heat transfer coefficient ranges from 186 to 1602 W/m².K. There is a good agreement between numerical and experimental results.

An analytical method is introduced by simplifying the flow in porous media into flow in minichannels connected in parallel. The minichannel diameter is assumed to be 0.15 mm while the surface area to volume ratio is 20000 m²/m³. The conservation of transport parameters was maintained in the analysis. Analytical results show that mass conservation requires the total length of the corrugated foam wall (L_f), the foam width (W) and foam porosity (ϵ) to be known. Numerical results revealed an important finding about the foam wall thickness required to achieve 99.9% of the heat transfer process. For the given air velocity range (0.711-4 m/s), It is found that ≈ 1 mm foam wall thickness is enough to complete the heat transfer process between the air and the foam.

CHAPTER FOUR: CARBON FOAM APPLICATIONS

Compact air-cooled heat sink is an essential component for electronics and aerospace applications. Compared to vapor-compression refrigeration, spray-cooled enclosures, and liquid-cooled manifolds, air-cooled heat sinks do not rely on the operation of the active pumps and compressors. Additionally, air-cooled heat sinks are worry-free of coolant leakage and many other related factors that increase the cost of the systems. In many electronics and aerospace applications, it is more practical to supply forced air flow to the components directly. Designers, therefore, would prefer implementing air cooling if its thermal performance could meet their requirements. For that reason, investigation of forced air convective heat transfer and pressure drop in a channel filled with V-shape corrugated carbon foams is of particular interest.

In chapter 2 and 3, experiment, simulation and analysis of the V-shape carbon foam demonstrate that the V-shape corrugated carbon foam is a very promising material for use in air cooling applications where high heat transfer coefficient with minimal pressure drop is required. In this chapter we introduce a practical evidence of the feasibility of the V-shape corrugated carbon foam of reducing the size of a traditional air-cooled condenser at the same heat load.

Case Study

The traditional air-cooled condenser available is shown in [Figure 22](#) with overall dimensions of (16.4 cm width x 4.7 cm height x 3.2 cm width). The heat transfer surface area is (16.4 cm x 3.2 cm x 10 surfaces) and air flow area of (16.4 cm x 4.7 cm). The air is supplied to the condenser by an axial fan Rotron aximax 2. This fan runs at 20000 rpm and is able to provide up to 0.025 m³/s (53 CFM) of air. The shut-off pressure is 685 Pa (2.75 inches of water).



Figure 22. Picture of the traditional air-cooled condenser

The pressure drop has a great interest in this analysis because it has to match the characteristics of the given fan. In fact, increasing the air face velocity will increase the heat transfer coefficient and the pressure drop as shown in chapter 2 and 3 however, this is limited to the fan capabilities and characteristics. The operating point has to be reasonable to supply sufficient air to cool down the condenser with appropriate pressure drop. The maximum air temperature difference can be achieved is 9 degrees (ideal case), if the inlet air temperature is fixed at 71°C, therefore to remove the heat out from the condenser at the rate 105 watts, the fan has to blow the air by at least 0.012 m³/s (24.6 CFM), as illustrated in [Equation 25](#).

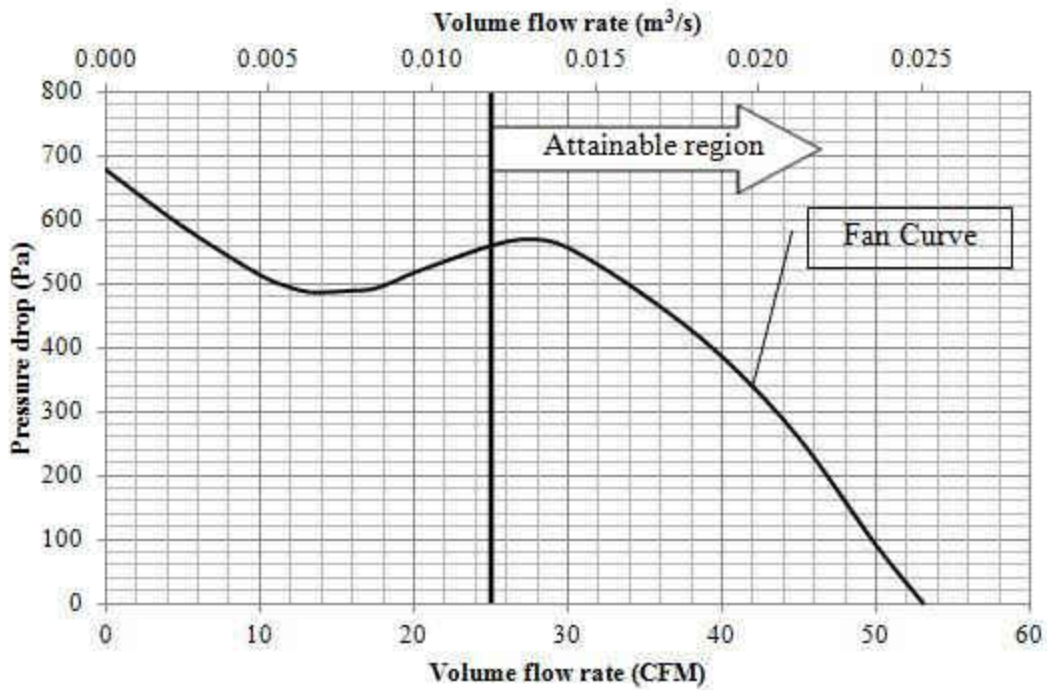


Figure 23. Attainable region of the fan curve

There is an attainable region for the fan to operate as shown in [Figure 23](#) with the pressure drop limited to 555 Pa (2.22 inches of water). The foam hydraulic characteristics is measured based on the air inlet velocity while the fan curve is a relation between the pressure drop and the air volume flow rate. In the design stage, different operating points can be obtained depending on the air flow area. The coupling between the fan and the foam is shown in [Figure 24](#).

$$Q = 105 = \dot{m} \cdot c_p \cdot (T_{bo} - T_{bi}) = HTC \cdot A_b \cdot (T_{fb} - T_{bi}) \quad 25$$

The operating conditions of this condenser are that the refrigerant R236fa is condensing at 80°C and the inlet air temperature is 71°C, this condenser rejects heat at a rate of 105 W. The

refrigerant flows inside 31 minichannels of 0.024 inches diameter (≈ 0.6 mm) as shown in Figure 22.

For design considerations and availability, the available height to fit the new condenser is 6.1 cm so the height of the new condenser is limited to 6.1 cm. The objective now is to design a new condenser with V-shape corrugated carbon foam inserts attached to the surface instead of aluminum fins to check its feasibility in terms of the size when coupled with the same fan to remove 105 W at the same working conditions.

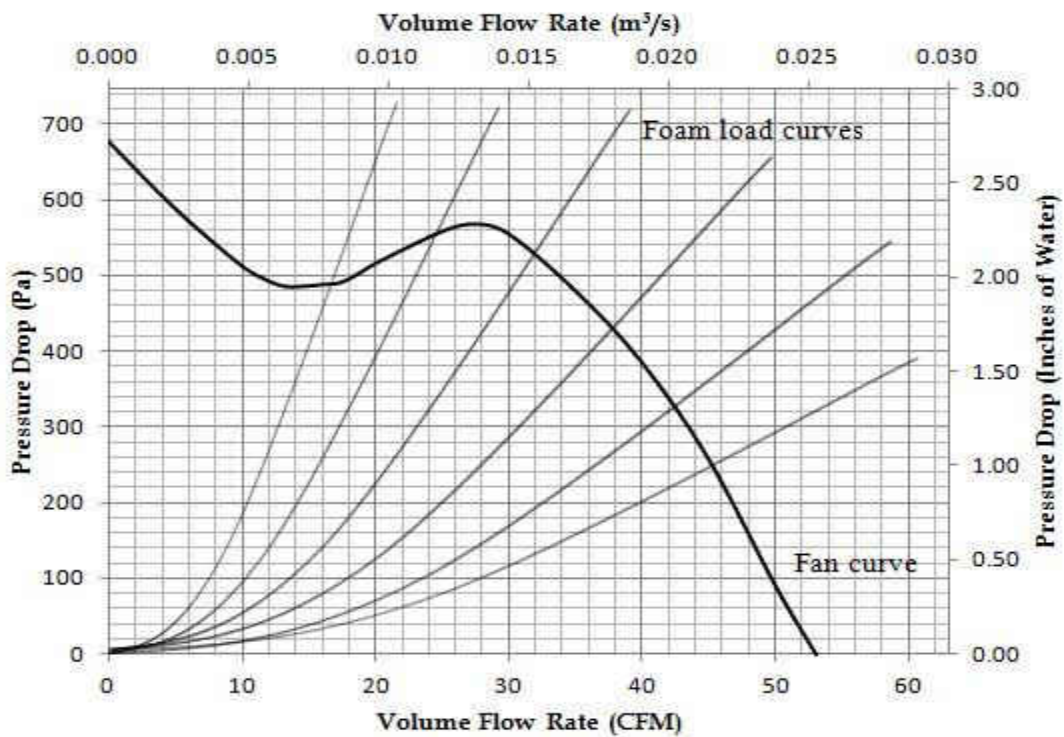


Figure 24. Fan and foam coupling

Condenser Analysis and Design

Based on design considerations and performance, the V-shape corrugated carbon foam piece of 6.8 mm height and 25.4 mm length is selected to replace aluminum fins. The height of the condenser will be fixed at 6.1 cm (2.4 inches) while its width (W^*) will be determined based on the criterion of removing 105 W from the condenser surface. The new condenser with the foam inserts is illustrated in [Figure 25](#). Air at 71°C flows inside a square duct of 6.1 cm height. Impermeable packing material is attached to the side bends of the condenser to prevent air leakage as shown in [Figure 25](#). The refrigerant gas comes from the gas inlet header which is located at the top of the condenser then through 25 minichannels of 0.024 inches diameter (≈ 0.06 mm). Number of minichannels is reduced from 31 to 25 because the width of the condenser decreased from 32 mm to 25.4 mm. The condensate liquid exits the condenser from the liquid header at the bottom of the condenser.

HTC is defined based on the difference in temperature between the foam base and the inlet air ($T_{fb}-T_{bi}$). This definition of the HTC allows simplifying the problem to one-dimensional heat transfer problem since the temperature potential is constant along thermal resistances everywhere within the condenser. Four cases are studied based on the condition of the refrigerant gas at inlet and the condition of the refrigerant liquid at exit. The calculation detail is shown in [Appendix C](#).

These cases are:

- **Case 1:** Inlet gas at 40° superheat, condensation at 80°C and liquid exits at 4°C subcooling.
- **Case 2:** Inlet gas at 40° superheat, condensation at 80°C and no subcooling.
- **Case 3:** No superheat, condensation at 80°C and liquid exits at 4°C subcooling.

- **Case 4:** No superheat, condensation at 80°C and No subcooling.

Assumptions:

1. One – dimensional heat transfer model.
2. Axial conduction is neglected (aluminum channel thickness < 0.5 mm).
3. Conduction resistance is neglected compared to the air side, refrigerant gas, refrigerant liquid and condensation resistances.
4. The variation of air properties is neglected ($\Delta T_{\max} = 9^\circ$).
5. The average temperature of the refrigerant gas and the refrigerant liquid will be used in calculation.
6. Contact resistance is neglected.

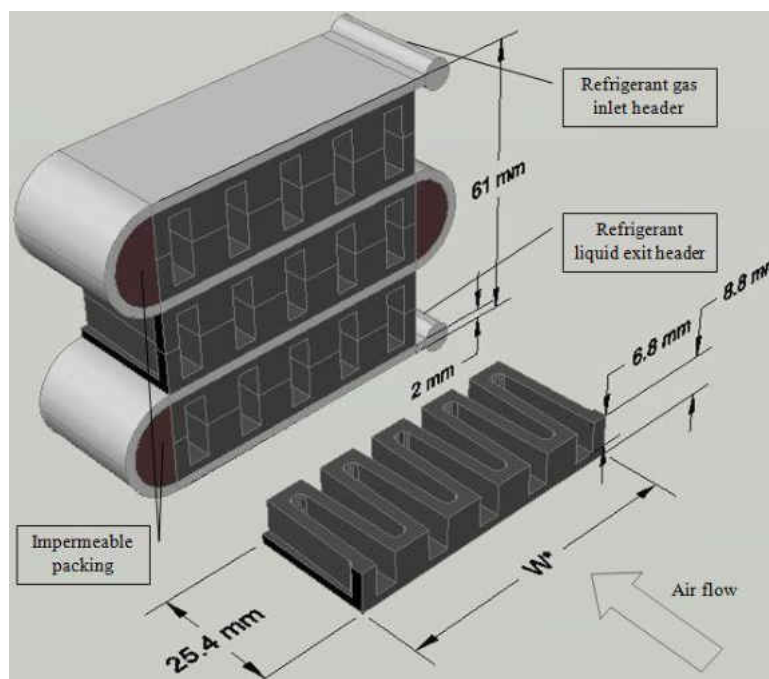


Figure 25. New condenser with carbon foam inserts

Results and Conclusion

Table 8 shows the analytical results of the new condenser design. Of the four cases considered in this analysis, case 2 requires the minimum condenser width (W^*) which is 71 mm. For all cases, the new condenser with V-shape corrugated carbon foam inserts beats the traditional aluminum finned condenser in terms of the overall size of the condenser and even the flow area. The new condenser is smaller in size than the traditional one by at least by 49%. Also the flow area is smaller by at least 36%. It is evident that using V-shape corrugated carbon foam can greatly help decreasing the size of the heat sink at the same heat load or it can help removing more heat for the same size of the heat sink.

Table 8. New condenser design parameters

	Foam Height (mm)	Foam Length (mm)	Condenser width W^* (mm)	New Dimension (mm)	Old Dimension (mm)	L_1 (cm)	L_2 (cm)	L_3 (cm)	T_{bo} ($^{\circ}$ C)	Area change %	Volume change %
Case (1)	6.8	25.4	73.7	74x61x25	102x47x32	32	8	3.6	79.7	-42	-54
Case (2)			71.1	71x61x25		33	8.8	N/A	80	-44	-55
Case (3)			81.3	81x61x25		45	N/A	4	78.9	-36	-49
Case (4)			78.7	79x61x25.4		47	N/A	N/A	79.1	-38	-50

CHAPTER FIVE: HIGHLY ORIENTED PYROLYTIC GRAPHITE (HOPG) Introduction

Natural graphite structure is usually amorphous because of defects and impurities contained within the structure. Many technologies are developed to prepare perfect graphite samples. Of these, pyrolysis is the most common and effective technique. Pyrolysis is a thermochemical decomposition of organic material at high temperatures with the absence of oxygen, water or any other reagents. It involves the simultaneous change of chemical composition and physical phase. Highly oriented pyrolytic graphite (HOPG) is a graphite material with a high degree of preferred crystallographic orientation in the plane perpendicular to the surface of the substrate (z-plane or out-of-plane). HOPG is obtained by graphitization heat treatment of carbon or by chemical vapor deposition at temperatures above 2500K then annealed under pressure at approximately 3300K.

The density, parameters of the crystal lattice, preferable orientation in the plane of the surface of the substrate and anisotropy of thermal and physical properties of the HOPG are close to those of natural graphite. The crystal structure of HOPG is uniquely characterized by the arrangement of carbon atoms which are stacked in parallel layers. In each layer, atoms form a grid of exact hexagons with distance between two adjacent atoms in xy plane (in-plane) equals 0.1415 nm. The distance between two adjacent atoms in two different layers equals 0.335 nm. [34, 35] as shown in [Figure 26](#).

Graphite structure by itself is anisotropic, because coupling in xy planes is due to the mutual strong bonds, whereas in z-planes, coupling is weak. The structural anisotropy results in

anisotropy of thermal properties like thermal conductivity [36]. HOPG is graphite with more crystalline perfection due to high temperature and pressure treatment.

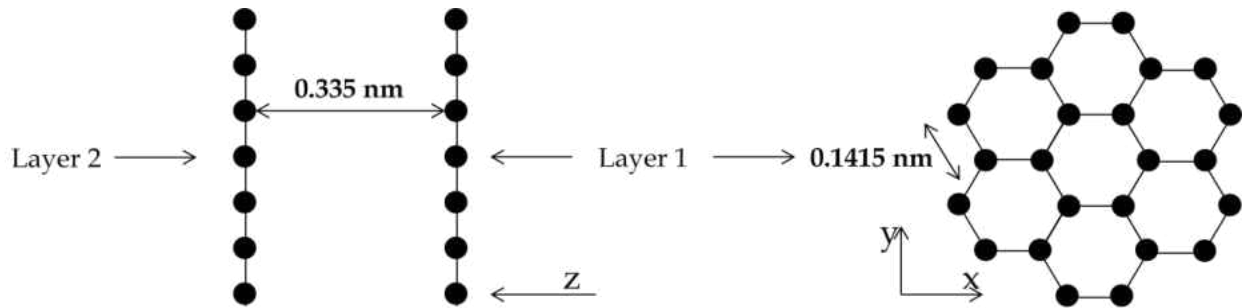


Figure 26. Crystal structure of HOPG

The in-plane thermal conductivity k_{xy} of HOPG is about 1700 W/m.K which is four to five times that of copper and the out-of-plane thermal conductivity k_z of about 8 W/m.K at room temperature. Figure 27 shows HOPG material's thermal conductivities k_{xy} and k_z as function of temperature and the anisotropy ratio (k_{xy}/k_z) [37, 38].

Therefore, HOPG is a highly anisotropic material with distinct thermal properties which can be useful in thermal applications in which axial conduction is crucial and needed to be minimized such as cryocoolers and recuperators. Due to its high thermal conductivity in xy plane, HOPG can also be very useful to produce effective micro-channels for high heat flux applications.

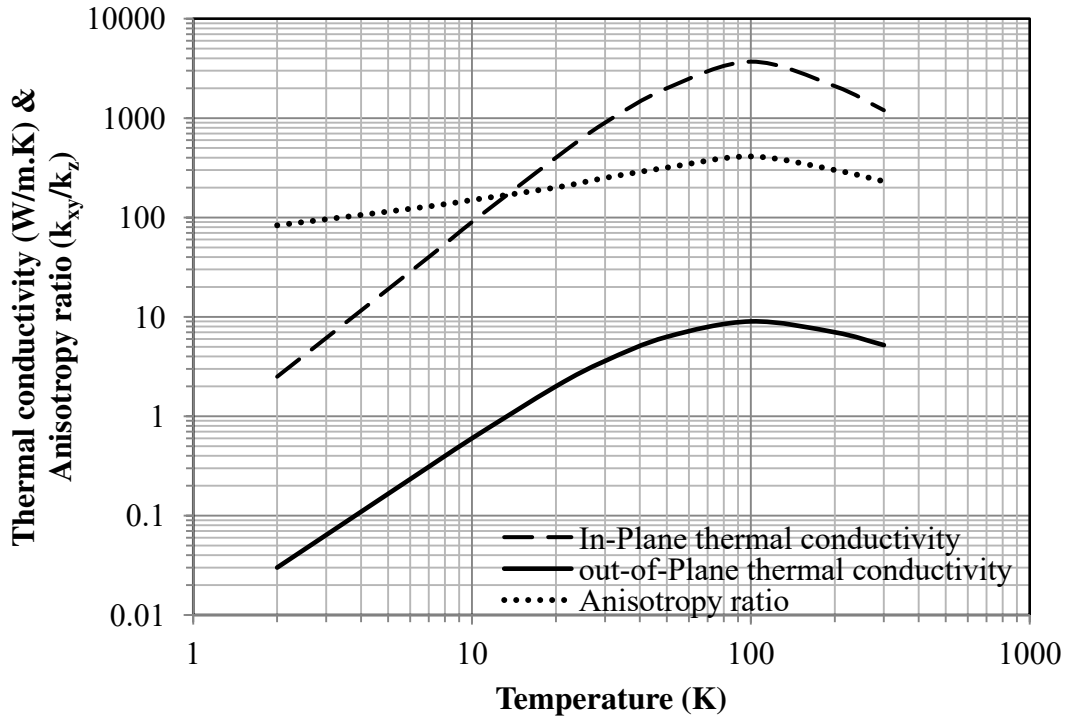


Figure 27. In-plane thermal conductivity k_{xy} , out-of-plane thermal conductivity k_z and anisotropy ratio as a function of temperature

To implement HOPG in thermal management application, machining of the HOPG is required. Different machining techniques are introduced in literature [39-41]. Park et al. [39] made 100 nm holes on HOPG surface using a metal-coated atomic force microscope (AFM). Song et al. [40] fabricated various nanostructures on HOPG based on mechanical machining and field evaporation. The basic idea is to transfer a known pattern into an encoded voltage pulse series and synchronize it with scanning probe microscopy (SPM). Hole drilling and polishing of HOPG was performed by Windholz and Molian [41] by a laser beam of a 248 nm wavelength, 23 ns pulse. The depth removed per pulse is 0.3 μm .

HOPG Micro-Channel

Thermal performance of a micro-channel made of thermal conductors like copper and aluminum will be compared to that made of HOPG at the same working conditions. Fluid flow is allowed to enter a micro-channel of height H^* and spacing L^* between two adjacent walls of thickness t^* and the micro-channel base is subjected to a heat source supplying heat at a rate of Q , as shown in Figure 28. A key thermal performance factor of micro-channel is the heat transfer rate that can be removed from the base. Hence we want to put as many fins as possible (meaning we want to keep t^* and L^* to a minimum, resulting in the maximum number of fins). The number of fins is usually limited by the pressure drop. At the same time, we like to have the fins as tall as possible (meaning high H^*). However, we need to keep high fin efficiency. Typical high-performance micro-channels are made of copper, with $L^* \sim 25$ microns, t^* and H^* are designed to have high fin efficiency. $t^* \sim L^*$, and $H^* \sim 500$ microns or less. HOPG allow H^* to be larger, while keeping t^* and L^* the same.

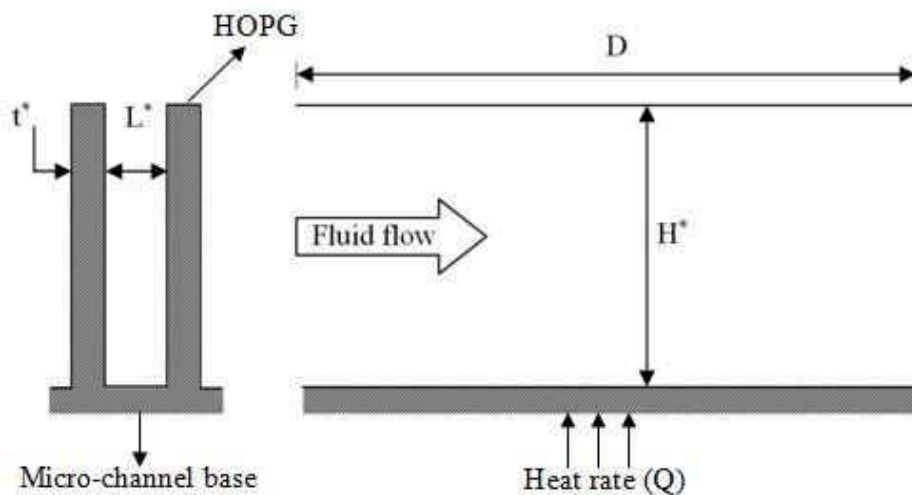


Figure 28. Micro-channel model

For design considerations, the wall of the micro-channel can be considered as a long fin with efficiency (η_f) since no enhancement is expected to occur in thermal performance by increasing the wall height.

$$\eta_f = \frac{q_f}{q_{\max}} = \frac{\sqrt{\text{HTC} \cdot P_w \cdot k \cdot A_c} \cdot \theta_b}{\text{HTC} \cdot P_w \cdot H^* \cdot \theta_b}$$

$$\eta_f = \frac{1}{H^*} \cdot \sqrt{\frac{k \cdot A_c}{\text{HTC} \cdot P_w}}$$

$$\eta_f = \frac{1}{H^*} \cdot \sqrt{\frac{k \cdot t^* \cdot D}{\text{HTC} \cdot 2(D + t^*)}} \quad \& \quad t^* \ll D$$

$$\eta_f = \frac{\sqrt{k}}{H^*} \cdot \sqrt{\frac{0.5t^*}{\text{HTC}}}$$

From [Equations 18 & 19](#) with the fact that the $t^* \approx L^* \ll H^* \& D$:

$$\text{HTC} \propto \frac{1}{L^*}$$

$$H^* = \sqrt{k} \frac{\sqrt{0.5t^* \cdot L^*}}{\eta_f}$$

For the same fin efficiency (η_f), micro-channel wall thickness (t^*) and micro-channel wall spacing (L^*):

$$\therefore H^* \propto \sqrt{k}$$

$$\frac{H_{\text{HOPG}}^*}{H_{\text{copper}}^*} = \sqrt{\frac{k_{\text{HOPG}}}{k_{\text{copper}}}} \cong \sqrt{\frac{1700}{400}} = 2.1$$

$$\frac{H_{\text{HOPG}}^*}{H_{\text{aluminum}}^*} = \sqrt{\frac{k_{\text{HOPG}}}{k_{\text{aluminum}}}} \cong \sqrt{\frac{1700}{205}} = 2.9$$

By replacing copper or aluminum with HOPG, the micro-channel height increases 2-3 times at the same fin efficiency. As a result, more mass flow rate of the fluid is allowed to flow inside the channel. In return, the heat capacity of the fluid increases 2-3 times. Since the fin efficiency is the same, fluid outlet temperature is expected to be constant by varying the micro-channel material, therefore:

$$\frac{Q_{\text{HOPG}}}{Q_{\text{copper}}} = \frac{\dot{m}_{\text{HOPG}} \cdot c_p \cdot \Delta T}{\dot{m}_{\text{copper}} \cdot c_p \cdot \Delta T} = \frac{\dot{m}_{\text{HOPG}}}{\dot{m}_{\text{copper}}} = \frac{H_{\text{HOPG}}^*}{H_{\text{copper}}^*} \cong 2.1$$

$$\frac{Q_{\text{HOPG}}}{Q_{\text{aluminum}}} = \frac{\dot{m}_{\text{HOPG}} \cdot c_p \cdot \Delta T}{\dot{m}_{\text{aluminum}} \cdot c_p \cdot \Delta T} = \frac{\dot{m}_{\text{HOPG}}}{\dot{m}_{\text{aluminum}}} = \frac{H_{\text{HOPG}}^*}{H_{\text{aluminum}}^*} \cong 2.9$$

This result implies that more heat can be removed efficiently from the HOPG micro-channel. The high in-plane thermal conductivity of HOPG, which is greater than copper and aluminum, allows increasing the height of the micro-channel. This translates to an increase of the rate of heat transfer by two or three times.

APPENDIX A: UNCERTAINTY ANALYSIS

Design Stage Uncertainty

Differential Pressure Measurement

$$U_z = 0.5 * \text{resolution} = 0.5 * 0.01" = 1.25 \text{ Pa}$$

$$U_c = \sqrt{(0.01 * 2491)^2} = 24.91 \text{ Pa}$$

$$U_d = U_{\Delta p} = \sqrt{(U_z^2 + U_c^2)} = \sqrt{(1.25^2 + 24.91^2)} = \pm 24.9 \text{ Pa (95\% confidence level)}$$

Volume Flow Measurement

OMEGA FL-2035

$$U_z = 0.5 * \text{resolution} = 0.5 * (2) = 1 \text{ CFH}$$

$$U_c = \sqrt{(0.03 * 100)^2} = 3 \text{ CFH}$$

$$U_d = U_{\dot{V}} = \sqrt{(1^2 + 3^2)} = \pm 3.16 \text{ CFH} = \pm 2.49 * 10^{-5} \left(\frac{\text{m}^3}{\text{s}} \right) \text{ (95\% confidence level)}$$

OMEGA FL-2060

$$U_z = 0.5 * \text{resolution} = 0.5 * (0.1) = 0.05 \text{ CFM}$$

$$U_c = \sqrt{(0.03 * 5)^2} = 0.15 \text{ CFM}$$

$$U_d = U_{\dot{V}} = \sqrt{(0.05^2 + 0.15^2)} = 0.158 \text{ CFM} = \pm 7.46 * 10^{-5} \left(\frac{\text{m}^3}{\text{s}} \right) \text{ (95\% confidence level)}$$

OMEGA FL-2060

$$U_z = 0.5 * \text{resolution} = 0.5 * (0.1) = 0.05 \text{ CFM}$$

$$U_c = \sqrt{(0.03 * 10)^2} = 0.3 \text{ CFM}$$

$$U_d = U_{\dot{V}} = \sqrt{(0.05^2 + 0.3^2)} = 0.304 \text{ CFM} = \pm 14.4 * 10^{-5} \left(\frac{\text{m}^3}{\text{s}} \right) \text{ (95\% confidence level)}$$

Temperature Measurement

Thermocouples + 2700 Multimeter/Data Acquisition System:

$$U_z = 0.5 * \text{resolution} = 0.5 * (0.001) = 5 * 10^{-4} \text{°C}$$

$$U_c = 0.1 \text{°C}$$

$$U_d = U_T = \sqrt{(0.0005^2 + 0.1^2)} = \pm 0.1 \text{°C (95% confidence level)}$$

Length Measurement

$$U_z = 0.5 * \text{resolution} = 0.5 * (0.0254) = 0.0127 \text{ mm}$$

$$U_c = 0$$

$$U_d = U_z = U_L = U_H = U_W = \pm 1.27 * 10^{-5} \text{ m (95% confidence level)}$$

Error Propagation

Foam base area (A_b)

$$A_b = W * L$$

$$\frac{\partial A_b}{\partial W} = L \quad \& \quad \frac{\partial A_b}{\partial L} = W$$

$$U_{A_b} = \sqrt{\left(U_W * \frac{\partial A_b}{\partial W}\right)^2 + \left(U_L * \frac{\partial A_b}{\partial L}\right)^2} = \sqrt{(1.27 * 10^{-5} * L)^2 + (1.27 * 10^{-5} * W)^2}$$

$$U_{A_b} = 1.27 * 10^{-5} * \sqrt{L^2 + W^2}$$

Cross-sectional area of flow (A_c)

$$A_c = W * H$$

$$\frac{\partial A_c}{\partial W} = H \quad \& \quad \frac{\partial A_c}{\partial H} = W$$

$$U_{A_c} = \sqrt{\left(U_W * \frac{\partial A_c}{\partial W}\right)^2 + \left(U_H * \frac{\partial A_c}{\partial H}\right)^2} = \sqrt{(1.27 * 10^{-5} * H)^2 + (1.27 * 10^{-5} * W)^2}$$

$$U_{A_c} = 1.27 * 10^{-5} * \sqrt{H^2 + W^2}$$

Average inlet air velocity (U)

$$U = \frac{\dot{V}}{A_c} = \frac{\dot{V}}{W * H}$$

$$\frac{\partial U}{\partial \dot{V}} = \frac{1}{W * H} \quad \& \quad \frac{\partial U}{\partial A_c} = -\frac{\dot{V}}{(W * H)^2}$$

$$U_U = \sqrt{\left(U_{\dot{V}} * \frac{\partial U}{\partial \dot{V}}\right)^2 + \left(U_{A_c} * \frac{\partial U}{\partial A_c}\right)^2} = \sqrt{\left(\frac{U_{\dot{V}}}{W * H}\right)^2 + \left(\frac{U_{A_c} * \dot{V}}{(W * H)^2}\right)^2}$$

$$U_U = \frac{1}{W * H} \sqrt{U_{\dot{V}}^2 + \left(\frac{1.27 * 10^{-5} * \sqrt{H^2 + W^2} * \dot{V}}{W * H}\right)^2}$$

Heat transfer coefficient (HTC)

$$HTC = \frac{Q}{A_b(T_{fb} - T_{bi})}$$

$$\frac{\partial HTC}{\partial A_b} = -\frac{Q}{A_b^2(T_{fb} - T_{bi})} = -\frac{HTC}{A_b} \quad \& \quad \frac{\partial HTC}{\partial Q} = \frac{1}{A_b(T_{fb} - T_{bi})} = \frac{HTC}{Q}$$

$$\frac{\partial HTC}{\partial T_{bi}} = \frac{Q}{A_b(T_{fb} - T_{bi})^2} = \frac{HTC}{(T_{fb} - T_{bi})} \quad \& \quad \frac{\partial HTC}{\partial T_{fb}} = -\frac{Q}{A_b(T_{fb} - T_{bi})^2} = -\frac{HTC}{(T_{fb} - T_{bi})}$$

$$U_{HTC} = \sqrt{\left(U_Q * \frac{\partial HTC}{\partial Q}\right)^2 + \left(U_{A_b} * \frac{\partial HTC}{\partial A_b}\right)^2 + \left(U_{T_{fb}} * \frac{\partial HTC}{\partial T_{fb}}\right)^2 + \left(U_{T_{bi}} * \frac{\partial HTC}{\partial T_{bi}}\right)^2}$$

$$= \sqrt{\left(\left(\alpha * Q\right) * \frac{HTC}{Q}\right)^2 + \left(\left(1.27 * 10^{-5} * \sqrt{L^2 + W^2}\right) * \frac{HTC}{W * L}\right)^2 + \left(0.1 * \frac{HTC}{(T_{fb} - T_{bi})}\right)^2 + \left(0.1 * \frac{HTC}{(T_{fb} - T_{bi})}\right)^2}$$

$$U_U = HTC \sqrt{\alpha^2 + \left(\frac{1.27 * 10^{-5} * \sqrt{L^2 + W^2}}{W * L}\right)^2 + \frac{0.02}{(T_{fb} - T_{bi})^2}}$$

α is the Wattage tolerance in percent which is determined by the manufacturer 5 to -10%.

Measurements and uncertainties of experimental parameters are shown in the following table:

	T_{fb} (°C)	T_{bi} (°C)	T_{bo} (°C)	Δp (Pa)	\dot{V} (L/s)	U (m/s)	HTC (W/m ² .K)	U_{Tfb} (±%)	U_{Tbi} (±%)	U_{Tbo} (±%)	$U_{\Delta p}$ (±%)	$U_{\dot{V}}$ (±%)	U_U (±%)	U_{HTC} (±%)
F1(11.7x25.4)	69.7	22.8	62.7	58	0.5	0.9	446	0.1	0.4	0.2	42.9	4.9	4.9	6.3
	51.4	22.3	45.4	126	1.0	1.7	749	0.2	0.4	0.2	19.8	7.6	7.6	6.3
	43.5	22.0	37.4	245	1.5	2.5	1071	0.2	0.5	0.3	10.2	5.1	5.1	6.4
	39.5	21.9	33.7	400	2.0	3.3	1364	0.3	0.5	0.3	6.2	3.8	3.8	6.4
	36.6	21.6	31.2	630	2.5	4.2	1665	0.3	0.5	0.3	4.0	3.0	3.1	6.4
	34.8	21.6	29.6	995	2.8	4.8	1921	0.3	0.5	0.3	2.5	5.1	5.1	6.4
	32.8	21.5	27.9	1730	3.3	5.6	2425	0.3	0.5	0.4	1.4	4.4	4.4	6.4
	31.9	21.5	27.2	2330	3.8	6.4	2697	0.3	0.5	0.4	1.1	3.8	3.8	6.5
	31.1	21.5	26.5		4.2	7.2	3041	0.3	0.5	0.4		3.4	3.4	6.5
F2 (6.8x25.4)	71.8	22.6	67.8	54	0.2	0.7	271	0.1	0.4	0.1	46.1	10.3	10.3	6.3
	51.8	22.4	48.4	112	0.5	1.5	454	0.2	0.4	0.2	22.2	4.9	4.9	6.3
	42.0	22.1	39.6	211	0.8	2.3	668	0.2	0.5	0.3	11.8	3.2	3.2	6.4
	37.8	21.9	35.4	310	1.0	2.9	840	0.3	0.5	0.3	8.0	7.6	7.6	6.4
	34.9	21.8	32.6	440	1.2	3.6	1023	0.3	0.5	0.3	5.7	6.1	6.1	6.4
	33.0	21.7	30.8	633	1.5	4.3	1182	0.3	0.5	0.3	3.9	5.1	5.1	6.4
	31.2	21.7	29.2	877	1.7	5.0	1395	0.3	0.5	0.3	2.8	4.3	4.4	6.5
	29.9	21.5	27.9	1150	2.0	5.7	1593	0.3	0.5	0.4	2.2	3.8	3.8	6.5
	29.1	21.4	27.1	1440	2.2	6.5	1751	0.3	0.5	0.4	1.7	3.4	3.4	6.6
	28.3	21.4	26.3	1840	2.5	7.2	1929	0.4	0.5	0.4	1.4	3.0	3.1	6.6
F3 (4.4x25.4)	57.3	21.3	55.7	190	0.2	1.1	278	0.2	0.5	0.2	13.1	10.3	10.2	6.3
	41.2	21.1	40.4	530	0.5	2.3	496	0.2	0.5	0.2	4.7	4.9	4.9	6.4
	35.2	21.3	34.4	1115	0.8	3.5	723	0.3	0.5	0.3	2.2	3.2	3.2	6.4
	32.5	21.3	31.9	1700	1.0	4.5	896	0.3	0.5	0.3	1.5	7.6	7.5	6.5
	30.3	21.2	29.7	2640	1.2	5.6	1110	0.3	0.5	0.3	0.9	6.1	6.0	6.5
	28.5	21.1	28.0		1.5	6.8	1343	0.4	0.5	0.4		5.1	5.0	6.6
	27.4	21.0	26.9		1.7	7.9	1554	0.4	0.5	0.4		4.3	4.3	6.7
	26.6	20.8	26.0		2.0	9.0	1742	0.4	0.5	0.4		3.8	3.8	6.8
F4 (11.7x38.1)	67.0	22.3	57.4	52	0.5	0.9	326	0.1	0.4	0.2	47.9	4.9	4.9	6.3
	49.2	22.1	42.0	120	1.0	1.7	576	0.2	0.5	0.2	20.8	7.6	7.6	6.3
	41.1	22.0	35.2	243	1.5	2.5	877	0.2	0.5	0.3	10.2	5.1	5.1	6.4
	37.3	21.8	31.7	400	2.0	3.3	1144	0.3	0.5	0.3	6.2	3.8	3.8	6.4
	34.9	21.7	29.5	590	2.5	4.2	1409	0.3	0.5	0.3	4.2	3.0	3.1	6.4
	33.0	21.6	27.8	940	2.8	4.8	1748	0.3	0.5	0.4	2.6	5.1	5.1	6.4
	31.1	21.4	26.2	1540	3.3	5.6	2223	0.3	0.5	0.4	1.6	4.4	4.4	6.5
	30.1	21.4	25.5	2170	3.8	6.4	2596	0.3	0.5	0.4	1.1	3.8	3.8	6.5
	29.4	21.4	24.9		4.2	7.2	2998	0.3	0.5	0.4		3.4	3.4	6.6

F5 (6.8x38.1)	67.9	22.4	65.4	47	0.2	0.7	196	0.1	0.4	0.2	53.0	10.3	10.3	6.3
	50.1	22.3	48.9	103	0.5	1.5	320	0.2	0.4	0.2	24.2	4.9	4.9	6.3
	40.7	22.0	39.9	188	0.8	2.3	477	0.2	0.5	0.3	13.2	3.2	3.2	6.4
	36.2	22.0	35.7	278	1.0	2.9	623	0.3	0.5	0.3	9.0	7.6	7.6	6.4
	33.5	21.8	33.0	411	1.2	3.6	764	0.3	0.5	0.3	6.1	6.1	6.1	6.4
	31.4	21.7	31.0	586	1.5	4.3	920	0.3	0.5	0.3	4.2	5.1	5.1	6.5
	29.8	21.6	29.4	800	1.7	5.0	1087	0.3	0.5	0.3	3.1	4.3	4.4	6.6
	28.7	21.5	28.2	1040	2.0	5.7	1245	0.3	0.5	0.4	2.4	3.8	3.8	6.6
	27.8	21.5	27.4	1330	2.2	6.5	1400	0.4	0.5	0.4	1.9	3.4	3.4	6.7
	27.1	21.4	26.7	1650	2.5	7.2	1546	0.4	0.5	0.4	1.5	3.0	3.1	6.8
F6 (4.4x38.1)	54.5	21.3	52.9	145	0.2	1.1	201	0.2	0.5	0.2	17.2	10.3	10.2	6.3
	44.3	21.3	43.7	270	0.5	2.3	290	0.2	0.5	0.2	9.2	4.9	4.9	6.4
	34.3	21.3	34.1	750	0.8	3.5	510	0.3	0.5	0.3	3.3	3.2	3.2	6.4
	31.6	21.2	31.4	1045	1.0	4.5	642	0.3	0.5	0.3	2.4	7.6	7.5	6.5
	29.3	21.1	29.3	1655	1.2	5.6	808	0.3	0.5	0.3	1.5	6.1	6.0	6.6
	27.8	21.1	27.8	2350	1.5	6.8	987	0.4	0.5	0.4	1.1	5.1	5.0	6.7
	26.8	21.0	26.7		1.7	7.9	1156	0.4	0.5	0.4		4.3	4.3	6.8
	25.9	20.9	25.7		2.0	9.0	1353	0.4	0.5	0.4		3.8	3.8	6.9
F7 (11.7x52.1)	61.7	22.7	52.4	40	0.5	0.9	258	0.2	0.4	0.2	62.3	4.9	4.9	6.3
	45.8	22.3	40.3	90	1.0	1.7	439	0.2	0.4	0.2	27.7	7.6	7.6	6.4
	38.8	22.0	33.8	180	1.5	2.5	634	0.3	0.5	0.3	13.8	5.1	5.1	6.4
	35.2	21.8	30.5	306	2.0	3.3	812	0.3	0.5	0.3	8.1	3.8	3.8	6.4
	33.0	21.6	28.4	475	2.5	4.2	982	0.3	0.5	0.4	5.2	3.0	3.1	6.4
	31.0	21.5	26.7	750	2.8	4.8	1200	0.3	0.5	0.4	3.3	5.1	5.1	6.5
	29.4	21.4	25.3	1340	3.3	5.6	1487	0.3	0.5	0.4	1.9	4.4	4.4	6.6
	28.6	21.5	24.7	1850	3.8	6.4	1687	0.3	0.5	0.4	1.3	3.8	3.8	6.6
	27.9	21.5	24.1	2600	4.2	7.2	1934	0.4	0.5	0.4	1.0	3.4	3.4	6.7
F8 (6.8x52.1)	66.8	22.5	58.4	40	0.2	0.7	147	0.1	0.4	0.2	62.3	10.3	10.3	6.3
	49.5	22.3	45.2	80	0.5	1.5	239	0.2	0.4	0.2	31.1	4.9	4.9	6.3
	40.5	22.2	38.0	145	0.8	2.3	355	0.2	0.5	0.3	17.2	3.2	3.2	6.4
	36.5	22.0	34.3	226	1.0	2.9	449	0.3	0.5	0.3	11.0	7.6	7.6	6.4
	33.8	21.9	31.8	333	1.2	3.6	549	0.3	0.5	0.3	7.5	6.1	6.1	6.4
	31.7	21.8	29.9	480	1.5	4.3	654	0.3	0.5	0.3	5.2	5.1	5.1	6.5
	30.2	21.6	28.5	660	1.7	5.0	761	0.3	0.5	0.4	3.8	4.3	4.4	6.5
	29.0	21.5	27.4	855	2.0	5.7	864	0.3	0.5	0.4	2.9	3.8	3.8	6.6
	28.1	21.4	26.5	1111	2.2	6.5	975	0.4	0.5	0.4	2.2	3.4	3.4	6.7
	27.4	21.3	25.9	1380	2.5	7.2	1069	0.4	0.5	0.4	1.8	3.0	3.1	6.7

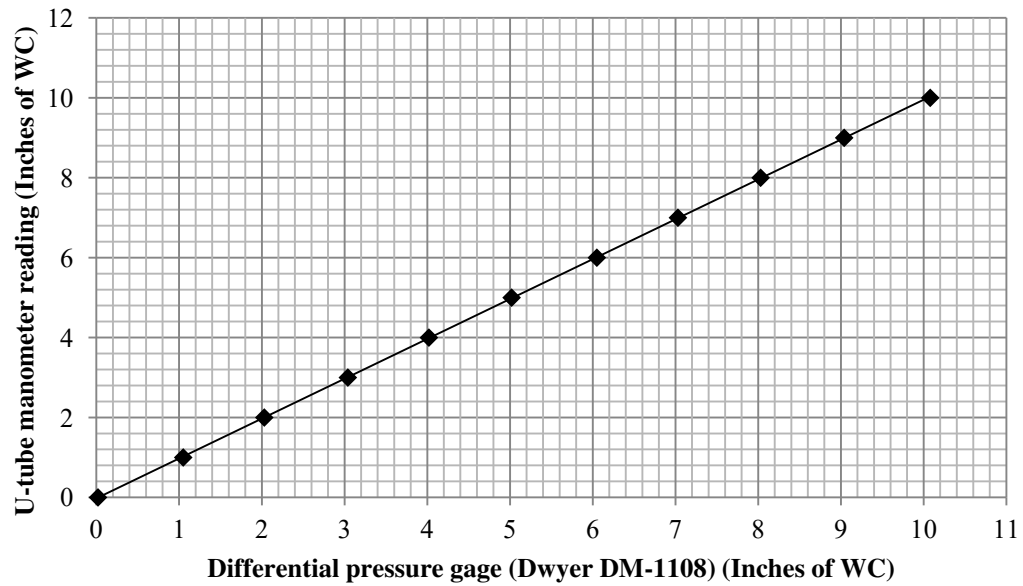
F9 (4.4x52.1)	53.3	21.9	49.0	95	0.2	1.1	155	0.2	0.5	0.2	26.2	10.3	10.2	6.3
	40.9	21.8	39.4	248	0.5	2.3	256	0.2	0.5	0.3	10.0	4.9	4.9	6.4
	34.8	21.9	34.1	510	0.8	3.5	377	0.3	0.5	0.3	4.9	3.2	3.2	6.4
	32.1	21.7	31.5	780	1.0	4.5	472	0.3	0.5	0.3	3.2	7.6	7.5	6.5
	29.7	21.6	29.4	1230	1.2	5.6	602	0.3	0.5	0.3	2.0	6.1	6.0	6.6
	28.1	21.4	27.8	1720	1.5	6.8	733	0.4	0.5	0.4	1.4	5.1	5.0	6.7
	26.9	21.3	26.6	2400	1.7	7.9	877	0.4	0.5	0.4	1.0	4.3	4.3	6.8
	26.1	21.2	25.8		2.0	9.0	1002	0.4	0.5	0.4		3.8	3.8	7.0

APPENDIX B: CALIBRATION OF MEASUREMENT INSTRUMENTS

Differential Pressure Gage

The differential pressure gage (Dwyer DM-1108) is calibrated by a U-tube manometer.

Manometer Reading (Inches of WC)	DWYER (DM-1108) (Inches of WC)
0	0.02
1	1.05
2	2.03
3	3.04
4	4.02
5	5.02
6	6.05
7	7.03
8	8.03
9	9.04
10	10.08



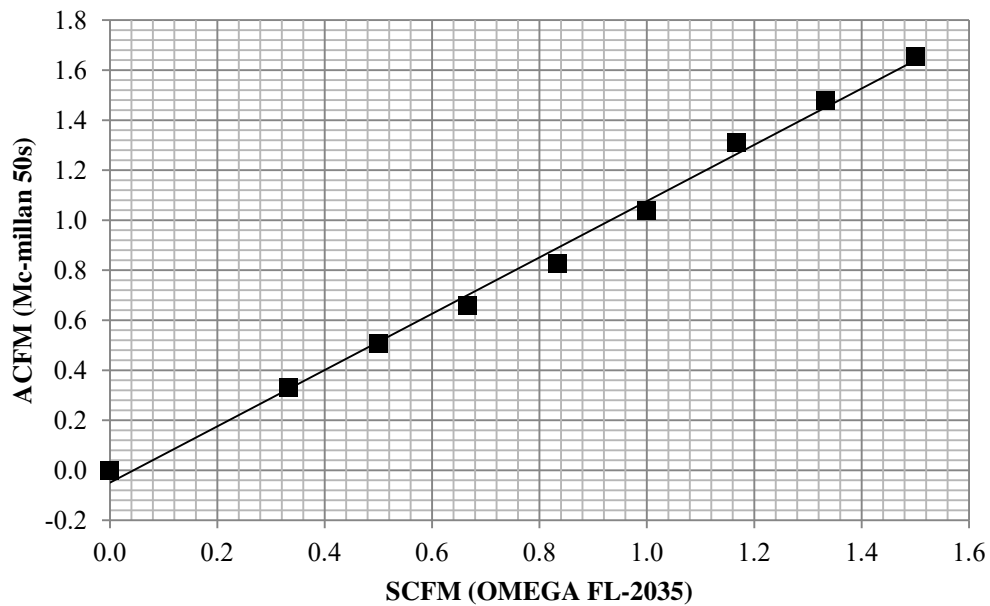
$$p_{\text{actual}} = 0.9975 * p_{\text{measured}} - 0.0248$$

Rotameters

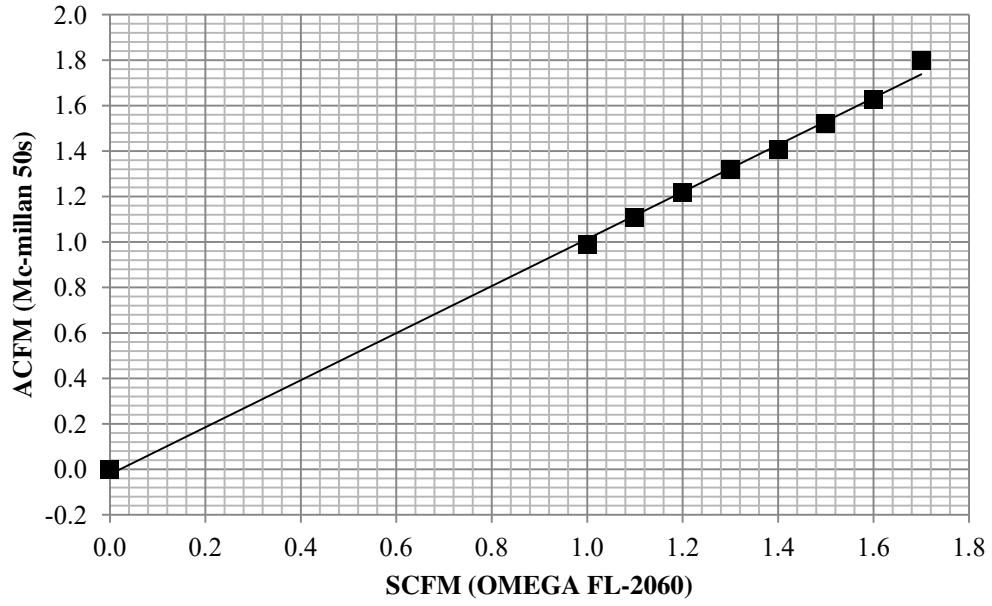
Rotameters are calibrated using McMillan mass flow sensor (model 50s, 0-50 l/min).

FL-2035	McMillan 50s		FL-2060	McMillan 50s		FL-2061	McMillan 50s	
SCFM	Volt	ACFM	SCFM	Volt	ACFM	SCFM	Volt	ACFM
0.000	-0.002	-0.001	0.000	-0.002	-0.001	0.000	-0.002	-0.001
0.333	0.920	0.333	1.000	2.733	0.988	1.000	2.535	0.917
0.500	1.400	0.506	1.100	3.060	1.106	1.250	3.326	1.202
0.667	1.820	0.658	1.200	3.370	1.218	1.500	4.030	1.457
0.833	2.290	0.828	1.300	3.650	1.320	1.750	4.930	1.782
1.000	2.870	1.038	1.400	3.890	1.406			
1.167	3.630	1.312	1.500	4.210	1.522			
1.333	4.090	1.479	1.600	4.500	1.627			
1.500	4.580	1.656	1.700	4.970	1.797			

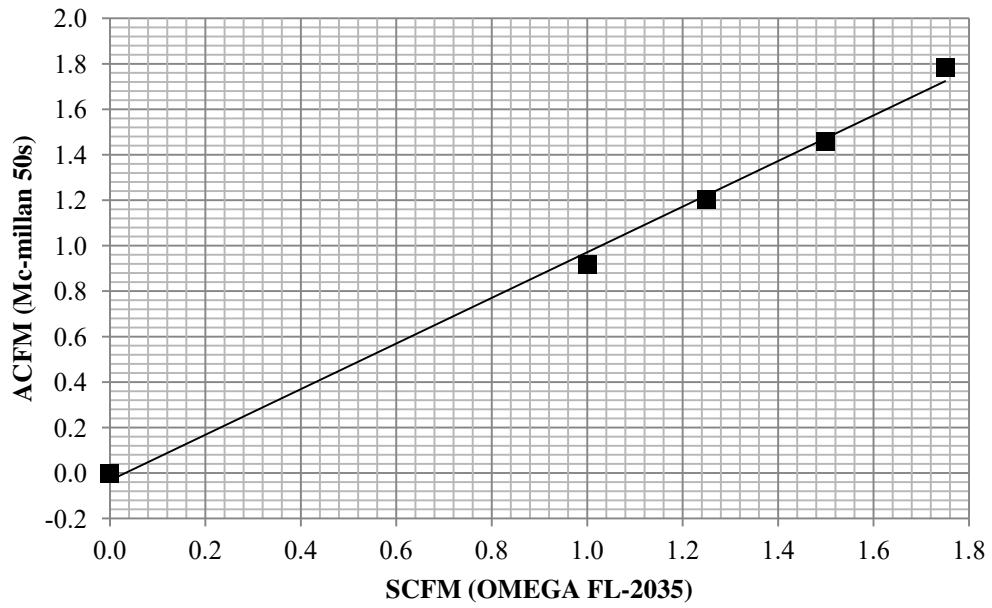
OMEGA FL-2035



OMEGA FL-2060



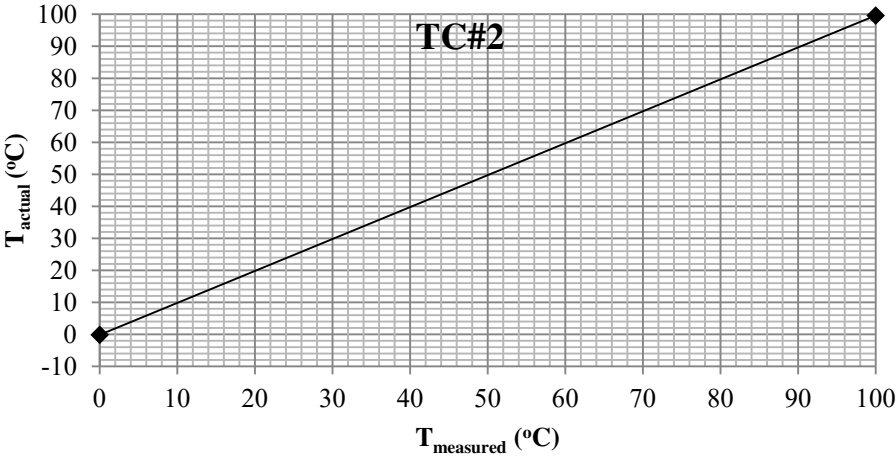
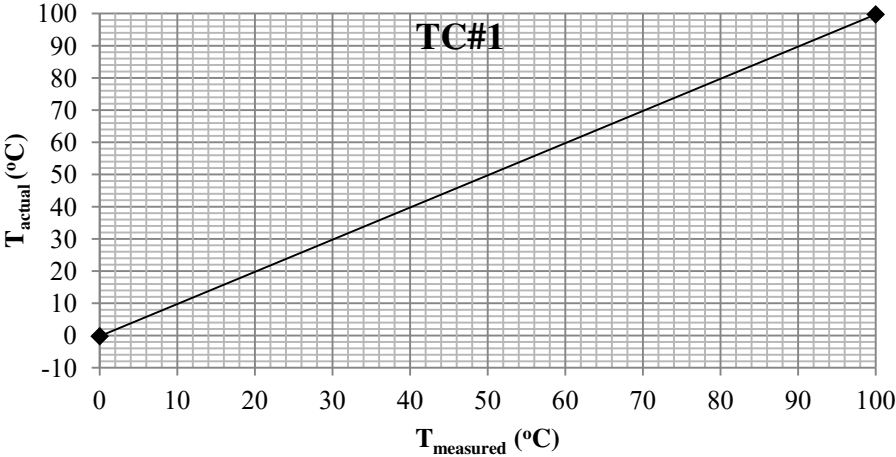
OMEGA FL-2061

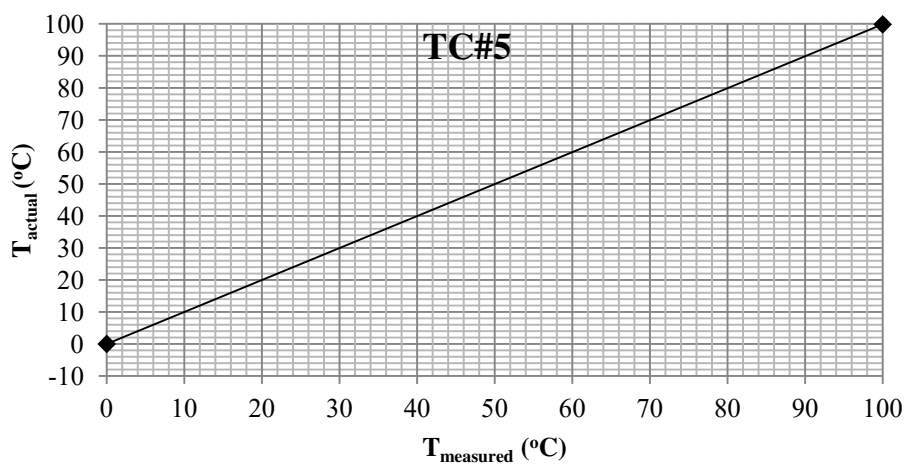
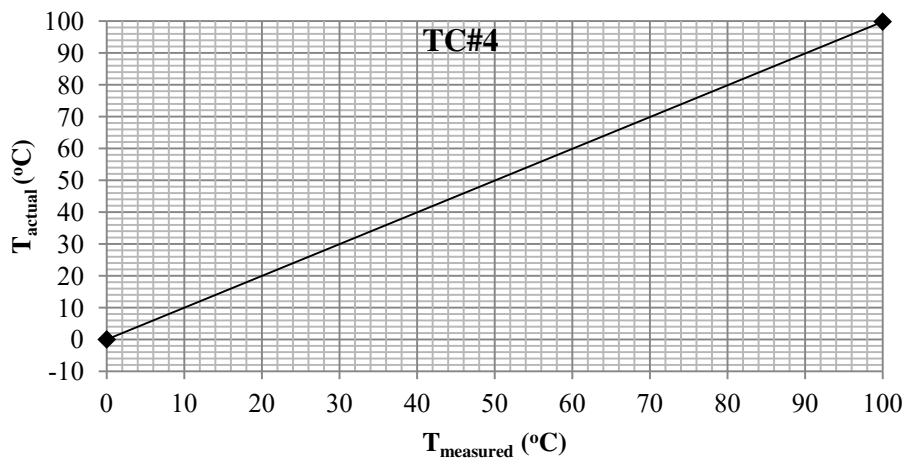
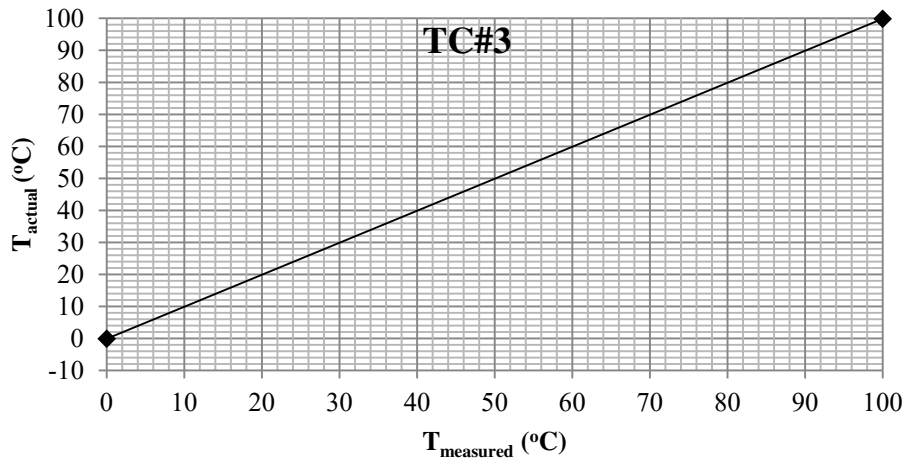


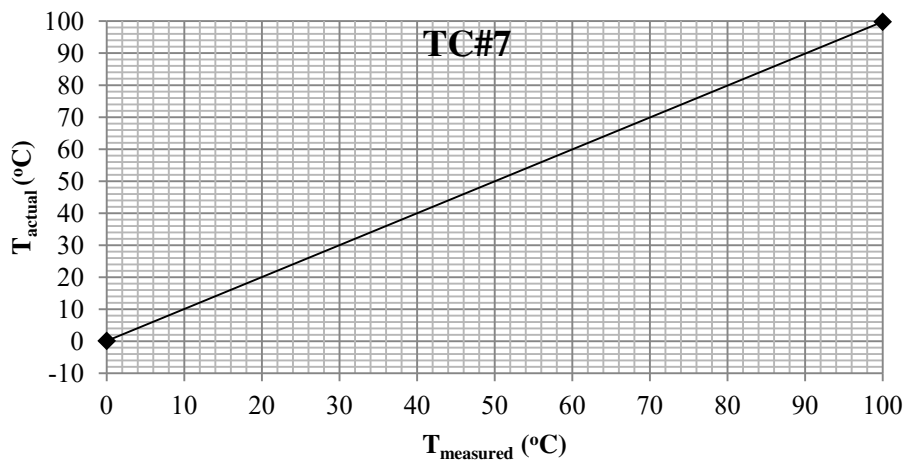
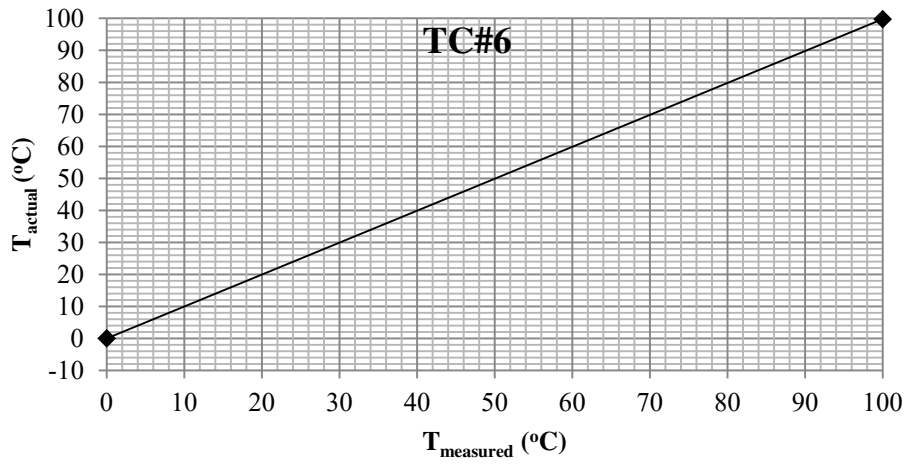
OMEGA FL-2035	$ACFM = 1.1257 * SCFM - 0.0496$
OMEGA FL-2060	$ACFM = 1.0351 * SCFM - 0.0217$
OMEGA FL-2061	$ACFM = 1.0032 * SCFM - 0.032$

Thermocouples

Thermocouples are calibrated in boiling water and ice/water bath.







TC#1	$T_{\text{actual}} = 0.9995 * T_{\text{measured}} - 0.2267$
TC#2	$T_{\text{actual}} = 0.9973 * T_{\text{measured}} - 0.12$
TC#3	$T_{\text{actual}} = 0.9994 * T_{\text{measured}} - 0.09$
TC#4	$T_{\text{actual}} = 0.9984 * T_{\text{measured}} - 0.0033$
TC#5	$T_{\text{actual}} = 0.9984 * T_{\text{measured}} + 0.0233$
TC#6	$T_{\text{actual}} = 0.9972 * T_{\text{measured}} + 0.0333$
TC#7	$T_{\text{actual}} = 0.9967 * T_{\text{measured}} + 0.13$

APPENDIX C: CONDENSER DESIGN

Governing Equation:

$$Q = \dot{m}_a \cdot c_p \cdot (T_{bo} - T_{bi}) = \dot{m}_R \cdot (\Delta h_{\text{superheat}} + h_{fg} + \Delta h_{\text{subcooling}}) = A_O \cdot U_O \cdot (T_{\text{sat}} - T_{bi}) \\ = A_c \cdot h_{\text{condensation}} \cdot (T_{\text{sat}} - T_{fb}) = A_O \cdot \text{HTC} \cdot (T_{fb} - T_{bi})$$

26

where;

\dot{m}_a is the mass flow rate of the air.

\dot{m}_R is the mass flow rate of the refrigerant.

A_O is the total outside surface area of the condenser.

A_f is the refrigerant flow area.

A_c is the refrigerant flow surface area of the condenser.

Δh_{fg} is the latent heat of the refrigerant.

$\Delta h_{\text{superheat}}$ is specific enthalpy drop of the refrigerant gas.

$\Delta h_{\text{subcooled}}$ is specific enthalpy drop of the refrigerant liquid.

T_{bi} is the air inlet temperature (71°C).

T_{bo} is the air outlet temperature.

T_{fb} is the surface temperature of the condenser.

T_{sat} is the condensation temperature of the refrigerant (80°C).

$h_{\text{condensation}}$ is the average heat transfer coefficient of condensation.

HTC is the average heat transfer coefficient for the air side.

U_O is the overall heat transfer coefficient based on the total outside surface area of the condenser (A_O) and $(T_{fb} - T_{ai})$.

L_1 is the condensation length.

L_2 is the superheat length.

L_3 is the subcooling length.

Case (1): Superheat, Condensation and Subcooling

Allowing the refrigerant gas to enter the condenser at 120°C, $\Delta h_{\text{superheat}} = 454.9 - 410.7 = 44.2 \left(\frac{\text{kJ}}{\text{kg}}\right)$.

$$Q = 105 = m_R \cdot (h_{fg} + \Delta h_{\text{superheat}} + \Delta h_{\text{subcooling}})$$

$$p_{\text{sat}} = 12.5 \text{ bar} \approx 184 \text{ Psi} \quad \& \quad T_{\text{sat}} = 80^\circ\text{C}$$

$$h_g = 410.7 \left(\frac{\text{kJ}}{\text{kg}}\right) \quad \& \quad h_l = 305.4 \left(\frac{\text{kJ}}{\text{kg}}\right)$$

Therefore

$$\therefore 105 = m_R \cdot [(410.7 - 305.4) + 44.2 + 3.8] \cdot 10^3 \rightarrow m_R = 0.68 \left(\frac{\text{g}}{\text{s}}\right)$$

Assuming the total number of minichannels (n^*) is proportional to the width of the condenser and the old condenser has 31 minichannels:

$$n_1^* = n_{1.25}^* \cdot \left(\frac{1}{1.25}\right) = 31 \cdot \left(\frac{1}{1.25}\right) = 25$$

$$\text{The refrigerant flow area } (A_f) = 25 * \frac{\pi}{4} * (0.024 * 0.0254)^2 = 7.3 * 10^{-6} \text{ m}^2$$

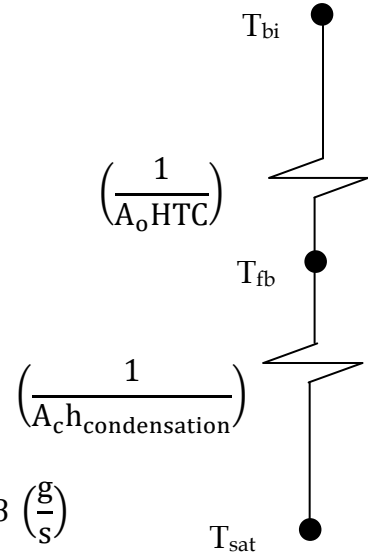
Condensation region:

$$\begin{aligned} Q_{\text{condensation}} &= m_a \cdot c_p \cdot (T_{bo} - T_{bi}) = m_R \cdot h_{fg} \\ &= 0.68 * 10^{-3} \cdot (410.7 - 305.4) * 10^3 = 71.6 \text{ W} \\ &= A_o \cdot U_o \cdot (T_{\text{sat}} - T_{bi}) = A_c \cdot h_{\text{condensation}} \cdot (T_{\text{sat}} - T_{fb}) \\ &= A_o \cdot \text{HTC} \cdot (T_{fb} - T_{bi}) \end{aligned}$$

$$\text{The specific volume of the gas is } (v_g) = \frac{1}{89.33} = 0.0112 \text{ (m}^3/\text{kg)} \rightarrow \text{(NIST)}$$

$$\text{The dynamic viscosity of the gas is } (\mu_g) = 1.3282 * 10^{-5} \text{ (Pa} \cdot \text{s)} \rightarrow \text{(NIST)}$$

$$\text{Therefore during the condensation, the gas side velocity } (v_g) = \frac{m_R \cdot v_g}{A_f} = 1.04 \text{ (m/s)}$$



$$Re_g = \left(\frac{v_g \cdot d}{\nu_g \cdot \mu_g} \right) = 4263 < 35,000$$

$$h_{\text{condensation}} = 0.555 \left[\frac{g \cdot \rho_l \cdot (\rho_l - \rho_g) \cdot k_l^3 \cdot h'_{fg}}{\mu_l \cdot (T_{\text{sat}} - T_{\text{fb}}) \cdot d} \right]^{0.25} \quad [33]$$

$$c_{pl}@80^\circ\text{C} = 1.5 \left(\frac{\text{kJ}}{\text{kg} \cdot \text{K}} \right) \rightarrow \text{(NIST)}$$

$$\rho_l@80^\circ\text{C} = 1138 \left(\frac{\text{kg}}{\text{m}^3} \right) \rightarrow \text{(NIST)}$$

$$k_l@80^\circ\text{C} = 0.0573 \left(\frac{\text{W}}{\text{m} \cdot \text{K}} \right) \rightarrow \text{(NIST)}$$

$$\mu_l@80^\circ\text{C} = 0.000143 \left(\frac{\text{N} \cdot \text{s}}{\text{m}^2} \right) \rightarrow \text{(NIST)}$$

Assume that the condenser surface temperature $\approx 79^\circ\text{C}$ and we will justify this assumption after calculating the minichannel length.

$$h'_{fg} = h_{fg} + \frac{3}{8} \cdot c_{pl} \cdot (T_{\text{sat}} - T_{\text{fb}}) = 105.9 \frac{\text{kJ}}{\text{kg}} \quad [33]$$

$$\therefore h_{\text{condensation}} = 3992 \left(\frac{\text{W}}{\text{m}^2 \cdot \text{K}} \right)$$

The actual air velocity can be determined from the foam-fan curve using trial and error. First assume the air flow velocity. The corresponding pressure drop and HTC can be obtained from [Figures 5-8](#). In the end after calculating the width of the condenser (W^*), the air flow velocity can be check from the fan-foam coupling graph. These graphs are illustrated in [Figure 24](#).

$$v_{\text{actual}} = 4 \left(\frac{\text{m}}{\text{s}} \right) \text{ @ pressure drop of } 560(\text{Pa})$$

The corresponding air-side HTC for the new area will be:

$$HTC = 1120 \left(\frac{\text{W}}{\text{m}^2 \cdot \text{K}} \right)$$

$$A_o = 1 * 0.0254 * L_1 = 0.0254L_1 \text{ m}^2$$

$$A_c = \pi * (0.024 * 0.0254) * L_1 * 25 = 0.048L_1 \text{ m}^2$$

$$\begin{aligned} \therefore A_o U_o &= \left[\frac{1}{0.0254L_1 * 1120} + \frac{1}{0.048L_1 * 3992} \right]^{-1} \\ &= \left[\frac{1}{28.4L_1} + \frac{1}{191.6L_1} \right]^{-1} \end{aligned}$$

where L_1 is the condensation length.

$$\therefore A_o U_o = 24.8 * L_1 \left(\frac{W}{K} \right)$$

$$Q = A_o \cdot U_o \cdot (T_{sat} - T_{bi})$$

$$\therefore 71.6 = 24.8 * L_1 * 9$$

$$\therefore L_1 = L_{(\text{one heated surface})} = 0.32 \text{ m}$$

Note: $L_{(\text{one heated surface})}$ is the length of the refrigerant tubes as if it is heated from one side

Check for the surface temperature of the condenser:

$$T_{fb} = 80 - \left(\frac{Q}{A_c h_{\text{condensation}}} \right) = 80 - \left(\frac{71.6}{0.048 * 0.32 * 3992} \right) \approx 79^\circ\text{C}$$

Superheat region:

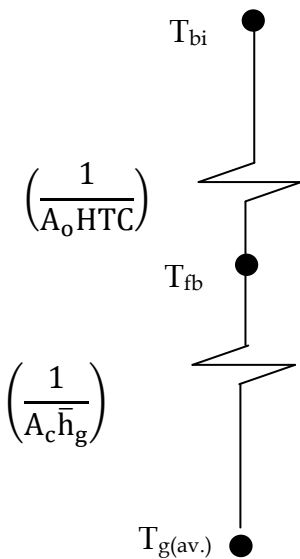
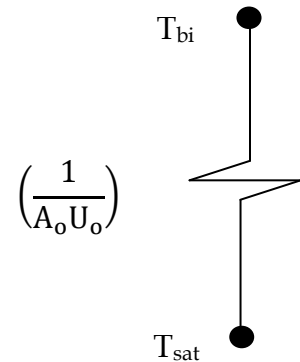
$$c_{pG} @ T_m = 1.1322 \left(\frac{\text{kJ}}{\text{kg} \cdot \text{K}} \right)$$

$$\rho_G @ T_m = 83.85 \left(\frac{\text{kg}}{\text{m}^3} \right)$$

$$k_G @ T_m = 0.02 \left(\frac{\text{W}}{\text{m} \cdot \text{K}} \right)$$

$$\mu_G @ T_m = 1.36 * 10^{-5} \left(\frac{\text{N} \cdot \text{s}}{\text{m}^2} \right)$$

$$Pr_G = \left(\frac{c_{pG} \cdot \mu_G}{k_G} \right) = \left(\frac{1132.2 * 1.36 * 10^{-5}}{0.02} \right) = 0.77$$



$$v_G = \frac{\dot{m}_R \cdot v_G}{A_f} = \left(\frac{0.68 * 10^{-3}}{83.85 * 7.3 * 10^{-6}} \right) = 1.11 \text{ (m/s)}$$

$$Re_G = \left(\frac{\rho_G \cdot v_G \cdot d}{\mu_G} \right) = \left(\frac{83.85 * 1.11 * 0.024 * 0.0254}{1.36 * 10^{-5}} \right) = 4172$$

Absolute roughness for aluminum (ϵ_R) = $1.5 * 10^{-6}$ m

Relative roughness for aluminum (ϵ_R/d) = 0.0025 m

$f = 0.042$

$$Nu = \left[\frac{\left(\frac{f}{8}\right) (Re_g - 1000) Pr_G}{1 + \left(12.7 \left(\frac{f}{8}\right)^{0.5} \left(Pr_G^{\frac{2}{3}} - 1\right)\right)} \right]$$

Since (L/d) is greater than 60 therefore:

$$Nu = \bar{Nu} = \left(\frac{\bar{h}_G \cdot d}{k_G} \right) = \left[\frac{\frac{0.042}{8} * (4172 - 1000) * 0.77}{1 + \left(12.7 * \left(\frac{0.042}{8}\right)^{0.5} \left(0.77^{\frac{2}{3}} - 1\right)\right)} \right] = 15$$

$$\therefore \bar{h}_G = 493 \left(\frac{W}{m^2 \cdot K} \right)$$

where \bar{h}_g is the heat transfer coefficient of the refrigerant superheated gas

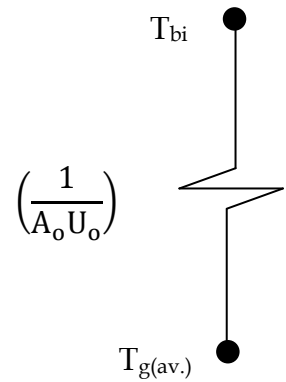
$$A_0 U_0 = \left[\frac{1}{A_0 HTC} + \frac{1}{A_c \bar{h}_G} \right]^{-1}$$

$$\therefore A_0 U_0 = \left[\frac{1}{0.0254 L_2 * 1120} + \frac{1}{0.048 L_2 * 493} \right]^{-1}$$

where L_2 is the superheat length.

$$\therefore A_0 U_0 = [12.9 L_2] \text{ W/K}$$

$$Q_{\text{superheat}} = A_0 \cdot U_0 \cdot (T_{G(\text{av.})} - T_{\text{bi}}) = \dot{m}_R \cdot \Delta h_{\text{superheat}}$$



$$Q_{\text{superheat}} = m_{\text{R}} \cdot \Delta h_{\text{superheat}} = (0.68 * 10^{-3}) * (44.2 * 10^3)$$

$$\therefore 30.1 = [12.9L_2] * 29$$

$$\therefore L_2 = L_{(\text{one heated surface})} = 0.08 \text{ m}$$

Subcooling region:

$$c_{\text{PL}} @ T_{\text{m}} = 1.46 \left(\frac{\text{kJ}}{\text{kg} \cdot \text{K}} \right)$$

$$\rho_{\text{L}} @ T_{\text{m}} = 1160 \left(\frac{\text{kg}}{\text{m}^3} \right)$$

$$k_{\text{L}} @ T_{\text{m}} = 0.0584 \left(\frac{\text{W}}{\text{m} \cdot \text{K}} \right)$$

$$\mu_{\text{L}} @ T_{\text{m}} = 1.5 * 10^{-4} \left(\frac{\text{N} \cdot \text{s}}{\text{m}^2} \right)$$

$$\text{Pr}_{\text{L}} = \left(\frac{c_{\text{PL}} \cdot \mu_{\text{L}}}{k_{\text{L}}} \right) = \left(\frac{1460 * 1.5 * 10^{-4}}{0.0584} \right) = 3.75$$

$$v_{\text{L}} = \frac{m_{\text{R}} \cdot v_{\text{L}}}{A_{\text{f}}} = \left(\frac{0.68 * 10^{-3}}{1160 * 7.3 * 10^{-6}} \right) = 0.08 \text{ (m/s)}$$

$$\text{Re}_{\text{L}} = \left(\frac{\rho_{\text{L}} \cdot v_{\text{L}} \cdot d}{\mu_{\text{L}}} \right) = \left(\frac{1160 * 0.08 * 0.024 * 0.0254}{1.5 * 10^{-4}} \right) = 377$$

$$\therefore \overline{\text{Nu}} = \left(\frac{\overline{h}_{\text{L}} \cdot d}{k_{\text{L}}} \right) = 4.36$$

$$\therefore \overline{h}_{\text{L}} = 417.7 \left(\frac{\text{W}}{\text{m}^2 \cdot \text{K}} \right)$$

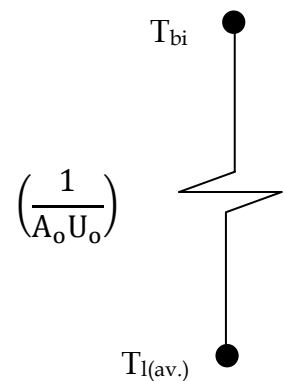
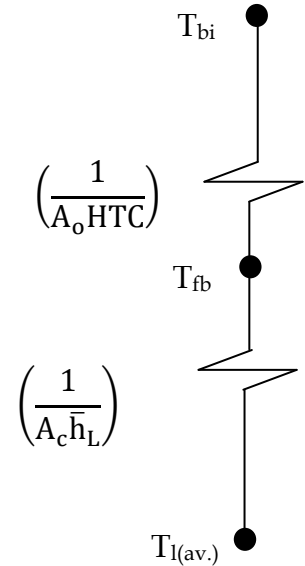
where \overline{h}_{L} is the heat transfer coefficient of the refrigerant subcooled liquid

$$A_{\text{O}}U_{\text{O}} = \left[\frac{1}{A_{\text{O}}\text{HTC}} + \frac{1}{A_{\text{c}}\overline{h}_{\text{L}}} \right]^{-1}$$

$$\therefore A_{\text{O}}U_{\text{O}} = \left[\frac{1}{0.0254L_3 * 1120} + \frac{1}{0.048L_3 * 417.7} \right]^{-1}$$

where L_3 is the subcooling length.

$$\therefore A_{\text{O}}U_{\text{O}} = [11.7L_3] \text{ W/K}$$



$$Q = A_0 \cdot U_0 \cdot (T_{L(av.)} - T_{bi}) = 105 - 71.6 - 30.1 = 3.3$$

$$\therefore 3.3 = [11.7L_3] * 7$$

$$\therefore L_3 = L_{(one\ heated\ surface)} = 0.04\ m$$

The total length of single surface condenser is $L_1+L_2+L_3 = 0.32+0.08+0.04=0.44\ m$

Since we are restricted to condenser height of 6.1 cm, with the fact that is the new condenser have four refrigerant tube passes for foam height of 6.8 mm then:

$$L_{(double\ surfaces)} = L_{condenser} = \frac{L_{(one\ heated\ surface)}}{2(N-1)} = \frac{L_{(one\ heated\ surface)}}{6} = 0.073m = 2.9"$$

where N is the number of refrigerant tube passes.

Outlet air temperature (T_{bo}):

Since the foam base thickness ($t_{foam} = 2mm$) and the refrigerant tube thickness ($t_{tube} = 2mm$) are contributing in the total air flow area then the air mass flow rate is calculated as follows:

$$m_a = A_{flow} \cdot \rho \cdot v = \left(\left(2.4 - ((N * t_{tube}) + (2(N-1)t_{foam})) \right) \cdot L_{double\ surface} \right) \cdot \rho \cdot v$$

where,

N is the number of refrigerant tubes.

t_{tube} is the condenser tube thickness.

t_{foam} is the foam base thickness.

$$Q = 105 = m_a \cdot c_p \cdot (T_{bo} - T_{bi})$$

$$105 = \left(\left((2.4 - ((4 * 0.079) + (2 * 3 * 0.079))) * 2.9 \right) * 0.0254^2 \right) * 1 * 4 * 1005 * (T_{bo} - 71)$$

$$T_{bo} = 79.7^\circ\text{C}$$

$$\therefore W^* = L_{\text{double surface}} = L_{\text{condenser}} = 2.9''$$

Case (2): Superheat and Condensation

$$Q = 105 = m_R \cdot (h_{fg} + \Delta h_{\text{superheat}})$$

$$\therefore 105 = m_R \cdot [(410.7 - 305.4) + 44.2] \cdot 10^3 \rightarrow m_R = 0.7 \left(\frac{\text{g}}{\text{s}} \right)$$

Condensation region:

$$\begin{aligned} Q_{\text{condensation}} &= m_a \cdot c_p \cdot (T_{bo} - T_{bi}) = m_R \cdot h_{fg} \\ &= 0.7 * 10^{-3} \cdot (410.7 - 305.4) * 10^3 = 73.7 \text{ W} \\ &= A_O \cdot U_O \cdot (T_{\text{sat}} - T_{bi}) \\ &= A_C \cdot h_{\text{condensation}} \cdot (T_{\text{sat}} - T_{fb}) \\ &= A_O \cdot \text{HTC} \cdot (T_{fb} - T_{bi}) \end{aligned}$$

$$\text{The specific volume of the gas is } (v_g) = \frac{1}{89.33} = 0.0112 \text{ (m}^3/\text{kg)} \rightarrow \text{(NIST)}$$

$$\text{The dynamic viscosity of the gas is } (\mu_g) = 1.3282 * 10^{-5} \text{ (Pa. s)} \rightarrow \text{(NIST)}$$

$$\text{Therefore during the condensation, the gas side velocity } (v_g) = \frac{m_R \cdot v_g}{A_f} = 1.07 \text{ (m/s)}$$

$$\text{Re}_g = \left(\frac{v_g \cdot d}{v_g \cdot \mu_g} \right) = 4387 < 35,000$$

$$h_{\text{condensation}} = 0.555 \left[\frac{g \cdot \rho_l \cdot (\rho_l - \rho_g) \cdot k_l^3 \cdot h'_{fg}}{\mu_l \cdot (T_{\text{sat}} - T_{fb}) \cdot d} \right]^{0.25}$$

$$c_{p_l} @ 80^\circ\text{C} = 1.5 \left(\frac{\text{kJ}}{\text{kg} \cdot \text{K}} \right) \rightarrow \text{(NIST)}$$

$$\rho_l @ 80^\circ\text{C} = 1138 \left(\frac{\text{kg}}{\text{m}^3} \right) \rightarrow \text{(NIST)}$$

$$k_l @ 80^\circ\text{C} = 0.0573 \left(\frac{\text{W}}{\text{m} \cdot \text{K}} \right) \rightarrow \text{(NIST)}$$

$$\mu_l @ 80^\circ\text{C} = 0.000143 \left(\frac{\text{N} \cdot \text{s}}{\text{m}^2} \right) \rightarrow \text{(NIST)}$$

assume that the condenser surface temperature $\approx 79^\circ\text{C}$ and we will justify this assumption after calculating the minichannel length.

$$h'_{fg} = h_{fg} + \frac{3}{8} \cdot c_{pl} \cdot (T_{\text{sat}} - T_{\text{fb}}) = 105.9 \frac{\text{kJ}}{\text{kg}}$$

$$\therefore h_{\text{condensation}} = 3992 \left(\frac{\text{W}}{\text{m}^2 \cdot \text{K}} \right)$$

The actual air velocity can be determined from the foam-fan curve using trial and error:

$$v_{\text{actual}} = 4 \left(\frac{\text{m}}{\text{s}} \right) \text{ @ pressure drop of } 560(\text{Pa})$$

The corresponding air-side HTC for the new area will be:

$$\text{HTC} = 1120 \left(\frac{\text{W}}{\text{m}^2 \cdot \text{K}} \right)$$

$$A_o = 1 * 0.0254 * L_1 = 0.0254L \text{ m}^2$$

$$A_c = \pi * (0.024 * 0.0254) * L_1 * 25 = 0.048L \text{ m}^2$$

$$\begin{aligned} \therefore A_o U_o &= \left[\frac{1}{0.0254L_1 * 1120} + \frac{1}{0.048L_1 * 3992} \right]^{-1} \\ &= \left[\frac{1}{28.4L_1} + \frac{1}{191.6L_1} \right]^{-1} \end{aligned}$$

$$\therefore A_o U_o = 24.8 * L_1 \left(\frac{\text{W}}{\text{K}} \right)$$

$$Q = A_o \cdot U_o \cdot (T_{\text{sat}} - T_{\text{bi}})$$

$$\therefore 73.7 = 24.8 * L_1 * 9$$

$$\therefore L_1 = L_{(\text{one heated surface})} = 0.33 \text{ m}$$

Check for the surface temperature of the condenser:

$$T_{\text{fb}} = 80 - \left(\frac{Q}{A_c h_{\text{condensation}}} \right) = 80 - \left(\frac{73.7}{0.048 * 0.33 * 3992} \right) \approx 79^\circ\text{C}$$

Superheat region:

$$c_{pG}@T_{\bar{m}} = 1.1322 \left(\frac{\text{kJ}}{\text{kg} \cdot \text{K}} \right)$$

$$\rho_G@T_{\bar{m}} = 83.85 \left(\frac{\text{kg}}{\text{m}^3} \right)$$

$$k_G@T_{\bar{m}} = 0.02 \left(\frac{\text{W}}{\text{m} \cdot \text{K}} \right)$$

$$\mu_G@T_{\bar{m}} = 1.36 * 10^{-5} \left(\frac{\text{N} \cdot \text{s}}{\text{m}^2} \right)$$

$$\text{Pr}_G = \left(\frac{c_{pG} \cdot \mu_G}{k_G} \right) = \left(\frac{1132.2 * 1.36 * 10^{-5}}{0.02} \right) = 0.77$$

$$v_G = \frac{\dot{m}_R \cdot v_G}{A_f} = \left(\frac{0.7 * 10^{-3}}{83.85 * 7.3 * 10^{-6}} \right) = 1.14 \text{ (m/s)}$$

$$\text{Re}_G = \left(\frac{\rho_G \cdot v_G \cdot d}{\mu_G} \right) = \left(\frac{83.85 * 1.14 * 0.024 * 0.0254}{1.36 * 10^{-5}} \right) = 4298$$

Absolute roughness for aluminum (ϵ_R) = $1.5 * 10^{-6}$ m

Relative roughness for aluminum (ϵ_R/d) = 0.0025 m

$f = 0.042$

$$\text{Nu} = \left[\frac{\left(\frac{f}{8} \right) (\text{Re}_G - 1000) \text{Pr}_G}{1 + \left(12.7 \left(\frac{f}{8} \right)^{0.5} \left(\text{Pr}_G^{\frac{2}{3}} - 1 \right) \right)} \right]$$

Since (L/d) is greater than 60 therefore:

$$\text{Nu} = \bar{\text{Nu}} = \left(\frac{\bar{h}_G \cdot d}{k_G} \right) = \left[\frac{\frac{0.042}{8} * (4298 - 1000) * 0.77}{1 + \left(12.7 * \left(\frac{0.042}{8} \right)^{0.5} \left(0.77^{\frac{2}{3}} - 1 \right) \right)} \right] = 15.6$$

$$\therefore \bar{h}_G = 513 \left(\frac{\text{W}}{\text{m}^2 \cdot \text{K}} \right)$$

where \bar{h}_g is the heat transfer coefficient of the refrigerant superheated gas

$$A_0 U_0 = \left[\frac{1}{A_0 \text{HTC}} + \frac{1}{A_c \bar{h}_G} \right]^{-1}$$

$$\therefore A_0 U_0 = \left[\frac{1}{0.0254 L_2 * 1120} + \frac{1}{0.048 L_2 * 513} \right]^{-1}$$

where L_2 is the superheat length.

$$\therefore A_0 U_0 = [13.2 L_2] \text{ W/K}$$

$$Q = A_0 \cdot U_0 \cdot (T_{G(\text{av.})} - T_{bi})$$

$$\therefore 105 - 73.7 = 31.3 = [12.3 L_2] * 29$$

$$\therefore L_2 = L_{(\text{one heated surface})} = 0.088 \text{ m}$$

The total length of single surface condenser is $L_1 + L_2 = 0.33 + 0.088 = 0.42 \text{ m}$

$$L_{(\text{double surfaces})} = L_{\text{condenser}} = \frac{L_{(\text{one heated surface})}}{2(N-1)} = \frac{L_{(\text{one heated surface})}}{6} = 0.07 \text{ m} = 2.8''$$

Outlet air temperature (T_{bo}):

$$m_a = A_{\text{flow}} \cdot \rho \cdot v = \left((2.4 - ((N * t_{\text{tube}}) + (2(N-1)t_{\text{foam}}))) \cdot L_{\text{double surface}} \right) \cdot \rho \cdot v$$

$$Q = 105 = m_a \cdot c_p \cdot (T_{bo} - T_{bi})$$

$$105 = \left(\left((2.4 - ((4 * 0.079) + (2 * 3 * 0.079))) * 2.8 \right) * 0.0254^2 \right) * 1 * 4 * 1005 * (T_{bo} - 71)$$

$$T_{bo} = 80^\circ\text{C}$$

$$\therefore W^* = L_{\text{double surface}} = L_{\text{condenser}} = 2.8''$$

Case (3): Condensation and Subcooling

Allowing the refrigerant liquid to exit the condenser at 76°C , $\Delta h_{\text{subcooling}} = 3.8 \left(\frac{\text{kJ}}{\text{kg}} \right)$.

$$Q = 105 = m_R \cdot (h_{fg} + \Delta h_{\text{subcooling}})$$

$$\therefore 105 = m_R \cdot [(410.7 - 305.4) + 3.8] \cdot 10^3 \rightarrow m_R = 0.96 \left(\frac{\text{g}}{\text{s}} \right)$$

Condensation region:

$$\begin{aligned}Q_{\text{condensation}} &= m_a \cdot c_p \cdot (T_{\text{bo}} - T_{\text{bi}}) = m_R \cdot h_{\text{fg}} \\&= 0.96 * 10^{-3} \cdot (410.7 - 305.4) * 10^3 = 101.3 \text{ W} \\&= A_O \cdot U_O \cdot (T_{\text{sat}} - T_{\text{bi}}) \\&= A_c \cdot h_{\text{condensation}} \cdot (T_{\text{sat}} - T_{\text{fb}}) \\&= A_O \cdot \text{HTC} \cdot (T_{\text{fb}} - T_{\text{bi}})\end{aligned}$$

The specific volume of the gas is $(v_g) = \frac{1}{89.33} = 0.0112 \text{ (m}^3/\text{kg)} \rightarrow \text{(NIST)}$

The dynamic viscosity of the gas is $(\mu_g) = 1.3282 * 10^{-5} \text{ (Pa} \cdot \text{s)} \rightarrow \text{(NIST)}$

Therefore during the condensation, the gas side velocity $(v_g) = \frac{m_R \cdot v_g}{A_f} = 1.47 \text{ (m/s)}$

$$\text{Re}_g = \left(\frac{v_g \cdot d}{v_g \cdot \mu_g} \right) = 6036 < 35,000$$

$$h_{\text{condensation}} = 0.555 \left[\frac{g \cdot \rho_l \cdot (\rho_l - \rho_g) \cdot k_l^3 \cdot h'_{\text{fg}}}{\mu_l \cdot (T_{\text{sat}} - T_{\text{fb}}) \cdot d} \right]^{0.25}$$

$$c_{p_l} @ 80^\circ\text{C} = 1.5 \left(\frac{\text{kJ}}{\text{kg} \cdot \text{K}} \right) \rightarrow \text{(NIST)}$$

$$\rho_l @ 80^\circ\text{C} = 1138 \left(\frac{\text{kg}}{\text{m}^3} \right) \rightarrow \text{(NIST)}$$

$$k_l @ 80^\circ\text{C} = 0.0573 \left(\frac{\text{W}}{\text{m} \cdot \text{K}} \right) \rightarrow \text{(NIST)}$$

$$\mu_l @ 80^\circ\text{C} = 0.000143 \left(\frac{\text{N} \cdot \text{s}}{\text{m}^2} \right) \rightarrow \text{(NIST)}$$

assume that the condenser surface temperature $\approx 79^\circ\text{C}$ and we will justify this assumption after calculating the minichannel length.

$$h'_{\text{fg}} = h_{\text{fg}} + \frac{3}{8} \cdot c_{p_l} \cdot (T_{\text{sat}} - T_{\text{fb}}) = 105.9 \frac{\text{kJ}}{\text{kg}}$$

$$\therefore h_{\text{condensation}} = 3992 \left(\frac{\text{W}}{\text{m}^2 \cdot \text{K}} \right)$$

The actual air velocity can be determined from the foam-fan curve using trial and error:

$$v_{\text{actual}} = 4 \left(\frac{\text{m}}{\text{s}} \right) \text{ @ pressure drop of } 560(\text{Pa})$$

The corresponding air-side HTC for the new area will be:

$$\text{HTC} = 1120 \left(\frac{\text{W}}{\text{m}^2 \cdot \text{K}} \right)$$

$$\therefore A_o U_o = \left[\frac{1}{0.0254 L_1 * 1120} + \frac{1}{0.048 L_1 * 3992} \right]^{-1}$$

$$= \left[\frac{1}{28.4 L_1} + \frac{1}{191.6 L_1} \right]^{-1}$$

$$\therefore A_o U_o = 24.8 * L_1 \left(\frac{\text{W}}{\text{K}} \right)$$

$$Q = A_o \cdot U_o \cdot (T_{\text{sat}} - T_{\text{bi}})$$

$$\therefore 101.3 = 24.8 * L_1 * 9$$

$$\therefore L_1 = L_{(\text{one heated surface})} = 0.45 \text{ m}$$

Check for the surface temperature of the condenser:

$$T_{\text{fb}} = 80 - \left(\frac{Q}{A_c h_{\text{condensation}}} \right) = 80 - \left(\frac{101.3}{0.048 * 0.45 * 3992} \right) \approx 79^\circ\text{C}$$

Subcooling region:

$$c_{pL} @ T_{\bar{m}} = 1.46 \left(\frac{\text{kJ}}{\text{kg} \cdot \text{K}} \right)$$

$$\rho_L @ T_{\bar{m}} = 1160 \left(\frac{\text{kg}}{\text{m}^3} \right)$$

$$k_L @ T_{\bar{m}} = 0.0584 \left(\frac{\text{W}}{\text{m} \cdot \text{K}} \right)$$

$$\mu_L @ T_{\bar{m}} = 1.5 * 10^{-4} \left(\frac{\text{N} \cdot \text{s}}{\text{m}^2} \right)$$

$$\text{Pr}_L = \left(\frac{c_{pL} \cdot \mu_L}{k_L} \right) = \left(\frac{1460 * 1.5 * 10^{-4}}{0.0584} \right) = 3.75$$

$$v_L = \frac{m_{\dot{R}} \cdot u_L}{A_f} = \left(\frac{0.96 * 10^{-3}}{1160 * 7.3 * 10^{-6}} \right) = 0.11 \text{ (m/s)}$$

$$Re_L = \left(\frac{\rho_L \cdot v_L \cdot d}{\mu_L} \right) = \left(\frac{1160 * 0.11 * 0.024 * 0.0254}{1.5 * 10^{-4}} \right) = 534$$

$$\therefore \overline{Nu} = \left(\frac{\bar{h}_L \cdot d}{k_L} \right) = 4.36$$

$$\therefore \bar{h}_L = 417.7 \left(\frac{W}{m^2 \cdot K} \right)$$

$$\therefore A_O U_O = \left[\frac{1}{0.0254 L_3 * 1120} + \frac{1}{0.048 L_3 * 417.7} \right]^{-1}$$

where L_3 is the subcooling length.

$$\therefore A_O U_O = [11.7 L_3] \text{ W/K}$$

$$Q = A_O \cdot U_O \cdot (T_{L(av.)} - T_{bi})$$

$$\therefore 105 - 101.3 = 3.7 = [11.7 L_3] * 7$$

$$\therefore L_3 = L_{(one\ heated\ surface)} = 0.05 \text{ m}$$

The total length of single surface condenser is $L_1 + L_3 = 0.45 + 0.05 = 0.5 \text{ m}$

$$L_{(double\ surfaces)} = L_{condenser} = \frac{L_{(one\ heated\ surface)}}{2(N-1)} = \frac{L_{(one\ heated\ surface)}}{6} = 0.082 \text{ m} = 3.2''$$

Outlet air temperature (T_{bo}):

$$m_a = A_{flow} \cdot \rho \cdot v = \left((2.4 - ((N * t_{tube}) + (2(N-1)t_{foam}))) \cdot L_{double\ surface} \right) \cdot \rho \cdot v$$

$$Q = 105 = m_a \cdot c_p \cdot (T_{bo} - T_{bi})$$

$$105 = \left(\left((2.4 - ((4 * 0.079) + (2 * 3 * 0.079))) * 3.2 \right) * 0.0254^2 \right) * 1 * 4 * 1005 * (T_{bo} - 71)$$

$$T_{bo} = 78.9^\circ\text{C}$$

$$\therefore W^* = L_{double\ surface} = L_{condenser} = 3.2''$$

Case (4): Condensation

$$Q = 105 = m_R \cdot h_{fg}$$

$$\therefore 105 = m_R \cdot [410.7 - 305.4] \cdot 10^3 \rightarrow m_R = 1 \left(\frac{g}{s} \right)$$

Condensation region:

$$\begin{aligned}Q_{\text{condensation}} &= m_a \cdot c_p \cdot (T_{\text{bo}} - T_{\text{bi}}) = m_R \cdot h_{\text{fg}} \\&= 1 * 10^{-3} \cdot (410.7 - 305.4) * 10^3 = 105.3 \text{ W} \\&= A_O \cdot U_O \cdot (T_{\text{sat}} - T_{\text{bi}}) \\&= A_c \cdot h_{\text{condensation}} \cdot (T_{\text{sat}} - T_{\text{fb}}) \\&= A_O \cdot \text{HTC} \cdot (T_{\text{fb}} - T_{\text{bi}})\end{aligned}$$

The specific volume of the gas is $(v_g) = \frac{1}{89.33} = 0.0112 \text{ (m}^3/\text{kg)} \rightarrow \text{(NIST)}$

The dynamic viscosity of the gas is $(\mu_g) = 1.3282 * 10^{-5} \text{ (Pa} \cdot \text{s)} \rightarrow \text{(NIST)}$

Therefore during the condensation, the gas side velocity $(v_g) = \frac{m_R \cdot v_g}{A_f} = 1.53 \text{ (m/s)}$

$$\text{Re}_g = \left(\frac{v_g \cdot d}{v_g \cdot \mu_g} \right) = 6272 < 35,000$$

$$h_{\text{condensation}} = 0.555 \left[\frac{g \cdot \rho_l \cdot (\rho_l - \rho_g) \cdot k_l^3 \cdot h'_{\text{fg}}}{\mu_l \cdot (T_{\text{sat}} - T_{\text{fb}}) \cdot d} \right]^{0.25}$$

$$c_{p_l} @ 80^\circ\text{C} = 1.5 \left(\frac{\text{kJ}}{\text{kg} \cdot \text{K}} \right) \rightarrow \text{(NIST)}$$

$$\rho_l @ 80^\circ\text{C} = 1138 \left(\frac{\text{kg}}{\text{m}^3} \right) \rightarrow \text{(NIST)}$$

$$k_l @ 80^\circ\text{C} = 0.0573 \left(\frac{\text{W}}{\text{m} \cdot \text{K}} \right) \rightarrow \text{(NIST)}$$

$$\mu_l @ 80^\circ\text{C} = 0.000143 \left(\frac{\text{N} \cdot \text{s}}{\text{m}^2} \right) \rightarrow \text{(NIST)}$$

assume that the condenser surface temperature $\approx 79^\circ\text{C}$ and we will justify this assumption after calculating the minichannel length.

$$h'_{\text{fg}} = h_{\text{fg}} + \frac{3}{8} \cdot c_{p_l} \cdot (T_{\text{sat}} - T_{\text{fb}}) = 105.9 \frac{\text{kJ}}{\text{kg}}$$

$$\therefore h_{\text{condensation}} = 3992 \left(\frac{\text{W}}{\text{m}^2 \cdot \text{K}} \right)$$

The actual air velocity can be determined from the foam-fan curve using trial and error:

$$v_{\text{actual}} = 4 \left(\frac{\text{m}}{\text{s}} \right) \text{ @ pressure drop of } 560(\text{Pa})$$

The corresponding air-side HTC for the new area will be:

$$\text{HTC} = 1120 \left(\frac{\text{W}}{\text{m}^2 \cdot \text{K}} \right)$$

$$\therefore A_o U_o = \left[\frac{1}{0.0254 L_1 * 1120} + \frac{1}{0.048 L_1 * 3992} \right]^{-1}$$

$$= \left[\frac{1}{28.4 L_1} + \frac{1}{191.6 L_1} \right]^{-1}$$

$$\therefore A_o U_o = 24.8 * L_1 \left(\frac{\text{W}}{\text{K}} \right)$$

$$Q = A_o \cdot U_o \cdot (T_{\text{sat}} - T_{\text{bi}})$$

$$\therefore 105.3 = 24.8 * L_1 * 9$$

$$\therefore L_1 = L_{(\text{one heated surface})} = 0.47 \text{ m}$$

Check for the surface temperature of the condenser:

$$T_{\text{fb}} = 80 - \left(\frac{Q}{A_c h_{\text{condensation}}} \right) = 80 - \left(\frac{105.3}{0.048 * 0.47 * 3992} \right) \approx 79^\circ\text{C}$$

The total length of single surface condenser is $L_1 = 0.47 \text{ m}$

$$L_{(\text{double surfaces})} = L_{\text{condenser}} = \frac{L_{(\text{one heated surface})}}{2(N-1)} = \frac{L_{(\text{one heated surface})}}{6} = 0.078 \text{ m} = 3.1''$$

Outlet air temperature (T_{bo}):

$$m_a = A_{\text{flow}} \cdot \rho \cdot v = \left(\left(2.4 - ((N * t_{\text{tube}}) + (2(N-1)t_{\text{foam}})) \right) \cdot L_{\text{double surface}} \right) \cdot \rho \cdot v$$

$$Q = 105 = m_a \cdot c_p \cdot (T_{\text{bo}} - T_{\text{bi}})$$

$$105 = \left(\left(\left(2.4 - ((4 * 0.079) + (2 * 3 * 0.079)) \right) * 3.1 \right) * 0.0254^2 \right) * 1 * 4 * 1005 * (T_{\text{bo}} - 71)$$

$$T_{bo} = 79.1^{\circ}\text{C}$$

$$\therefore W^* = L_{\text{double surface}} = L_{\text{condenser}} = 3.1''$$

LIST OF REFERENCES

- [1] N. C. Gallego and J. W. Klett, "Carbon foams for thermal management," *Carbon*, vol. 41, pp. 1461-1466, 2003.
- [2] J. Klett, R. Hardy, E. Romine, C. Walls, and T. Burchell, "High-thermal-conductivity, mesophase-pitch-derived carbon foams: effect of precursor on structure and properties," *Carbon*, vol. 38, pp. 953-973, 2000.
- [3] A. G. Straatman, N. C. Gallego, Q. Yu, L. Betchen, and B. E. Thompson, "Forced convection heat transfer and hydraulic losses in graphitic foam," *Journal of Heat Transfer*, vol. 129, pp. 1237-1245, 2007.
- [4] S. Mancin, C. Zilio, A. Diani, and L. Rossetto, "Experimental air heat transfer and pressure drop through copper foams," *Experimental Thermal and Fluid Science*, vol. 36, pp. 224-232, 2012.
- [5] R. Y. Chein, H. H. Yang, T. H. Tsai, and C. J. Lu, "Experimental study of heat sink performance using copper foams fabricated by electroforming," *Microsystem Technologies-Micro-and Nanosystems-Information Storage and Processing Systems*, vol. 16, pp. 1157-1164, 2010.
- [6] S. Y. Kim, J. W. Paek, and B. H. Kang, "Thermal performance of aluminum-foam heat sinks by forced air cooling," *IEEE Transactions on Components and Packaging Technologies*, vol. 26, pp. 262-267, 2003.
- [7] S. Y. Kim, J. W. Paek, and B. H. Kang, "Flow and heat transfer correlations for porous fin in a plate-fin heat exchanger," *Journal of Heat Transfer*, vol. 122, pp. 572-578, 2000.
- [8] A. A. Sertkaya, K. Altinisik, and K. Dincer, "Experimental investigation of thermal performance of aluminum finned heat exchangers and open-cell aluminum foam heat exchangers," *Experimental Thermal and Fluid Science*, vol. 36, pp. 86-92, 2012.
- [9] P. T. Garrity, J. F. Klausner, and R. W. Mei, "Performance of aluminum and carbon foams for air side heat transfer augmentation," *Journal of Heat Transfer*, vol. 132, p. 121901 (9 pp.), 2010.
- [10] K. C. Leong, H. Y. Li, L. W. Jin, and J. C. Chai, "Numerical and experimental study of forced convection in graphite foams of different configurations," *Applied Thermal Engineering*, vol. 30, pp. 520-532, 2010.

- [11] Z. A. Williams and J. A. Roux, "Graphite foam thermal management of a high packing density array of power amplifiers," *Journal of Electronic Packaging*, vol. 128, pp. 456-465, 2006.
- [12] W. Wu, J. H. Du, Y. R. Lin, L. C. Chow, H. Bostanci, B. A. Saarloos, and D. P. Rini, "Evaluation of compact and effective air-cooled carbon foam heat sink," *Journal of Heat Transfer*, vol. 133, p. 054504 (5 pp.), 2011.
- [13] Y. R. Lin, J. H. Du, W. Wu, L. C. Chow, and W. Notardonato, "Experimental study on heat transfer and pressure drop of recuperative heat exchangers using carbon foam," *Journal of Heat Transfer*, vol. 132, p. 091902 (10 pp.), 2010.
- [14] S. P. Vanka and K. M. Stone, "Review of literature on heat transfer enhancement in compact heat exchangers," ed: Air Conditioning and Refrigeration Center, College of Engineering, University of Illinois at Urbana-Champaign, 1996.
- [15] J. G. Soland, J. W. M. Mack, and W. M. Rohsenow, "Performance ranking of plate-fin heat exchanger surfaces," *Journal of Heat Transfer*, vol. 100, pp. 514-519, 1978.
- [16] K. Vafai and S. Kim, "On the limitations of the Brinkman-Forchheimer-extended Darcy equation," *International Journal of Heat and Fluid flow*, vol. 16, pp. 11-15, 1995.
- [17] M. Sözen and K. Vafai, "Analysis of the non-thermal equilibrium condensing flow of a gas through a packed bed," *International Journal of Heat and Mass Transfer*, vol. 33, pp. 1247-1261, 1990.
- [18] K. Vafai, *Handbook of Porous Media*: CRC Press, 2009.
- [19] M. Kaviany, *Principles of Heat Transfer in Porous Media*: New York, Springer-Verlag, 1995.
- [20] A. A. Mohamad and G. Karim, "Flow and heat transfer within segregated beds of solid particles," *Journal of Porous Media*, vol. 4, pp. 215–224, 2001.
- [21] B. Alazmi and K. Vafai, "Analysis of fluid flow and heat transfer interfacial conditions between a porous medium and a fluid layer," *International Journal of Heat and Mass Transfer*, vol. 44, pp. 1735-1749, 2001.

- [22] A. Mohamad, "Heat transfer enhancements in heat exchangers fitted with porous media Part I: constant wall temperature," *International journal of thermal sciences*, vol. 42, pp. 385-395, 2003.
- [23] B. I. Pavel and A. A. Mohamad, "An experimental and numerical study on heat transfer enhancement for gas heat exchangers fitted with porous media," *International Journal of Heat and Mass Transfer*, vol. 47, pp. 4939-4952, 2004.
- [24] B. Alazmi and K. Vafai, "Analysis of variants within the porous media transport models," *Journal of Heat Transfer*, vol. 122, pp. 303-26, 2000.
- [25] B. Alazmi and K. Vafai, "Analysis of variable porosity, thermal dispersion, and local thermal nonequilibrium on free surface flows through porous media," *Journal of Heat Transfer*, vol. 126, pp. 389-99, 2004.
- [26] L. J. Betchen and A. G. Straatman, "An investigation of the effects of a linear porosity distribution on non-equilibrium heat transfer in high-conductivity graphitic foam," *Numerical Heat Transfer, Part A: Applications*, vol. 58, pp. 605-624, 2010.
- [27] A. Marafie and K. Vafai, "Analysis of non-Darcian effects on temperature differentials in porous media," *International Journal of Heat and Mass Transfer*, vol. 44, pp. 4401-4411, 2001.
- [28] A. Haji-Sheikh and K. Vafai, "Analysis of flow and heat transfer in porous media imbedded inside various-shaped ducts," *International Journal of Heat and Mass Transfer*, vol. 47, pp. 1889-1905, 2004.
- [29] C. T. DeGroot and A. G. Straatman, "A finite-volume model for fluid flow and nonequilibrium heat transfer in conjugate fluid-porous domains using general unstructured grids," *Numerical Heat Transfer, Part B: Fundamentals*, vol. 60, pp. 252-277, 2011.
- [30] R. S. Figliola and D. E. Beasley, *Theory and Design for Mechanical Measurements*, 4th ed. Hoboken, N.J: John Wiley, 2006.
- [31] A. G. Straatman, N. C. Gallego, Q. Yu, L. Betchen, and B. Thompson, "Forced convection heat transfer and hydraulic losses in graphitic foam," *Journal of heat transfer*, vol. 129, pp. 1237-1245, 2007.

- [32] J. H. Du, L. C. Chow, Y. R. Lin, W. Wu, J. Kapat, and W. U. Notardonato, Thermally Conductive Porous Element-Based Recuperators, US Patent 8,322,406, 2012.
- [33] D. P. Dewitt and F. P. Incropera, Fundamentals of Heat and Mass Transfer: Wiley, 2002.
- [34] G. A. Slack, "Anisotropic thermal conductivity of pyrolytic graphite," *Physical Review*, vol. 127, p. 694, 1962.
- [35] P. Klemens, "The specific heat and thermal conductivity of graphite," *Australian Journal of Physics*, vol. 6, pp. 405-409, 1953.
- [36] B. T. Kelly, "Physics of graphite," 1981.
- [37] C. Uher and D. Morelli, "Thermal transport properties of SbCl₅-graphite and of HOPG in the c-direction," *Synthetic Metals*, vol. 12, pp. 91-96, 1985.
- [38] D. Morelli and C. Uher, "Thermal conductivity and thermopower of graphite at very low temperatures," *Physical Review B*, vol. 31, p. 6721, 1985.
- [39] J. G. Park, C. Zhang, R. Liang, and B. Wang, "Nano-machining of highly oriented pyrolytic graphite using conductive atomic force microscope tips and carbon nanotubes," *Nanotechnology*, vol. 18, p. 405306, 2007.
- [40] J. Song, Z. Liu, C. Li, H. Chen, and H. He, "SPM-based nanofabrication using a synchronization technique," *Applied Physics A: Materials Science & Processing*, vol. 66, pp. S715-S717, 1998.
- [41] R. Windholz and P. Molian, "Nanosecond pulsed excimer laser machining of chemical vapour deposited diamond and highly oriented pyrolytic graphite: Part I An experimental investigation," *Journal of materials science*, vol. 32, pp. 4295-4301, 1997.